

# THESIS

## THE VORTICITY STRUCTURE OF THE 2–3 JUNE 2003 MCS DURING BAMEX

Submitted by

Michelle A. Harrold

Department of Atmospheric Science

In partial fulfillment of the requirements

For the Degree of Master of Science

Colorado State University

Fort Collins, Colorado

Fall 2009

## ABSTRACT OF THESIS

### THE VORTICITY STRUCTURE OF THE 2-3 JUNE 2003 MCS DURING BAMEX

This study examined the low- and mid-level vorticity structure of a mesoscale convective system (MCS) that developed on 2-3 June 2003 in northern Mississippi. The MCS occurring during the Bow Echo and Mesoscale Convective Vortex Experiment (BAMEX); therefore, it was highly sampled by both ground-based (e.g. mobile sounding systems, weather radar, and wind profilers) and airborne platforms, allowing for a fully comprehensive analysis of the weather system. Airborne platforms used in this study include the Electra Doppler Radar (ELDORA), which was mounted on the Naval Research Laboratory (NRL) P-3 aircraft, and a Doppler radar mounted on the National Oceanic and Atmospheric Administration (NOAA) P-3 aircraft.

In the afternoon of 2 June 2003, a squall line began to organize near the Arkansas/Mississippi border. Mobile soundings and the wind profiler from Okolona, MS indicated the convective system formed in weak-to-moderate shear ( $\sim 15 \text{ m s}^{-1}$  from the surface to 5.0 km) while exhibiting a large component of along-line shear. ELDORA and the NOAA P-3 captured the convective line as it transitioned from a linear structure with small-scale embedded bowed segments (10 – 15 km in length) to a larger-scale bowed convective system ( $\sim 50$  km in length).

Data from ELDORA and the NOAA P-3 allowed for high-resolution, dual- and quadruple-Doppler wind syntheses, which provided a detailed kinematic analysis of the

2-3 June 2003 MCS. Analysis of the vertical vorticity field revealed a banded pattern of cyclonic and anticyclonic vertical vorticity that was oriented parallel to the convective line. Cyclonic vertical vorticity was concentrated ahead of the convective line, with anticyclonic vertical vorticity associated with and behind the convective line. Small-scale cyclonic and anticyclonic vortices (~10 km) in the low- and mid-levels were observed within the bands of vertical vorticity; these vortices were often associated with the small-scale bowed segments. In addition to the small-scale vortices, a mid-level, counter-rotating vortex couplet also formed and was associated with the larger-scale bowing of the convective line.

Analysis of the vertical vorticity time tendency equation showed tilting of the environmental horizontal vorticity within the updraft region generated the banded pattern. Upward tilting ahead of the updraft resulted in cyclonic vertical vorticity, and the downward tilting on the backside of the updraft results in anticyclonic vertical vorticity with the small-scale vortices forming in regions with locally intense updrafts. Stretching then amplified the preexisting vertical vorticity. The mid-level, counter-rotating vortices also formed due to tilting effects; however, the vortices quickly became dominated by the stretching term and retreated toward the stratiform region, being maintained by system-generated processes. This overall vorticity pattern is directly connected to the along-line shear associated with the environment that the MCS formed.

Michelle A. Harrold  
Department of Atmospheric Science  
Colorado State University  
Fort Collins, CO 80523  
Fall 2009

## ACKNOWLEDGEMENTS

This research was funded by the National Center for Atmospheric Research (NCAR) under NSF00001 (subcontract # S06-58489). NCAR is operated by the University Corporation for Atmospheric Research under the sponsorship of the National Science Foundation. The data from this project was obtained during the Bow Echo and Mesoscale Convective Vortex Experiment (BAMEX) and is archived by the Earth Observing Laboratory (EOL) at NCAR. Archived data from this study is located at [http://data.eol.ucar.edu/master\\_list/?project=BAMEX](http://data.eol.ucar.edu/master_list/?project=BAMEX).

Drs. Richard Johnson and Roger Wakimoto, my co-advisors, have offered invaluable insight and knowledge, not only about convective weather systems but about the entire research process. I would especially like to thank them for the flexibility they have shown within the last year due to unforeseen circumstances. In addition, I would like to thank my outside committee members, Drs. Steven Rutledge and V. Chandrasekar for the constructive comments that they offered in conjunction with this thesis.

Special thanks go to Michael Bell (EOL at NCAR) for spending countless hours assisting me with airborne radar analysis, both the processing and visualizing aspects. His availability, knowledge, and patience were vital and greatly appreciated. Also, thanks go to Dr. Wen-Chau Lee (EOL at NCAR) for spending time discussing topics related to airborne radar analysis. I am also thankful for the assistance from several members within Dr. Johnson's and Dr. Rutledge's research groups. Their help and availability with computers, programming problems, and general discussion about radar and weather systems was invaluable. Finally, I would like to thank my family, especially my parents, and friends; they have shown unconditional love and support.

# CONTENTS

<b>1</b>	<b>Introduction</b>	<b>1</b>
<b>2</b>	<b>Background</b>	<b>4</b>
2.1	Overview of MCSs	4
2.1.1	General definition and structure	4
2.1.2	Classification of MCSs	7
2.1.3	Bowing convection	10
2.2	Dynamics of MCSs	16
2.2.1	Cold pool and shear interactions	16
2.2.2	Generation and maintenance of rear-inflow	19
2.2.3	Generation and maintenance of mesoscale vortices	20
2.3	Summary	30
<b>3</b>	<b>Methodology and Data Analysis</b>	<b>33</b>
3.1	Data sources from BAMEX	33
3.1.1	Ground-based observation network	35
3.1.2	Airborne platforms	35
3.2	Methods of data analysis	43
3.2.1	Principles of multiple-Doppler analysis	43
3.2.2	Data editing	48
3.2.3	Converting to Cartesian grid	50
3.2.4	Synthesizing data	53
<b>4</b>	<b>Environmental Conditions</b>	<b>55</b>
4.1	Synoptic and mesoscale conditions	55
4.2	Summary	67
<b>5</b>	<b>Overall Structure of the MCS</b>	<b>70</b>
5.1	Overall squall line evolution	70
5.2	Banded vorticity pattern	83
5.3	Discussion	90
<b>6</b>	<b>Vortices within the MCS</b>	<b>95</b>
6.1	Small-scale vortices	95

6.1.1	Overview of small-scale vortices	95
6.1.2	Vortexgenesis	102
6.2	Mid-level counter-rotating vortices	113
6.3	Discussion	121
<b>7</b>	<b>Conclusions</b>	<b>127</b>
7.1	Summary of results	127
7.2	Suggested future work	131

## LIST OF FIGURES

2.1	Conceptual model of an MCS with trailing stratiform precipitation. From Houze et al. (1989).	5
2.2	Schematic of the surface pressure field and precipitation patterns for symmetric and asymmetric MCSs. From Loehrer and Johnson (1995).	7
2.3	Schematics for the three modes of linear MCS: TS, LS, and PS. From Parker and Johnson 2000).	8
2.4	Vertical profiler of layer-mean, storm-relative winds for the three modes of MCS. From (Parker and Johnson 2000).	9
2.5	Conceptual model of the bow echo. From Fujita (1978).	12
2.6	Generalized pathways for bowed convection evolution. From Klimowski et al. (2004).	14
2.7	Four phases within the evolution of an idealized MCS showing the interaction between the low-level wind shear, the cold pool, and the rear-inflow jet. From Weisman (1993).	17
2.8	Schematic showing tilting of the horizontal vorticity in an environment with ambient westerly shear. From Weisman (1993).	22
2.9	Schematic showing tilting of the horizontal vorticity into the vertical via vortex stretching. From Weisman and Davis (1998).	24
2.10	Schematic proposed by Trapp and Weisman (2003) showing the proposed mechanism for low-level mesovortexgenesis.	28
2.11	Schematic proposed by Wakimoto et al. (2006b) to show the origin of the vortex couplet along the outflow boundary.	32
	32	
3.1	Map displaying area encompassed by BAMEX.	34
3.2	Geometry of the airborne dual-Doppler radar system. From Chong and Campos (1996).	37
3.3	Reflectivity from ELDORA and the NOAA P-3 superimposed on Level III NEXRAD data from KGWX.	41
3.4	Flowchart of the data analysis process.	44
3.5	Horizontal projection of flight patterns and beam angles for “L”-shaped flight patterns and FAST. From Jorgensen et al. (1996).	46
4.1	Surface map from 2-3 June 2003 for 1200, 1800, 2200, and 0000 UTC.	57

4.2	Upper-air maps for 2-3 June 2003 at 1200 UTC for 850, 500, and 300 hPa.	58
4.3	NOWRAD composite over BAMEX region for 2 June 2003 at 1400 and 1800 UTC.	62
4.4	Sequence of composite radar images for the 2-3 June 2003 squall line.	63
4.5	Mobile sounding from 2 June 2003 at 1735 UTC.	64
4.6	Mobile sounding from 2 June 2003 at 1903 UTC.	65
4.7	Profiler data from Okolona, MS from 1700 – 0000 UTC on 2-3 June 2003.	66
4.8	Hodographs from the Okolona, MS wind profiler from 2100 – 0000 UTC on 2-3 June 2003.	68
5.1	Isochrone analysis of the six ELDORA flight legs.	71
5.2	NOWRAD composite of BAMEX region at 2230, 2300, 2330, and 0000 UTC on 2-3 June 2003.	72
5.3	Storm-relative winds superimposed on ELDORA reflectivity for all six flight legs.	75
5.4	Approximate east-west cross-sections using ELDORA analysis through a small-scale bow during the first flight leg displaying reflectivity, vertical vorticity, and vertical velocity.	77
5.5	Approximate east-west cross-sections using quad-Doppler analysis through a small-scale bow during the second flight leg displaying reflectivity, vertical vorticity, and vertical velocity.	79
5.6	Approximate east-west cross-sections using quad-Doppler analysis through a small-scale bow during the fifth flight leg displaying reflectivity, vertical vorticity, vertical velocity, and horizontal vorticity.	80
5.7	East-west cross-sections through centerline of a vortex couplet for differing shear simulations. From Weisman and Davis (1998).	82
5.8	Reflectivity and vertical velocity superimposed on vertical vorticity at 0.45 km for the six flight legs.	85
5.9	ELDORA-derived tilting and stretching terms for the first flight leg at 1.05 km.	89
5.10	Quad-Doppler-derived tilting and stretching terms for the second flight leg at 1.05 km.	90
5.11	Quad-Doppler-derived tilting and stretching terms for the fifth flight leg at 1.05 km.	91
6.1	ELDORA Reflectivity, vertical velocity, and storm-relative winds superimposed on vertical vorticity at 2.25 km for the first flight leg.	96
6.2	ELDORA Reflectivity, vertical velocity, and storm-relative winds superimposed on vertical vorticity at 2.25 km for the second flight leg.	97
6.3	ELDORA Reflectivity, vertical velocity, and storm-relative winds superimposed on vertical vorticity at 2.25 km for the third flight leg.	99
6.4	ELDORA Reflectivity, vertical velocity, and storm-relative winds superimposed on vertical vorticity at 2.25 km for the fourth flight leg.	100
6.5	ELDORA Reflectivity, vertical velocity, and storm-relative winds superimposed on vertical vorticity at 2.25 km for the fifth flight leg.	101
6.6	ELDORA Reflectivity, vertical velocity, and storm-relative winds	

	superimposed on vertical vorticity at 2.25 km for the sixth flight leg.	102
6.7	Approximate east-west cross-sections using ELDORA analysis through a small-scale pair of anticyclonic and cyclonic vortices during the first flight leg displaying reflectivity, vertical vorticity, and vertical velocity.	103
6.8	ELDORA-derived reflectivity and vertical velocity superimposed on vertical vorticity and the tilting, stretching, and combined tilting and stretching terms at 1.05 km during the first flight leg.	105
6.9	ELDORA-derived reflectivity and vertical velocity superimposed on vertical vorticity and the tilting, stretching, and combined tilting and stretching terms at 1.05 km during the first flight leg.	106
6.10	Approximate east-west cross-sections using ELDORA analysis through a forming small-scale pair of anticyclonic and cyclonic vortices during the third flight leg displaying reflectivity, vertical vorticity, vertical velocity, and the tilting term.	108
6.11	Approximate east-west cross-sections using ELDORA analysis through a developed small-scale pair of anticyclonic and cyclonic vortices during the sixth flight leg displaying reflectivity, vertical vorticity, vertical velocity, and the tilting term.	110
6.12	Approximate east-west cross-sections using ELDORA analysis through an area with no vortex formation during the first flight leg displaying reflectivity, vertical vorticity, and vertical velocity.	111
6.13	Approximate north-south cross-sections using quad-Doppler analysis through the anticyclonic band during the second flight leg displaying vertical vorticity, the stretching term, and the tilting term.	114
6.14	Horizontal plots at 2.25 km of the evolution of the vortex couplet from the third to sixth leg.	115
6.15	Approximate north-south cross-sections using ELDORA analysis through the vortex couplet during the third flight leg, displaying vertical vorticity, the stretching term, and the tilting term.	116
6.16	Approximate north-south cross-sections using ELDORA analysis through the vortex couplet during the fourth flight leg, displaying vertical vorticity and the stretching term.	117
6.17	Approximate north-south cross-sections using quad-Doppler analysis through the vortex couplet during the fifth flight leg, displaying vertical vorticity and the stretching term.	119
6.18	Approximate north-south cross-sections using quad-Doppler analysis through the vortex couplet during the sixth flight leg, displaying vertical vorticity and the stretching term.	120
7.1	Conceptual model of a vertical vorticity generation via horizontal vortex tilting in a system with along-line wind shear.	130

## LIST OF TABLES

3.1	ELDORA scanning modes during BAMEX.	38
3.2	NOAA P-3 scanning modes during BAMEX.	39
3.3	Time, reference time, and storm motion for the six flight legs.	42

# Chapter 1

## INTRODUCTION

Over the last several decades, observational and modeling studies of mesoscale convective systems (MCSs) have helped both the research and forecasting communities better understand these systems in order to minimize the impacts the storms have on human society and agriculture. Through many detailed studies, it is found that MCSs are initiated in a variety of kinematic and thermodynamic environments resulting in different organizational modes. Much work has been done to better understand the general circulation, precipitation patterns, and classification of MCSs (e.g. Johnson and Hamilton 1988, Houze et al. 1990, and Parker and Johnson 2000). Others studies have focused on the mesoscale circulations within these squall lines (e.g. Weisman and Davis 1998 and Trapp and Weisman 2003). While some MCSs retain linear features, other systems “bow out” with time. The kinematics and radar signatures of bowed convection was recognized and thoroughly investigated by Fujita (1978). He originally termed the phrase “bow echo” to describe curved convective systems, and he was able to associate these types of convective systems with severe winds. Since Fujita’s extensive work, bowed convection has been studied through both simulations (e.g. Weisman 1992, 1993) and eve

observational studies (Fujita and Wakimoto 1981, Przybylinski 1995, and Wakimoto et al. 2006).

While there has been significant research conducted on both MCSs and bow echoes, before the Bow Echo and Mesoscale Convective Vortex Experiment (BAMEX; Davis et al. 2004), there had yet to be a study that detailed convection over the entire Central Plains in the United States that was able to collect highly detailed kinematic and thermodynamic data throughout the entire lifecycle of the MCS. It was the goal of BAMEX to obtain high-resolution data of convective systems over the entire central United States using a variety of stationary [e.g. Weather Surveillance Radar-1988 Doppler (WSR-88D) and meso-networks] and mobile platforms (both airborne and ground-based). This field campaign took place during the spring and summer of 2003, and during the time period there were 18 weather systems that were intensely observed.

On 2-3 June, 2003, as MCS formed over northwest Mississippi and traversed over the northern portion of the state. Being within the sampling region of BAMEX, this particular MCS was sampled for approximately 2 hours (2230 – 0017 UTC) with airborne Doppler radars. Fortuitously, there were two aircraft equipped with dual-Doppler capabilities, which allowed for excellent, high-resolution sampling of this convective system. In addition, data from several ground-based networks were utilized (e.g. WSR-88Ds, mobile rawinsonde launches, and a wind profiler). This convective system proved compelling for several reasons. Several, small-scale (10 – 15 km) embedded bowed segments were observed within the linear convective line before the system transitioned to a bowed convective line. Also, a banded vertical vorticity pattern, oriented parallel to the convective line was observed in the MCS. This vorticity structure

consisted of a strong band of cyclonic vertical vorticity ahead of the convective line with a band of anticyclonic vertical vorticity associated with and behind the convective line. Directly behind (i.e. to the west of) the anticyclonic band of vorticity there was often a weaker band of cyclonic vorticity. The only other published, observational study surrounding a line-parallel, banded vertical vorticity pattern was Biggerstaff and Houze (1991), which investigated the 10-11 June 1985 squall line during the Preliminary Regional Experiment for Stormscale Operational Meteorology (PRE-STORM). Zhang et al. (1989) and Zhang (1992) were able to reproduce the vertical vorticity pattern using model simulations and comment on the mechanisms that formed this observed pattern.

In the following chapter, a review of the literature will be presented, with a focus on both MCSs and bowed convection. Common kinematic and thermodynamic features as well as general structure will be discussed. Special focus will be given to mesoscale vortices that form in both MCSs and bowed convection. Chapter 3 explains the specific datasets and methodologies that were used to investigate the 2-3 June 2003 MCS. A detailed description surrounding dual-Doppler radar technique will be given. In total, the airborne Doppler radar was able to sample the MCS for ~2 hours over six, individual flight passes. A basic overview of the synoptic and mesoscale environment will be given in Chapter 4. Chapter 5 will present a basic overview of the squall line and kinematic fields observed in the 2-3 June 2003 MCS. This will be followed by a thorough description of the observed vorticity patterns seen in the 2-3 June 2003 MCS in Chapter 6. Finally, chapter 7 provides conclusions.

## Chapter 2

### BACKGROUND

#### 2.1 Overview of MCSs

##### 2.1.1 *General definition and structure*

Mesoscale convective systems (MCSs) are a general name given to groups of convective clouds that interact, form widespread precipitation, and last for several hours. The term MCS is a broad term used to classify convection such as bow echoes, squall lines, and mesoscale convective complexes. Houze et al. (1989) and Houze et al. (1990) did extensive research on these systems and classified them as being symmetric or asymmetric. Houze et al. (1989) devised a conceptual schematic of a mature, symmetric MCS with a trailing stratiform region (Fig. 2.1). Symmetric systems generally have convective cells similar in strength along the entire convective line as well as a stratiform region with a secondary reflectivity maximum directly behind the convective line. Similarly, the mid-level cyclonic and anticyclonic circulations that form (discussed in 2.2.3) are of equal strength and size. Houze et al. found asymmetric systems have the most intense convective cells on the southern end of the convective line, while the stratiform region migrates to the northern part of the MCS. In the asymmetric case, the

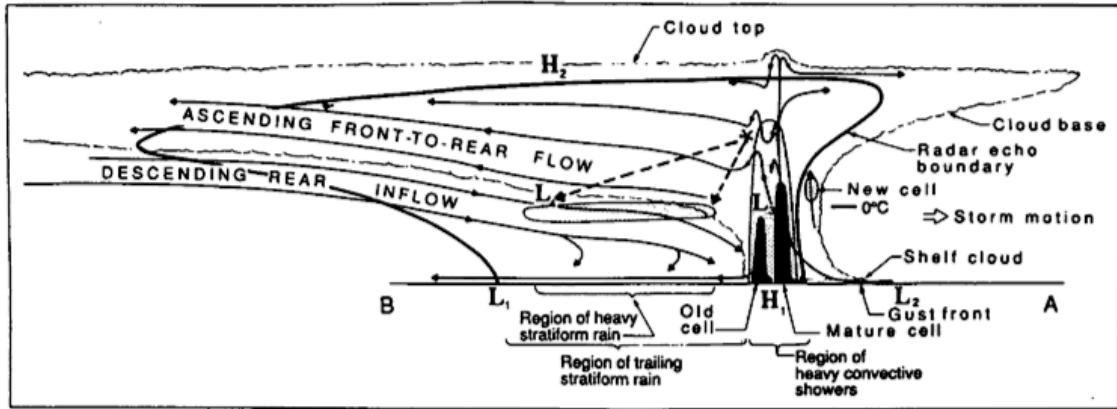


Figure 2.1: Conceptual model of an MCS with trailing stratiform precipitation. The vertical cross-section is perpendicular to the connective line. From Houze et al. (1989).

mid-level cyclonic circulation becomes more dominant than its anticyclonic counterpart. Both observational and modeling studies (e.g. Skamarock et al. 1994, Loehrer and Johnson 1995, Weisman and Davis 1998), have shown that as an MCS matures, it often transitions from symmetric to asymmetric. It is generally accepted that the transition occurs due the Coriolis effect, although along-line flow can contribute to the asymmetry (Hilgendorf and Johnson 1998).

While no two MCSs are alike, surface features such as wake lows, mesohighs, and pre-squall lows appear in most organized convection. The earliest observational studies by Byers and Braham (1949), Fujita (1955), and Fujita (1959) provided the first evidence of these surface features, how they form, how they affect the lifecycle of the convective system. Since the initial investigation of these features, there have been several other studies dedicated to further understanding them (e.g. Johnson and Hamilton 1988; Loehrer and Johnson 1995). Loehrer and Johnson (1995) use observational data from the Oklahoma-Kansas Preliminary Regional Experiment for STORM-Central (OK

PRE-STORM) to investigate the surface features lifecycle characteristics of MCSs.

Figure 2.2 shows the surface features associated with symmetric and asymmetric MCSs.

The mesohigh is often located directly below the downdrafts. In this area, evaporation is causing the air parcel to cool in relation to the surrounding air. As the cool, dense air descends to the surface, hydrostatic balance causes a mesohigh to form in response. While the hydrostatic response is the main contributor to the generation of the mesohigh, nonhydrostatic responses such as the downdraft impacting the ground (Fujita 1955) and precipitation loading (Wakimoto 1982) also act to increase the strength of the mesohigh.

The area of low pressure behind the mesohigh on the back edge of the stratiform region is commonly called a wake low. Johnson and Hamilton (1988) hypothesized that the strength and location of the wake low was strongly influenced by the descending, rear-inflow jet. The air associated with the jet adiabatically warms as it descends, causing a wake low to form due to a hydrostatic response. Its location on the back edge of the stratiform region allows for little interaction with precipitation processes such as evaporative cooling.

The pre-squall mesolow is an area of weak low pressure in front of the convective line. Hoxit et al. (1976) propose that it is formed from adiabatic warming due to subsidence ahead of the convective line. While formed by similar processes compared to the wake low, the pre-squall mesolow is often weaker than the wake low due to weaker dynamics.

Loehrer and Johnson (1995) discovered that 75% of the symmetric MCSs that they studied later transitioned into asymmetric MCSs, showing that symmetric and

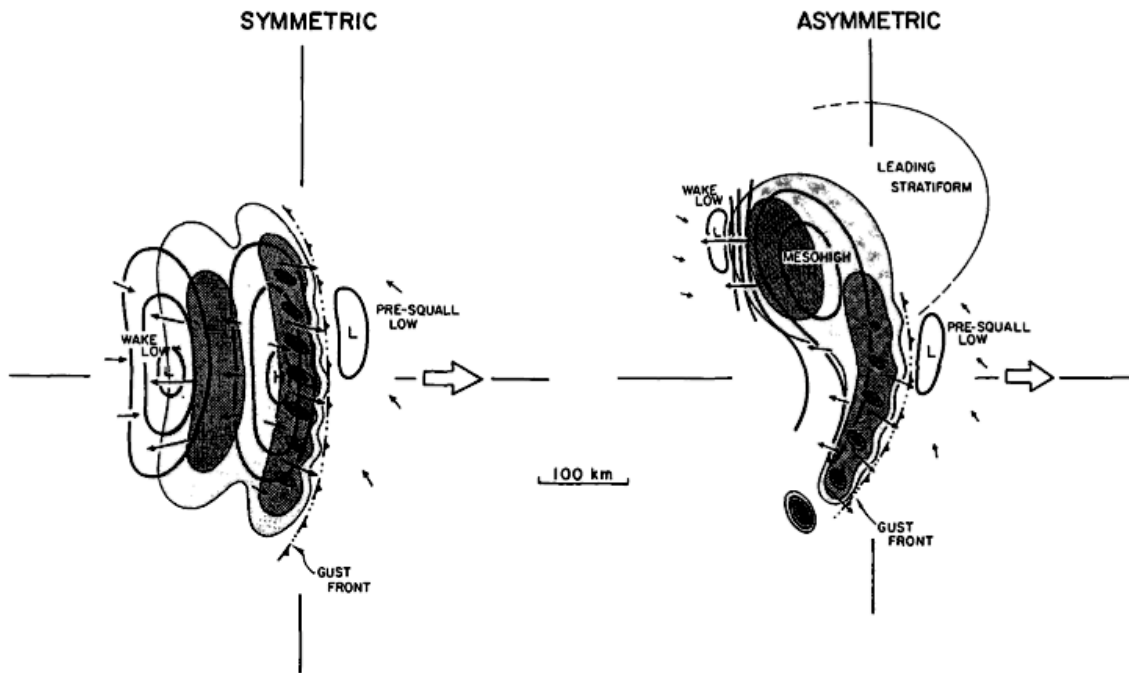


Figure 2.2: Schematic of the surface pressure field and precipitation patterns for symmetric (left) and asymmetric (right) MCSs. The pressure is contoured in 1 hPa intervals. Heavy shaded regions denote reflectivities in excess of 40 dBZ and the lighter shading represents reflectivity fields greater than 30 dBZ. From Loehrer and Johnson (1995).

asymmetric are better referred to as phases of the storm's lifecycle rather than distinct classifications. Revisiting Fig. 2.2 shows the northward shifting of the stratiform region and the southward shifting of the most intense cells in the convective line as the convective system becomes more asymmetric. The mesohigh and wake low are shown to have strengthened and become more concentrated as they shift northward with the stratiform region.

### 2.1.2 Classifications of MCSs

Convective lines often have two main components: a convective region and an associated stratiform region. Parker and Johnson (2000) present a thorough climatology of MCS -

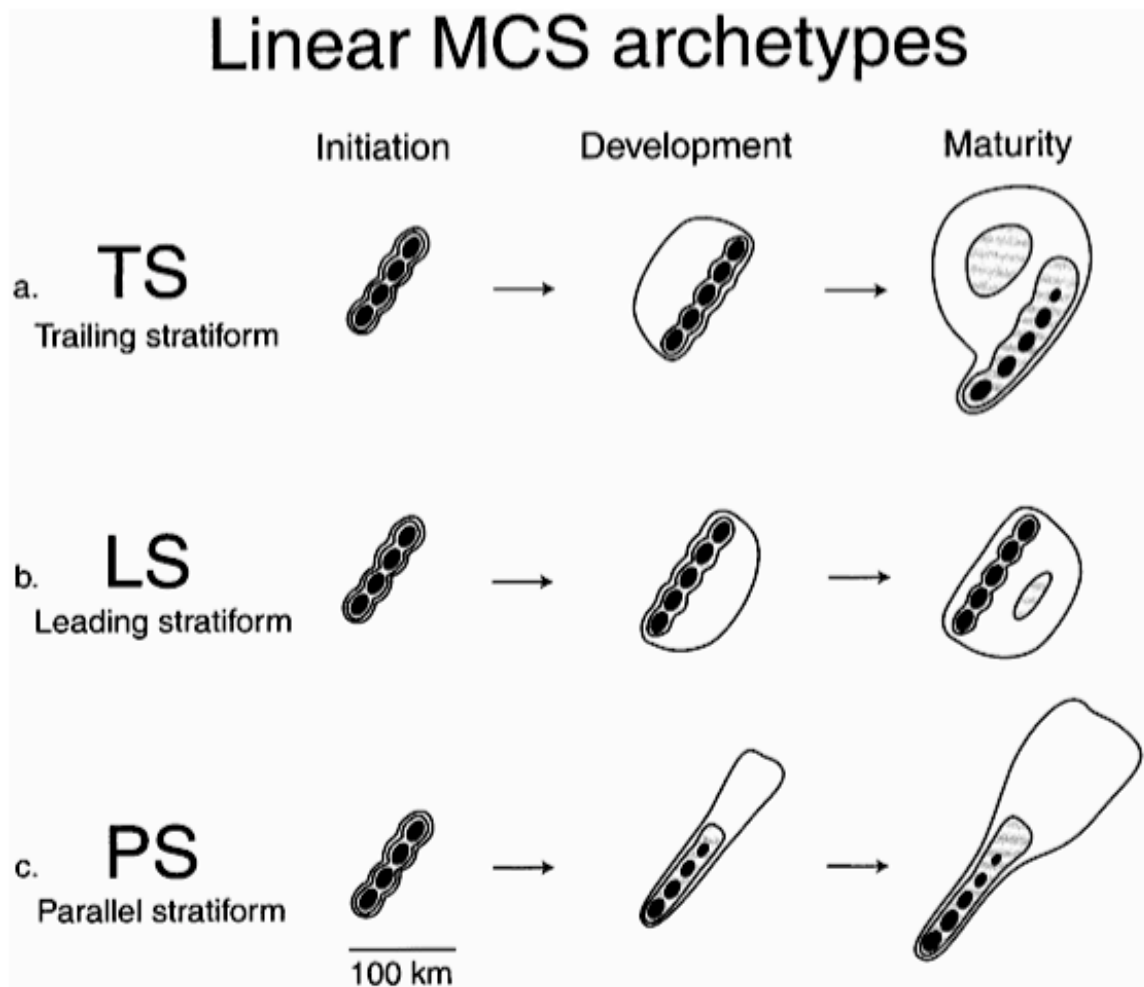


Figure 2.3: Schematics for the three modes of linear MCS: (a) convective line with trailing stratiform (TS), (b) convection line with leading stratiform (LS), (c) convective line with parallel stratiform (PS). From Parker and Johnson (2000).

events and further classify MCSs with regard to the relationship of stratiform region to the convective line (Fig. 2.3): trailing stratiform (TS, stratiform precipitation behind the convective region, similar to Houze et al. 1989), leading stratiform (LS, stratiform precipitation ahead of the convective region), or parallel stratiform (PS, stratiform region positioned along the axis of the convective line). In the 88 MCSs that Parker and Johnson (2000) classified 58% were TS, 19% were LS, and 19% were PS,

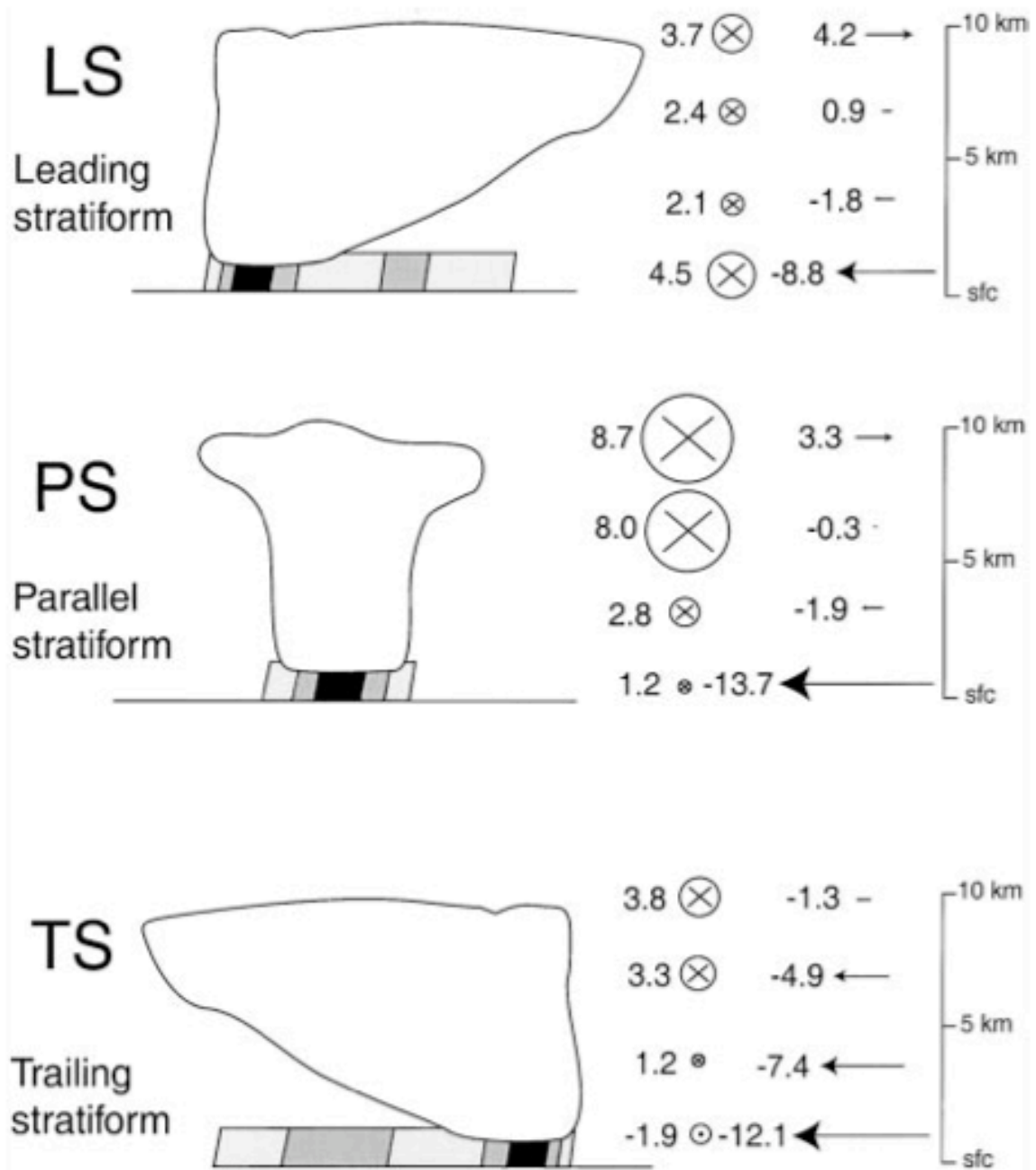


Figure 2.4: Vertical profiles of layer-mean, storm-relative winds for the three modes of MCSs. The layers depicted are 0-1, 2-4, 5-8, and 9-10 km. The shaded areas under the cloud outlines provide typical reflectivity patterns associated with each mode. From Johnson and Parker (2000).

with 4% being unclassifiable. Often times, types of MCSs transitioned from one stratiform regime to another. While TS cases did not readily transform into other modes, 30% of the LS cases evolved to TS, and 58% of PS cases transitioned to TS.

The type of stratiform region that forms is largely dependent on the tropospheric wind shear (Fig. 2.4). TS tend to develop when there are front-to-rear storm relative winds throughout the entire troposphere. The front-to-rear flow allows for hydrometeors to be advected behind the convective line, where the stratiform region develops. TS are typically the longest lasting of the three modes and the fastest moving (12.2 h and  $13 \text{ m s}^{-1}$ , respectively). LS are often associated with weak mid- to upper-level storm relative winds that have rear-to-front flow aloft. LS often exhibited stronger than average rear-to-front flow, which would help advect the hydrometeors ahead of the convective line. On average, these systems are not as long lasting and slower than TS modes (6.5 h and  $7.1 \text{ m s}^{-1}$ , respectively). PS have mid- to upper-level line-parallel storm relative winds and have increasing wind speed from the surface through the troposphere. Hydrometeors are often advected in the direction of the line-parallel flow causing the stratiform region to form parallel to the convective line. This mode often has a similar timescale to the LS mode (6.3 h) and moves on average at  $11.4 \text{ m s}^{-1}$ .

### *2.1.3 Bowing convection*

#### **Definition and structure**

MCSs encompass many types of convection. One such subset of MCS is bowed convection. The investigation of bowing convection began in the 1950s with the rise of observational weather radars. The first two observational studies on bowing convection

described the bowed features and their associations with straight-line wind damage and tornadoes. Nolen (1959) provided the first study of bowing segments embedded in a quasi-linear line of convection. He concluded that portions of the convective line accelerated outward and adjacent portions decelerated, initiating a mesoscale wave-like pattern. This pattern was referred to as a line echo wave pattern (LEWP). Nolen (1959) concluded there was an association between LEWPs and the occurrence of tornadoes. Hamilton (1970) further investigated LEWPs and linked the bowed portion of the convection to straight-line winds as well as tornadoes.

Fujita (1978) provided a landmark paper, in which he termed the bowing convective segments “bow echoes.” Fujita described the evolution and proposed the kinematic structure of a bow echo using radar signatures and surface observations from damage surveys. He documented the stages in the life cycle of a bow echo and notes the location of where damaging, straight-line wind or downbursts and tornadoes are likely to occur (Fig. 2.5). Fujita describes three stages of bow echo development and evolution: tall echo, bow echo, and comma echo. In the tall echo stage, there is a quasi-linear line with strong convection and descending rear inflow beginning to form (this latter feature has been added to Fujita’s conceptual model by Wakimoto 2006a). Fujita proposes that the descending rear inflow can cause damaging straight-line winds at the surface as well as aiding in the bowing of the convective line. The bow echo stage occurs when the convective line transforms into the classic bow echo shape. Fujita (1978) presents evidence of a cyclonic vortex forming on the northern end of the convective line. Weisman (1992, 1993) uses models to simulate an anticyclonic vortex on the southern end of the system in addition to the cyclonic vortex to the north. Due to the location near

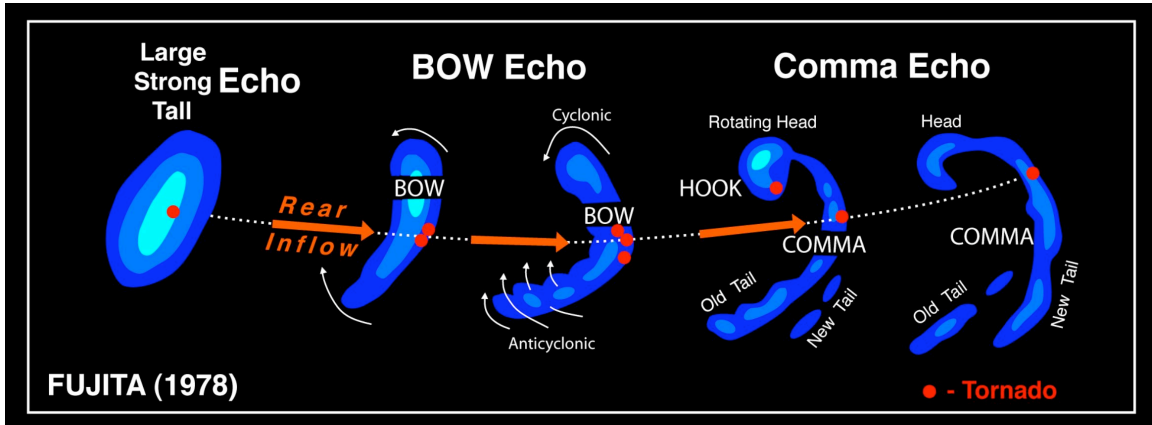


Figure 2.5: Conceptual model of the life cycle of a bow echo. From Fujita (1978) and adapted by Wakimoto (2006a).

the ends of the convective line, the vortex couplet is termed “bookend vortices” (Weisman 1993). The flow from these counter-rotating vortices was shown to enhance the descending rear to front flow as well as cause the convection to bow outward. The bow echo stage can also have intense straight-line winds or tornadoes, most commonly located near the apex of the bow. In the comma or dissipation stage, the Coriolis effect aids in the cyclonic vortex becoming dominant, causing the convective line to take on a comma shape (Weisman 1993). On the northern side, there is often a rotating head at the top of the convective line, and this is another area where tornadoes or straight-line winds are often present.

Since the work of Nolen (1959), Hamilton (1970), and Fujita (1978), there have been many observational and modeling studies to further understand bowing convection. While there is still no concrete definition of a bow echo, the studies from the last several decades have shown many characteristics common to bow echoes, including: being associated with damaging straight-line winds and/or tornadoes, being long-lived (roughly from 3-6 hours), observed on scales between 20-200 km, curved or bowed appearance on radar with a strong reflectivity gradient on the leading edge of convection, a strong rear-

inflow jet and often an attendant rear-inflow notch seen on radar as well as having mid-level bookend vortices (e.g. Fujita 1978, Lee et al. 1992, Jorgensen and Smull 1993, Weisman 1993, Przybylinski 1995, Wakimoto 2006a,b).

### **Classification of bowing convection**

Through the decades of research involving bow echoes, it has been found that there are different modes and size ranges of bow echoes; however, there is still not a universal classification system to define different types of bow echoes. Klimowski et al. (2004) attempt to classify bow echoes from their original convective mode to their resultant mode (Fig. 2.6). The study investigated 273 bow echoes (classified as such through the definition provided in Klimowski et al. 2000) and discovered that bow echoes evolve from three primary modes of initial convection: weakly organized cells, squall lines, or supercells. Once the initial mode was established, the transition to the mature stage was investigated. Klimowski et al. (2004) propose four classifications of bow echoes to account for spatial and reflectivity characteristics: the classic bow echo (BE), bow echo complex (BEC), cell bow echo (CBE), and squall line bow echo (SLBE). BEs are based on the definition given by Fujita (1978) and are described as being larger than a single thunderstorm, not associated with a large linear complex, and are mostly isolated from other organized convection. BECs are defined as an MCS containing a bow echo as the primary mode of convection, but there are also other organized modes present (e.g. supercells). BECs are also associated with derechos, and this is documented in Przybylinski and DeCaire (1985), Johns and Hirt (1987), and Moller et al. (1994). CBEs

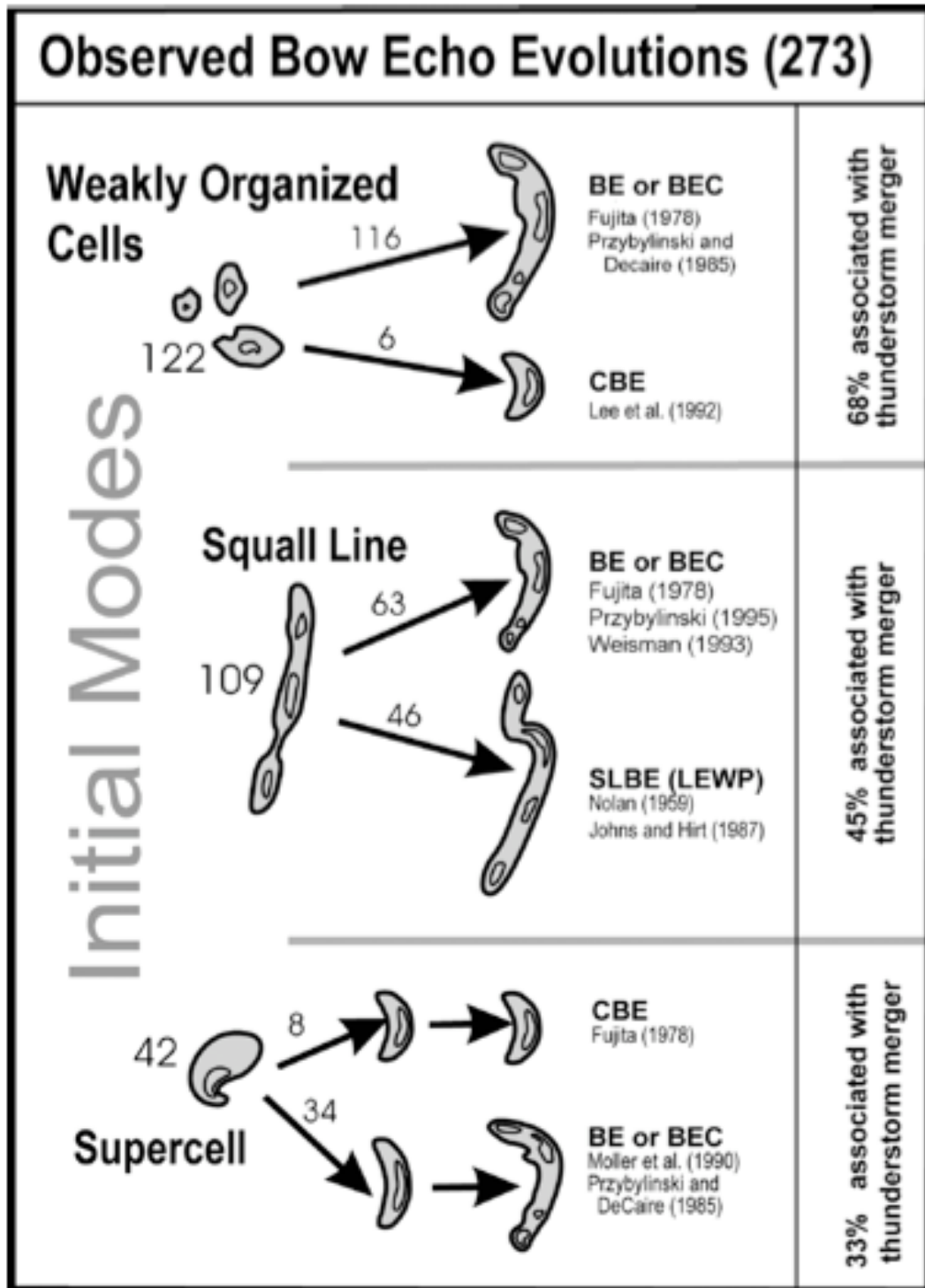


Figure 2.6: Generalized pathways for bowed convection evolution. The initial modes are on the left hand side, and the evolution path is followed by the black arrows. From Klimowski et al. (2004).

Przyblynski and DeCaire (1985), Johns and Hirt (1987), and Moller et al. (1994). CBEs are described as bow echoes on small scales (i.e. 10-25 km) that are isolated and not part of any larger-scale organized convection. This category was adapted from Lee et al. (1992). The SLBE category encompasses bow echoes that are embedded in a quasi-linear convective line and based on studies from Lee et al. (1992) and Przyblynski and DeCaire (1985). This is a common mode associated with serial derechos (Johns and Hirt, 1987) and Nolen's (1959) LEWP classification.

Figure 2.6 shows the generalized evolution for bow echoes, from the initial stage to the mature stage. Klimowski et al. (2004) observed that most bow echoes evolved from weakly organized cells (45%), which was closely followed by squall lines (40%). Only 15% of bow echoes were found to have evolved from supercells. From all initial modes, BEs /BECs were the most common classification of bow echoes (78%). SLBE was found to form 17% of the time, followed by the CBE classification (5%).

Klimowski et al. (2004) also investigated the regional characteristics of bowing convection evolution. The study sectioned the contiguous United States into five main regions (number in parentheses denotes the number of bow echoes observed): the West (2), Northern Plains (120), Southern Plains (40), Mississippi/Missouri Valley (87), and the East (24). Several west-to-east and north-to-south trends were discovered. Bowed convection evolving from squall lines increased from west-to-east. Northern and Southern Plains each saw approximately 32% of bowed convection evolve from squall lines. Over the MS/MO Valley this percentage increased to 47%, and in the East, the percentage climbed to 72%, showing a clear trend for squall lines to be a preferential initial mode as one goes from west-to-east. Trends in the resulting bowed convection

show that more systems evolved into SLBEs as one moves eastward. The more eastern regions, including the MS/MO Valley and the East had a high percentage of bowed convection end as SLBEs (24% and 46%, respectively) compared to the Northern and Southern Plains (14% and 15%, respectively).

## 2.2 Dynamics of MCSs

### 2.2.1 Cold pool and shear interactions

Throughout the last few decades, several theories have been created, tested, and modified in relation to MCS development and maintenance. Rotunno et al. (1988, hereafter RKW) and Weisman et al. (1988) developed one such theory that described how organized convection matured into quasi-two-dimensional, long-lived squall lines. RKW asserts the balance between the ambient vertical wind shear in the low-levels and the system-generated vorticity from the cold pool dictate the longevity and structure of MCSs. Assuming the MCS is a two-dimensional feature, the dynamics can be described through the following set of equations, which relate the generation of horizontal vorticity and the horizontal buoyancy gradients:

$$\frac{d\eta}{dt} = -\frac{\partial B}{\partial x} \quad (2.1)$$

where

$$\eta = \frac{\partial u}{\partial z} - \frac{\partial w}{\partial x} \quad (2.2)$$

where  $\eta$  is horizontal vorticity,  $B$  is buoyancy,  $u$  is the velocity perpendicular to the convective line,  $x$  is the distance perpendicular to the convective line,  $w$  is vertical velocity, and  $z$  is height. Figure 2.7 displays an idealized life cycle for a long-lived

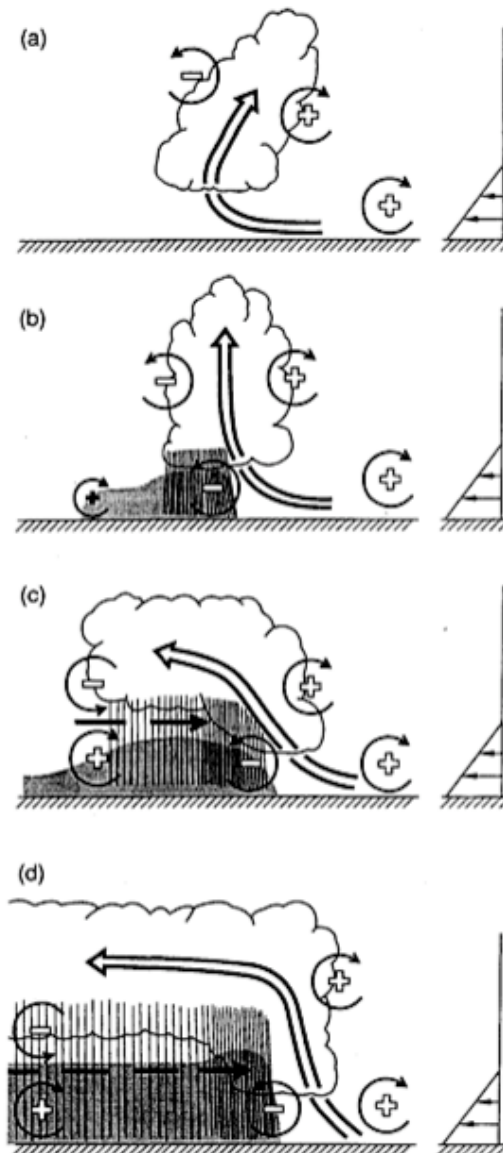


Figure 2.7: Four phases within the evolution of an idealized MCS showing the interaction between the low-level wind shear, the cold pool, and the rear-inflow jet. Note: the updraft is denoted by the wider arrow, the positive (negative) horizontal vorticity is denoted by the circular arrows with a + (-), the rear-inflow jet is denoted by the black, dashed line, and the cold pool is denoted by the grey shaded area. The (a) initial updraft is pointed upshear. In this phase, there is no downdraft and attendant cold pool. (b) the convection is maturing and upright due to the balance between the cold pool and shear. (c) the cold pool expands, allowing it to overtake the ambient shear. This will cause the updraft to tilt downshear. During this phase, the rear-inflow jet is generated. (d) rear inflow jet becomes elevated.

convective system and the interactions between environmental shear, the system-generated cold pool, and the horizontal vorticity.

In the earliest stages, the convective updraft tilts downshear due to being overwhelmed by the ambient vertical wind shear as well as not having a cold pool to help balance the aforementioned shear (Fig. 2.7a). When the system begins to precipitate, a weak cold pool forms causing horizontal buoyancy gradients to form on the front and back edges of the cold pool. These buoyancy gradients generate a circulation on the edge of the cold pool that interacts with the ambient wind shear. The balance between the cold pool circulation and the ambient shear cause the updraft to become upright (Fig. 2.7b). As the system strengthens, the cold pool also strengthens. The cold pool induced circulation begins to overwhelm the ambient vertical shear causing the system to be tilted upshear with the updraft slanting up and over the cold pool (Fig. 2.7c). It is during this phase when the rear-inflow jet is generated. If the environmental conditions permit, the rear-inflow jet becomes elevated and a new balance between the cold pool and ambient vertical wind shear is attained (Fig. 2.7d).

This concept of an optimal balance between the cold pool and vertical wind shear has been strongly debated by Evans and Doswell (2001) and Coniglio et al. (2004). These observational studies focused on the environmental conditions associated with derechoes (intense, fast-moving storms, often associated with widespread, damaging winds). Environmental soundings were used to determine low-level shear and instability as well as extract thermodynamic information to determine the cold pool strength. These values were then correlated throughout the lifecycle of the convective systems to see if there was indeed an optimal state that existed to promote the growth and maintenance of

the storm. In contrast to RKW, their results showed almost no correlation between the low-level vertical wind shear and the cold pool. In fact, the derechos often formed when there was less than  $15 \text{ m s}^{-1}$  of vertical shear, which is established by RKW as being on the lower threshold needed to balance the circulation induced by the cold pool. While there was weaker low-level shear in certain cases, both Evans and Doswell (2001) and Coniglio et al. (2004) found there to be moderate-to-strong deep layer shear. Weisman and Weisman and Rotunno (2005) replied stating that the calculations were done using unrealistic cold pool temperatures, causing the low correlations between the cold pool and the vertical shear. They also noted that derechos are a small subset of MCSs, and to fully test RKW with observations, a wider range of MCSs should be used. While both proponents and questioners of RKW make valid points, it is important to remember that RKW is simply a theory, which can be helpful in understanding the basic principles of convection.

### *2.2.2 Generation and maintenance of rear-inflow*

The development of the rear-inflow jet is directly related to the relationship between horizontal buoyancy gradients and horizontal vorticity, revisited in (2.1). As described above and seen in Fig. 2.7, the updraft transitions from tilting downshear to a more aligned, upshear configuration. When the updraft tilts upshear, the horizontal buoyancy gradients along the backside of the convective system generate a vertically aligned horizontal vorticity couplet, which produces the rear-inflow. As seen in Fig. 2.7c, the horizontal vorticity couplet induces a rear-to-front flow near the upper boundary of the cold pool. This inflow is accelerated from rear-to-front, and the strength of the jet is

directly connected to the strength of the horizontal buoyancy gradients. These gradients are dictated by the strengths of the surface cold pool and the warm plume directly above it.

Rear-inflow jet strength is also dependent on the ambient low-level vertical wind shear and the instability (Weisman 1992). Stronger low-level vertical wind shears can enhance the lifting on the leading edge and allow for a more-elevated rear-inflow. Larger CAPE values can increase the buoyancy in the front-to-rear ascending flow, which can act to spread the warmer air rearward, above the cold pool. A warmer plume of air above the cold pool will increase mid-level convergence and horizontal buoyancy gradients, which will cause a more-elevated, stronger rear-inflow jet. Conversely, environments with weak vertical wind shear and/or low instability allow for the rear-inflow jet to descend to the surface and spread outward.

### *2.2.3 Generation and maintenance of mesoscale vortices*

#### **Mid-level vortices**

Fujita (1978) first noted the presence of mid-level cyclonic and anticyclonic circulations on the northern and southern ends of the convective system, respectively. These circulations were associated with bowed convective systems, which were on the scale of 20 to 120 km. Since Fujita (1978), there have been numerous studies showing the existence of mid-level mesoscale vortices. These vortices have been observed and modeled over a wide range of horizontal length (tens to hundreds of kilometers) and time scales (several hours to days). In addition to differing temporal and spatial scales, mid-level vortices have been observed within different types of convection, including bow

echoes, convection with smaller-scale bowing segments, and quasi-linear convective systems.

Weisman (1993) used a three-dimensional, idealized model to simulate convective systems in environments with differing low-level vertical wind shear and CAPE. The models produced 10 to 30 km wide cyclonic and anticyclonic mid-level vortices on the northern and southern ends of the convective line, respectively, both with and without Coriolis forcing applied. Without the presence of Coriolis forcing, the cyclonic and anticyclonic vortices grew and strengthened similarly with time and maintained a symmetric shape. With the Coriolis forcing, the convection shifted from a symmetric to asymmetric shape over the lifecycle, and the cyclonic vortex grew spatially larger and strengthened more than the anticyclonic vortex over time (e.g. ~4 hours). Simulations by Weisman (1993) also showed that the mid-level vortex couplet was able to concentrate the flow within the rear-inflow jet (discussed in 2.2.2), and up to 30-50% of the strength of the rear-inflow jet can be attributed to the concentrated flow associated with the vortex couplet.

Weisman (1993) proposes the initial source of the vertical vorticity needed for vortex generation originates from the tilting of the horizontal vorticity associated with a downdraft in the westerly, ambient shear (Fig. 2.8). Weisman (1993) suggests the vortex couplet begins to form when the downdraft tilts the vortex lines downward, creating a cyclonic vortex to the north of the downdraft and an anticyclonic vortex to the south (Fig. 2.9b).

Weisman and Davis (1998) revisit the simulations from Weisman (1993) to further investigate how vertical vorticity is generated and maintained in MCSs with

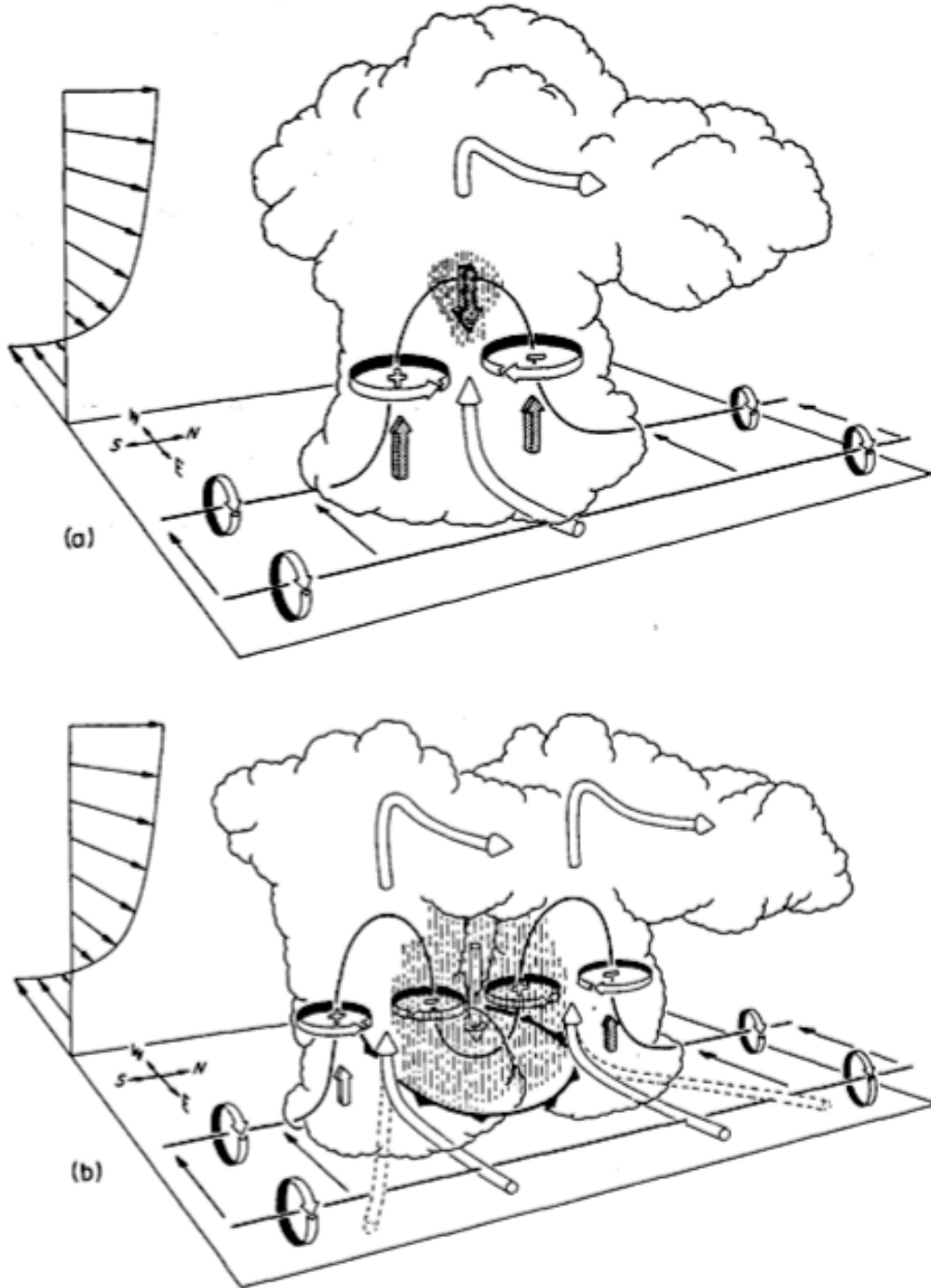


Figure 2.8: Schematic showing how the horizontal vorticity is tilted when it interacts with the downdraft within westerly ambient wind shear. Note: circular arrows represent the airflow, the black lines represent vortex lines, which rotate with the direction of the circular arrow surrounding the vortex line, and the shaded arrows represent the updraft and downdraft growth. (a) initial stage of vortex development (b) splitting stage, where the cyclonic and anticyclonic vortices form.

attendant mid-level vortices. In their idealized model simulations, there is no vertical vorticity initially present, which implies that vertical vorticity generation occurs by tilting the horizontal vorticity into the vertical. They assert this horizontal vorticity be tilted into the vertical either by system-generated (easterly) or from ambient shear (westerly) (Fig. 2.9). Figure 2.9a shows how storm-generated easterly shear produced near the cold pool/updraft interface can be tilted upward by a localized updraft thereby creating a vertical vorticity couplet, and Fig. 2.9b shows how the downward tilting of horizontal vorticity associated with ambient westerly shear by a localized downdraft (i.e., the mechanism depicted in Fig. 2.8) can create a vortex couplet of the same sign. Namely, cyclonic and anticyclonic rotation centers are present on the northern and southern ends of the convective line, respectively, for both the easterly and westerly shear.

Weisman and Davis (1998) simulated vortices on both the system- and subsystem-scale, and they concluded that each had a different source of vertical vorticity. The sub-system vortices are on the scale of the smaller convective segments within the larger convective line, and they are mostly contained to the low-levels (which will be discussed in the following section). The system-scale vortices are on the same scale as the convective system and are predominantly in the mid-levels. Vertical vorticity generation in conjunction with system-scale vortices occurs when system-generated horizontal vorticity produced near the cold pool-updraft interface is tilted upward into the vertical. This allows a cyclonic vortex to form on the northern end of the convective line, while an anticyclonic vortex forms on the southern end. While the focus of their study concentrated on non-Coriolis force simulations, they did comment that when Coriolis effects were added, the system appearance and vertical vorticity distribution began to

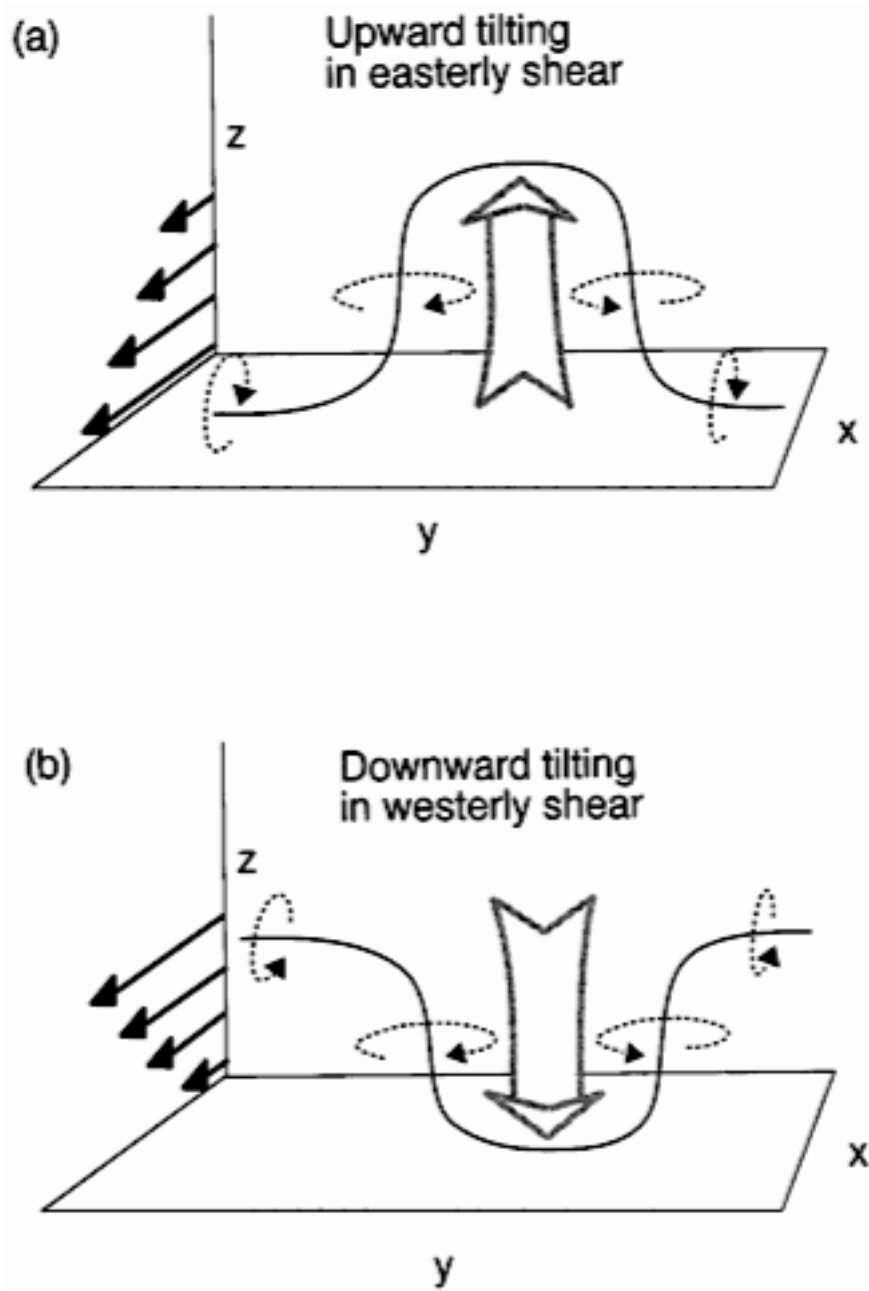


Figure 2.9: Schematic of the tilting of horizontal vorticity into the vertical via vortex tilting. (a) shows easterly shear (produced near the cold pool/updraft interface) and the upward tilting it causes (b) shows the westerly shear (from the ambient wind shear) and the downward tilting it causes.

change after 4.5 hours. The changes are due in part to the system-scale mid-level convergence of Coriolis rotation, which will cause the cyclonic vortex to become more dominant than the weakening anticyclonic vortex. This change in structure can be seen as the system transitions from symmetric to asymmetric.

In addition, Skamarock et al. (1994a) also modeled the ability for mid-level mesoscale vortices to form in a finite convective line. While Weisman (1993) study modeled environments with strong low-level shear, the Skamarock et al. (1994a) showed the ability for convective systems with weak low-level shear (i.e.  $10 \text{ m s}^{-1}$  over the lowest 2.5 km AGL). Similar to Weisman (1993), when Coriolis forcing was applied, the cyclonic vortex become the stronger of the vortices and took on an asymmetric appearance. A difference between Skamarock et al. (2004) and Weisman (1993) was the location of the vortices. It was hypothesized that due to the weaker shear, the vortices retreated away from the convective line and toward the stratiform region. In Weisman's stronger-shear environment, the mid-level vortices stayed anchored near the convective line.

Whether the horizontal vorticity is tilted in easterly shear near the updraft or westerly shear near a downdraft, the modeling studies mentioned above have shown the mid-level vorticity structure to have cyclonic (anticyclonic) vertical vorticity concentrated in the northern (southern) portion of the convective system. This vertical vorticity structure is both well observed and well accepted. However, Biggerstaff and Houze (1991; hereafter BH91) used observational data to examine the mid-level vorticity structure of a squall line that had a line-parallel banded vorticity structure, as opposed to the vorticity concentrating on the northern and southern edges of the convection. A band

of anticyclonic vorticity was observed directly between the main convective line and the secondary band of enhanced reflectivity associated with the stratiform region. This band was situated between two bands of cyclonic vorticity. A strong band of cyclonic vorticity was located on the leading edge of the convective line, and a weaker band was located in the stratiform region directly behind (i.e., to the west) the band of anticyclonic vorticity. Unlike most convective systems, which have line-perpendicular vertical wind shear, this particular convective system was in an environment with predominantly line-parallel wind shear, which was hypothesized to be the reason for the banded structure.

BH91 focused on determining the how the banded structure behind the convective line and in the stratiform region formed. More specifically, the tilting and stretching terms from the vertical vorticity equation were used to diagnose the origins and maintenance of the banded vorticity structure. They discovered the anticyclonic band occurred where there was strong downward tilting due to the vertical velocity gradient between the strong convective updraft and the transition zone downdraft. This downward tilting was dominant enough to change the sign of the vertical vorticity from positive to negative as air flowed through the convective region. In conjunction, a negative stretching term collocated in this region and acted to concentrate and amplify the anticyclonic vorticity. While the tilting and stretching terms were of the same order of magnitude, the tilting term was a factor of 2-3 stronger than the stretching term. Similarly, the cyclonic band of vorticity located near the back edge of the stratiform region can be explained by the tilting and stretching of vorticity. The gradients of vertical motion between the descending rear-inflow and mesoscale downdraft allow for upward tilting of vorticity in this region. Stretching from the within the rear-to-front flow

helps concentrate the cyclonic vorticity; however, contributions from stretching are on a much smaller-scale than contributions from tilting. Due to an insufficient, high-resolution network in the proper location, Biggerstaff and Houze were unable to thoroughly investigate the strong cyclonic vorticity band ahead of the convective line. However, they do offer a hypothesis to its formation. They believe the band is generated and maintained by strong upward tilting due to vertical velocity gradients associated with the strong convective updraft.

The same squall line that was investigated by BH91 was simulated by Zhang et al. (1989) and Zhang (1992). Zhang et al. (1989) was able to correctly simulate the line-parallel, banded vorticity pattern, and Zhang (1992) asserted that the cyclonic and anticyclonic vorticity bands associated with the convective line were generated by first by the upward tilting then subsequent downward tilting of the environmental horizontal vorticity. Stretching effects then amplified this vorticity pattern.

### **Meso- $\gamma$ vortices**

Both observational and modeling studies have shown the ability for convection to produce meso- $\gamma$  vortices (2–40 km) in both the low-levels (e.g. Weisman and Trapp (2003), Trapp and Weisman (2003), and Wakimoto et al. (2006b)) and in the mid-levels (e.g. Weisman and Davis (1998)). In a study discussed in the previous section, Weisman and Davis (1998) simulate mid-level subsystem-vortices, and these vortices only formed in the stronger, deeper shear simulations, and they were associated with a cyclonic updraft-anticyclonic downdraft structure, similar to supercells. While there was a general bowing of the entire convective system, the system-scale vortices were directly related to

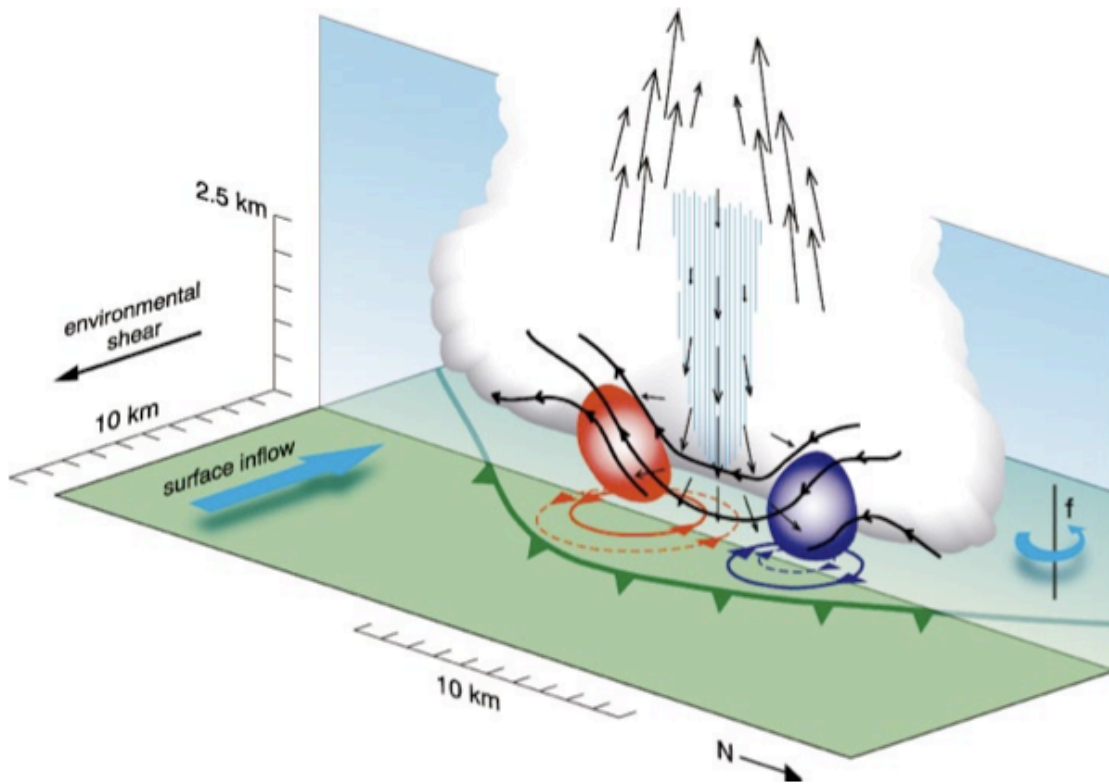


Figure 2.10. Schematic proposed by Trapp and Weisman (2003) showing the proposed mechanism for low-level mesovortexgenesis. Note: the green line is the gust front, the red area is the cyclonic vorticity, the blue area is the anticyclonic vorticity, the arrows represent the motion vector on the vertical plane, and the black lines are the vortex lines.

small-bowed segments throughout the entire bowing line. Weisman and Davis (1998) propose a different source of vertical vorticity generation for these vortices.

It is hypothesized by Trapp and Weisman that vertical vorticity is generated via tilting of the ambient horizontal vorticity, as opposed to the mid-level vortex couplet, which is produced by system-generated horizontal vorticity. The nature of the cyclonic updraft-anticyclonic downdraft might promote the convective line into breaking up into the smaller-bowing segments seen in the model simulations.

Later modeling studies by Trapp and Weisman (2003) and Weisman and Trapp (2003) use an idealized, three-dimensional model to simulate convective lines to better

understand low-level meso- $\gamma$  vortices genesis and their effects on severe wind damage at the surface. Several observational studies have shown more intense swaths of damage embedded within larger areas of weaker damage due to the existence of such vortices (DeWald and Funk 2000; Miller and Johns 2000). While these smaller-scale low-level vortices were embedded within larger-scale convection, it is theorized that they had a different mode of generation than the associated larger-scale, mid-level vortex. Trapp and Weisman (2003) proposed a schematic to show how the vorticity is generated. As seen in Fig. 2.10, the initial vortex couplet is produced when the horizontal vorticity associated with the gust front is tilted via a localized downdraft near the gust front/cold cool intersection. Due to the Coriolis effect, the cyclonic vortex will begin to amplify, while the anticyclonic vortex will diminish. Trapp and Weisman (2003) propose that the ensuing cyclonic circulation will cause a downward-directed pressure gradient force. Within this circulation is where they believe the strongest surface winds will be. Throughout all of their simulations, Trapp and Weisman (2003) found an overwhelming preference for cyclonic vortices to form and mature, while anticyclonic vortices were not sustained due to the presence of the Coriolis effect.

Wakimoto et al. (2006b) develops another hypothesis regarding low-level mesovortexgenesis. While Wakimoto et al. (2006b) and Trapp and Weisman (2003) agree that low-level mesovortices within bowing convection form when there is strong low-level vertical shear, their conceptual models of how the vortices form are divergent. Both theories realize the importance a downdraft tilting the vorticity near the leading edge of the cold pool, but the mechanism that produces the downdraft is debated. Trapp and Weisman's theory has a downdraft near the leading line of the storm that tilts the

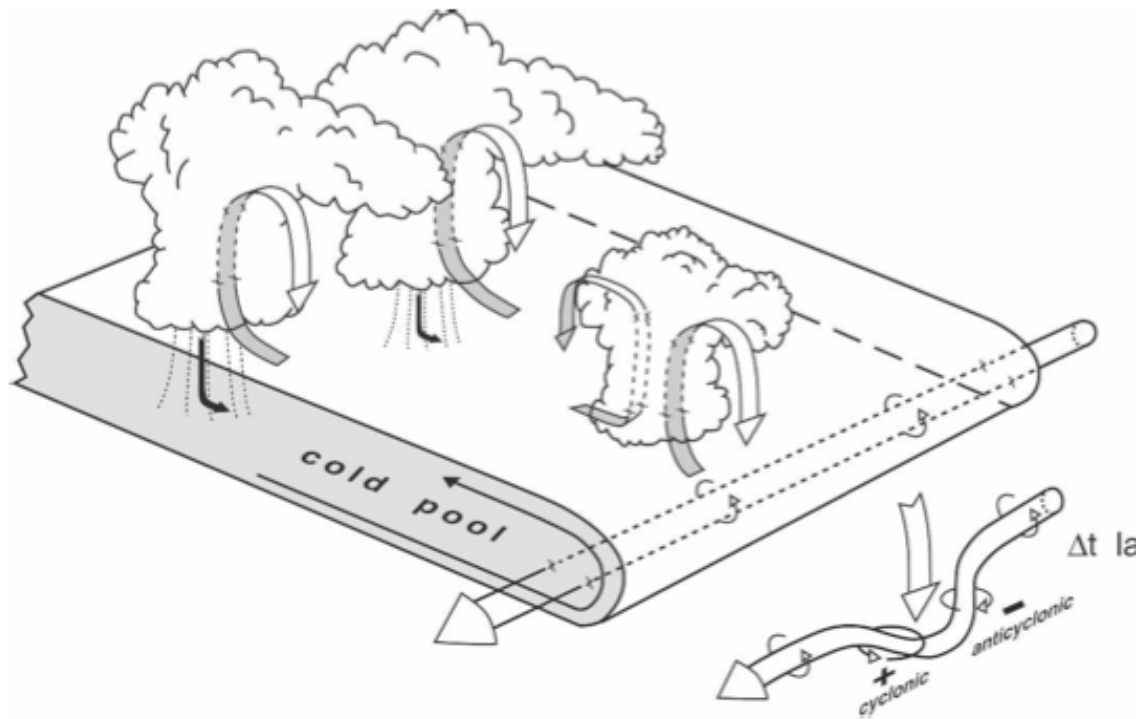


Figure 2.11: Schematic proposed by Wakimoto et al. (2006b) to show the origin of the vortex couplets along the outflow boundary. Note: the circular arrow represents the vortex tube. The distortion of the vortex with time can be seen in the lower right portion of the figure.

horizontal vorticity into the vertical. This downdraft is proposed to form by the evaporation of rain as it falls to the ground. Wakimoto et al. (2006b) suggests that cells near and ahead of the convective line were still in their formative, updraft-dominated stages, which would mean the downdrafts were not associated with precipitation processes. Instead, Wakimoto et al. (2006b) suggests this downdraft is mechanically forced in order to balance the buoyant, convective updraft. The conceptual schematic can be seen in Fig. 2.11.

### 2.3 Summary

As presented in the above literature review, extensive research has been conducted to better understand MCSs. From quasi-linear convection to bowing convection, MCSs

have been shown to encompass a variety of spatial and temporal ranges as well as modes of evolution. A variety of modeling studies has been performed that help to lay a general framework for better understanding how changes in the environment or changes within the convection itself can affect the mode and evolution of the MCS. While observational data are often used to promote and validate results seen in simulations, there are also occasions when observational data can show non-idealized phenomena that veer from previously simulated results or the theories. For example, there is still debate over RKW theory and the observations of cold pool/vertical shear balance (Evans and Doswell 2001 and Coniglio et al. 2004). Also, Wakimoto et al. (2006b) and Trapp and Weisman (2003) both agree the downdraft tilting near the outflow boundary is imperative to mesovortexgenesis; however, their thoughts on how the downdraft is generated are divergent. There are also phenomena that have been modeled but have not been thoroughly studied in observational data (e.g. small-bowed segments of convection). In addition, the observational and modeling studies mentioned above often have line-perpendicular shear that aids in generating cyclonic (anticyclonic) vertical vorticity in the northern (southern) end of the convective line. In BH91, a convective event that had an along-line shear component contained a banded vertical vorticity structure. It was successfully reproduced in simulations (Zhang et al. 1989 and Zhang 1992), leading to questions if the environmental shear affects the vertical vorticity patterns in MCSs. Similarly, many of the studies focus on convection in the northern and central United States, and while this is where a large portion of severe convection occurs, it is imperative to study convective events in the southeastern and eastern United States as well. It is of the utmost of importance to continue to model theories behind modes and

evolution of convection, but it is of equal importance to continue to bridge the gap between simulated and observed data.

## Chapter 3

### METHODOLOGY AND DATA ANALYSIS

#### 3.1 Data Sources from BAMEX

Data for this study were collected during the Bow Echo and Mesoscale Convective Vortex Experiment (BAMEX), which took place from May to July 2003. The field campaign was based out of MidAmerica St. Louis Airport in Mascoutah, Illinois, and its domain focused over the entire Midwest region. A map of the BAMEX region is provided in Fig. 3.1. The domain was chosen for two main reasons: there is a high climatological frequency of bow echoes and other mesoscale convection over the area (Johns and Hirt 1987; Evans and Doswell 2001), and there is also a dense observing network already in place. The network includes surface mesoscale-networks, WSR-88D radars, scheduled rawinsonde launches, and wind profilers. The goal of BAMEX was to use the preexisting observing networks as well as incorporate various mobile platforms to better sample and understand bow echoes, MCVs, and other mesoscale convection (Davis et al. 2004). The use of mobile platforms was essential in fulfilling the goals of BAMEX, as MCSs often traverse an area several hundred kilometers for multiple hours, making it difficult to continuously collect data throughout the life cycle of the convection. While

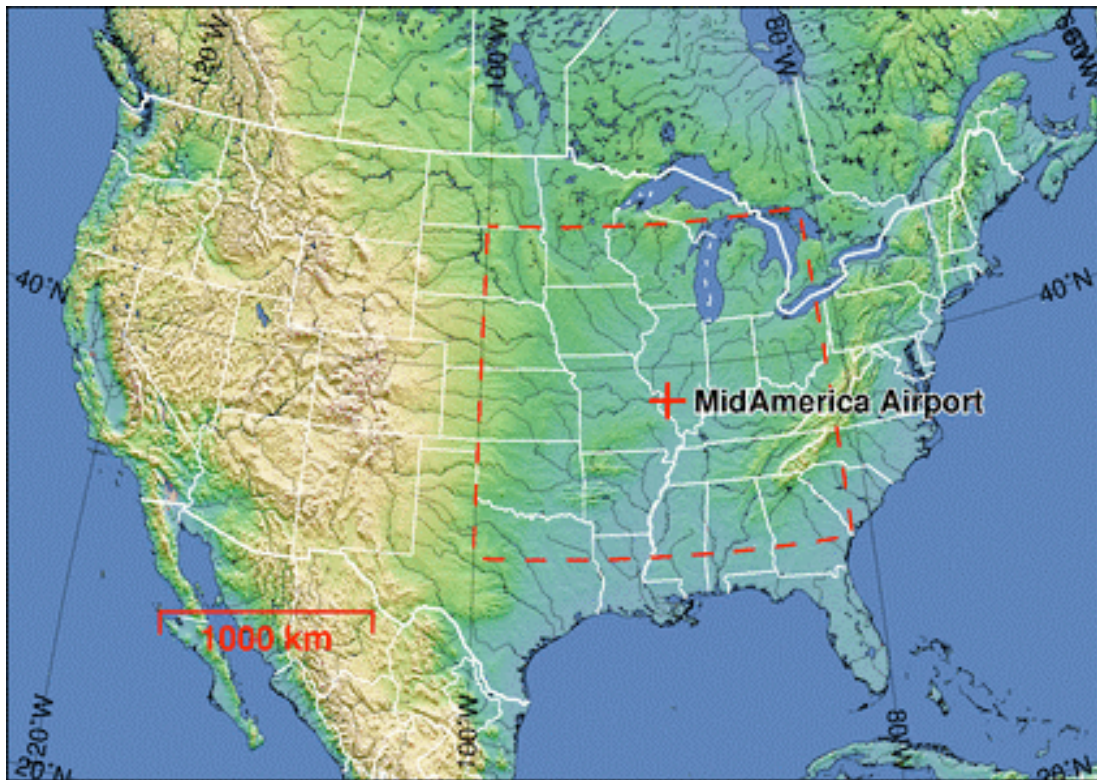


Figure 3.1: Red-dotted lines enclose the area covered by the BAMEX field campaign. It was based out of MidAmerica St. Louis Airport in Mascoutah, Illinois. Found online at: <http://catalog.eol.ucar.edu/bamex/>.

there have been many observational studies focusing on MCSs, there are minimal studies that capture the majority of the convection's life cycle on multiple meteorological scales. Through the use of mobile observing systems (ground based and airborne) and stationary observing networks, BAMEX was able to collect high-density kinematic and thermodynamic data for 18 intensive observing periods (IOPs) during the spring and summer of 2003. All data (e.g. airborne radar data, WSR-88D data, mobile soundings, wind profile data, etc.) collected from the project have been archived and can be obtained at [http://data.eol.ucar.edu/master\\_list/?project=BAMEX](http://data.eol.ucar.edu/master_list/?project=BAMEX), which is maintained by the Earth Observing Laboratory (EOL) at the National Center for Atmospheric Research (NCAR).

### *3.1.1 Ground-based observation networks*

Ground-based observation systems (GBOS) during BAMEX provided high-resolution data, both spatially and temporally. GBOS data used in this study include radar data and rawinsonde data from the National Weather Service (NWS), wind profiler data from the National Oceanic and Atmospheric Administration (NOAA) Profiler Network (NPN), mobile rawinsonde data from the Mobile GPS/Loran Atmospheric Sounding System (MGLASS) units from NCAR, and surface meteorological observations from various networks.

Specifically, level III data from Columbus Air Force Base, MS (KGWX) is used to compare to the airborne radar data as well as obtain a larger-scale view of the MCS; unfortunately, level II data was not available for this time period. In addition to data from KGWX, NOWRAD data is also used to gain a regional perspective of the weather that was occurring during the studied event. MGLASS units were able to sample the pre-convective region at 1735, 1757, 1903, and 2208 UTC. These soundings, in conjunction with the wind profiler in Okolona, MS, assisted in providing both a high-resolution thermodynamic and kinematic profile of the atmosphere before and during the 2-3 June 2003 MCS. Chapter 4 will provide an in depth look at the data collected by these platforms.

### *3.1.2 Airborne platforms*

Aircraft study of weather phenomena is especially useful because it allows for the collection of data over areas that cannot always be sampled by ground-based radars. Also, airborne radar data are more coherent than using a series of ground-based radars if

the weather phenomenon covers a large area over time. The airborne platforms used during the field campaign included P-3 aircraft from NOAA and the Naval Research Laboratory (NRL) and a Learjet from Weather Modification, Inc. NCAR and NOAA both maintain P-3's capable of mounting fore and aft-scanning X-band Doppler radars on the tail of the aircraft. The mounted radar on NRL's P-3 is called the Electra Doppler Radar (ELDORA). Both ELDORA and NOAA P-3 radar were used during BAMEX to provide multiple-Doppler radar data.

### **ELDORA**

ELDORA is a fore and aft-scanning X-band (3.22-cm) Doppler radar that is mounted on the tail of research aircraft (Hildebrand and Mueller 1986; Frush et al. 1986). The geometry of a tail-mounted fore and aft-scanning radar can be viewed in Fig. 3.2. A complete list of ELDORA's scanning parameters used during BAMEX is seen in Table 1. The two antennas scan vertically and are pointed  $\sim 18.5^\circ$  slightly fore and aft of normal to aircraft. During BAMEX, ELDORA's fore and aft transmitted pulses were each broken up into five sub-pulses, all at slightly different frequencies. The measurements from the ten different frequencies are then averaged in order to produce the final output measurements. Due to this process, ELDORA is capable of resolving features at a much higher resolution (which is also due to fast antenna scan rate) and having a smaller velocity error variance. Also, the staggered transmitted pulses allowed for extended unambiguous Nyquist velocities, which dramatically decrease problems with radial velocity folding. Also, as seen in Table 1, ELDORA has a low minimum detectable

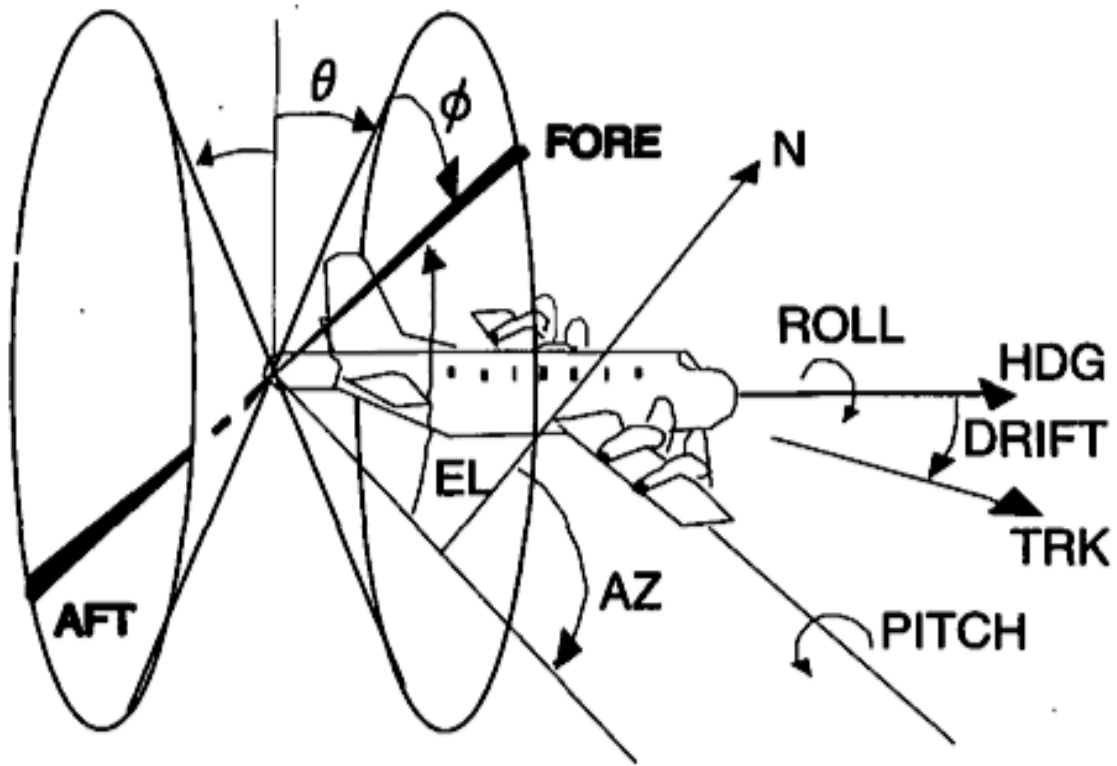


Figure 3.2: Airborne dual-beam radar system schematic from Chong and Campos (1996). Description of names/abbreviations: AFT – aft pointing beam and sweep area, FORE – fore pointing beam and sweep area,  $\theta$  - antenna angle fore or aft of airplane,  $\phi$  - rotation angle of the beam, EL – elevation angle, relative to Earth’s surface, AZ – azimuth angle, relative to Earth’s surface, ROLL – roll of the aircraft, HDG – heading of the aircraft, DRIFT – drift of the aircraft, TRK – track of the aircraft, and PITCH – pitch of the aircraft.

signal, which allows for clear-air returns to be detected. For the reasons listed above, the aircraft mounted with ELDORA usually flew in front (i.e. to the east) of a convective system because it can detect gust fronts and mesovortices that may form on the leading edge of the storm, as well as capture the kinematic structure directly behind the convective line. During BAMEX, the NRL P-3 flew ahead of the convective line at an altitude around 1.5 km MSL. To capture the convection on acceptable spatial and temporal scales, flight legs around 50-100 km are considered optimal. A flight leg is the quasi-linear path the aircraft takes to sample the convection in one direction. Ideally,

Table 3.1. ELDORA scanning modes during BAMEX.

Antenna rotation rate ( $^{\circ} \text{ s}^{-1}$ )	140
Number of samples	24
PRF (Hz)	2000/2500
Gate length (m)	150
Sweep-angle beam spacing ( $^{\circ}$ )	1.4
Along-track data spacing (m)	$\sim 300$
Maximum range (km)	60
Maximum unambiguous velocity ( $\pm \text{m s}^{-1}$ )	77.2
Minimum detectable signal at 10 km (dBZ)	$\sim -15$

flight legs are flown as parallel to the convection as possible to keep errors associated with radar geometry to a minimum.

ELDORA has one major drawback that must be considered. Since it is an X-band radar, it is heavily attenuated in strong convection. Since ELDORA was sampling areas of intense convection during BAMEX, the area several kilometers behind the convective line often went completely undetected. For this reason, it was beneficial to have the NOAA P-3 fly behind the convective line. This flight pattern is especially preferred in systems that have trailing stratiform precipitation.

For the BAMEX field campaign, ELDORA collected data that contained radial reflectivity, radial velocity, spectral width, and normalized coherent power. The dataset contained raw, unedited data fields as well as information from the airplane's inertial navigation system (INS) and global positioning system (GPS).

### **NOAA P-3**

The NOAA P-3 (Jorgensen et al. 1983) contains two radars used for research: the fore and aft-scanning radar mounted on the tail and a C-band radar on the lower fuselage. The

Table 3.2: NOAA P-3 scanning modes during BAMEX.

Antenna rotation rate ( $^{\circ} \text{ s}^{-1}$ )	60
Number of samples	32
PRF (Hz)	2133/3200
Gate length (m)	150
Sweep-angle beam spacing ( $^{\circ}$ )	0.75
Along-track data spacing (m)	$\sim 1200$
Maximum range (km)	46.8
Maximum unambiguous velocity ( $\pm \text{m s}^{-1}$ )	51.5
Minimum detectable signal at 10 km (dBZ)	$\sim 0$

X-band (3.2-cm) radar was used for the multiple-Doppler analysis, and the C-band radar was used to see the planar view of the MCSs. A full list of the NOAA P-3's scanning parameters can be seen in Table 2. Unlike ELDORA, there is only one transmitter and antenna for the fore- and aft-scanning. Therefore, both beams must be transmitted from the same antenna. For this reason, the resolution of the NOAA P-3 data is more coarse than the ELDORA data. Like ELDORA, the NOAA P-3 also uses staggered transmitted pulses to increase the unambiguous Nyquist velocities.

In BAMEX, the NOAA P-3 flew behind (i.e. to the west of) the convective line in or near the stratiform region around 3-4 km MSL. Since the sensitivity of the NOAA P-3 radar is less than that of ELDORA, it cannot detect clear-air echoes; therefore, it is suited well to fly in the stratiform region. Vertical spiral legs were occasionally flown in order to provide important microphysical data in the stratiform region. When not flying in the spiral flight pattern, the NOAA P-3's main goal was to collect data from the stratiform region by completing quasi-linear flight legs parallel to the convection, similar to the flight patterns of ELDORA. The goal of the quasi-linear flight legs was to detect the rear inflow, bookend vortices, and MCVs that could not be detected by ELDORA.

The NOAA P-3 radar data sets contained the fore and aft radial reflectivity and

radial velocity as well as the lower fuselage C-band reflectivity. Like ELDORA, the data set uncontained raw, unedited data fields complete with the information from the airplane's INS and GPS.

### **Synchronization of radars**

Another goal of BAMEX was to synchronize the flight legs from ELDORA and the NOAA P-3 in order to fuse the datasets together. When the data from ELDORA and the NOAA P-3 are combined there are several benefits. Vertical velocities are much more accurate when two sets of dual-Doppler data are synthesized together to create a quadruple-Doppler (hereafter, referred to as quad-Doppler) analysis (Hildebrand et al. 1996; Jorgensen et al. 1996). Also, the spatial coverage of the analysis increases. Recall that both the ELDORA and the NOAA P-3 use X-band radars. In areas of strong convection, X-band radars are severely affected by attenuation. Therefore, by having two sets of radars sampling the same MCS, the coverage increases, even if attenuation is problematic. An example of attenuation problems and how the use of two sets of radars is beneficial can be seen in Fig. 3.3. ELDORA does an excellent job of sampling the leading edge of the convection as well as the area ahead of the convective line; however, the back edge of the convection and the entire stratiform region is missing due to attenuation. The opposite is true of the NOAA P-3; the stratiform region and the back edge of the most intense convection is sampled, but the leading edge and pre-convective environment ahead of the storm is poorly resolved due to attenuation.

For this study, six ELDORA flight legs were used in the analysis. The first leg commenced at 2230 UTC on 2 June 2003, and the last leg ended at 0017 UTC on 3 June

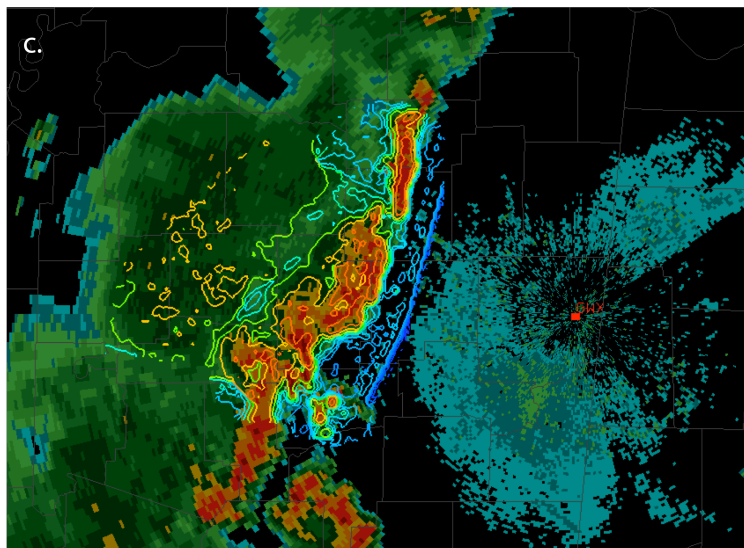
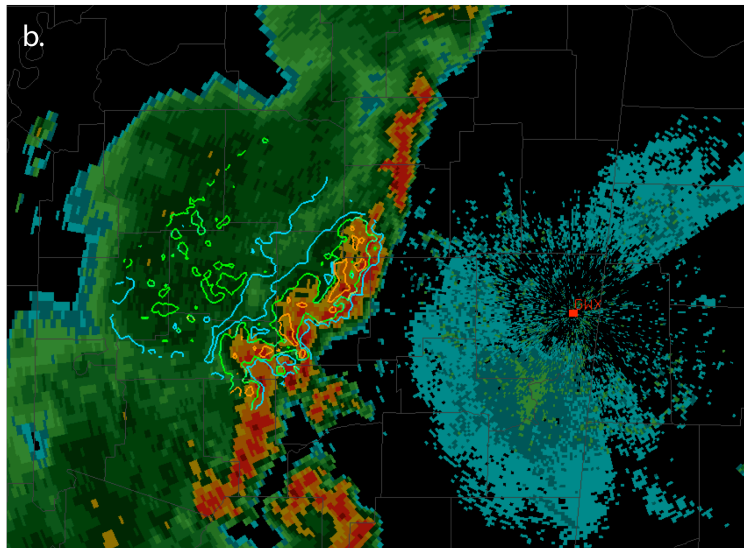
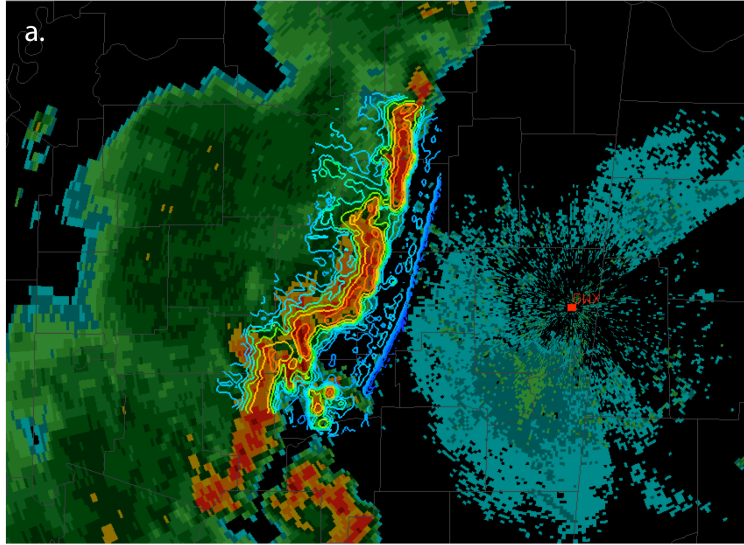


Figure 3.3: Airborne radar data overlaid on NEXRAD level III data from KGWX (Columbus Air Force Base, MS) at 0010 UTC on 3 June 2003. The top image is only the NOAA P-3 radar data (contours) overlaid on the NEXRAD data. The middle image is only ELDORA data (contours) overlaid on NEXRAD data. The bottom image is the maximum reflectivity from both the NOAA P-3 and ELDORA (contours) overlaid on NEXRAD data.

2003, providing just under two hours of nearly complete coverage on the observed MCS (Table 3.3). Two full legs (the fifth and sixth legs) and one partial leg (the second leg) were able to be merged with the NOAA P-3 data. The synchronized data are able to provide a much clearer picture of the entire convective region, not just the convective region or the stratiform region, as is the case for ELDORA and the NOAA P-3, respectively.

Table 3.3: Time (UTC), reference time (UTC), and storm motion for each of the six legs from 2/3 June 2003. The denoted ‘E’ and ‘N’ in the time column denote the times for the ELDORA leg and the NOAA P-3 leg, respectively. The reference time is reference point that was picked to either advect data forward or backward.

	Time of Leg (UTC)	Reference time (UTC)	Storm motion
Leg 1	22:30:00 – 22:48:00	22:40:00	260° at 10.6 m s <sup>-1</sup>
Leg 2	22:50:00 – 23:04:00 (E) 22:45:30 – 23:05:05 (N)	23:00:00	259° at 15.0 m s <sup>-1</sup>
Leg 3	23:06:00 – 23:25:00	23:15:00	260° at 15.0 m s <sup>-1</sup>
Leg 4	23:26:00 – 23:42:30	23:35:00	260° at 15.0 m s <sup>-1</sup>
Leg 5	23:45:00 – 23:59:30 (E) 23:44:30 – 00:01:30 (N)	23:53:00	260° at 15.2 m s <sup>-1</sup>
Leg 6	00:02:45 – 00:17:30 (E) 00:05:15 – 00:14:30 (N)	00:09:00	260° at 15 m s <sup>-1</sup>

### 3.2 Methods of data analysis

Before an accurate three-dimensional reconstruction of the wind field is completed, there are several important steps that need to be completed. The data provided by ELDORA and the NOAA P-3 are raw and unfiltered, meaning it must be put through a set of quality controls before it can be used for research purposes. These correction steps as well as multiple-Doppler theory will be discussed in depth. Fig. 3.4 is provided as a visualization of the data analysis process.

#### 3.2.1 Principles of multiple-Doppler analysis

##### Dual-Doppler theory

The purpose of dual-Doppler analysis is to sample a region from two vantage points (i.e. collect two radial velocity values for the same target, one from the fore and one from the aft beam). The measured velocities,  $V_1$  and  $V_2$ , are expressed by the following equations:

$$V_1 = u \sin \beta_1 \cos \theta_1 + v \cos \beta_1 \cos \theta_1 + (w + V_T) \sin \theta_1 \quad (3.1)$$

$$V_2 = u \sin \beta_2 \cos \theta_2 + v \cos \beta_2 \cos \theta_2 + (w + V_T) \sin \theta_2 \quad (3.2)$$

where  $\beta_{1,2}$  are the azimuthal angles of both radars,  $\theta_{1,2}$  are the elevation angles for both radars,  $V_T$  is the terminal fall speed (calculated using the radar reflectivity), and  $w$  is the vertical motion. Solving for  $u$  and  $v$  yields:

$$u = \frac{1}{\sin(\beta_1 - \beta_2)} \left[ \frac{V_1 \cos \beta_2}{\cos \theta_1} - \frac{V_2 \cos \beta_1}{\cos \theta_2} \right] - (w + V_T) \left[ \frac{\cos \beta_2 \tan \theta_1 - \cos \beta_1 \tan \theta_2}{\sin(\beta_1 - \beta_2)} \right] \quad (3.3)$$

$$v = \frac{1}{\sin(\beta_1 - \beta_2)} \left[ \frac{V_2 \sin \beta_1}{\cos \theta_2} - \frac{V_1 \sin \beta_2}{\cos \theta_1} \right] - (w + V_T) \left[ \frac{\sin \beta_1 \tan \theta_2 - \sin \beta_2 \tan \theta_1}{\sin(\beta_1 - \beta_2)} \right] \quad (3.4)$$

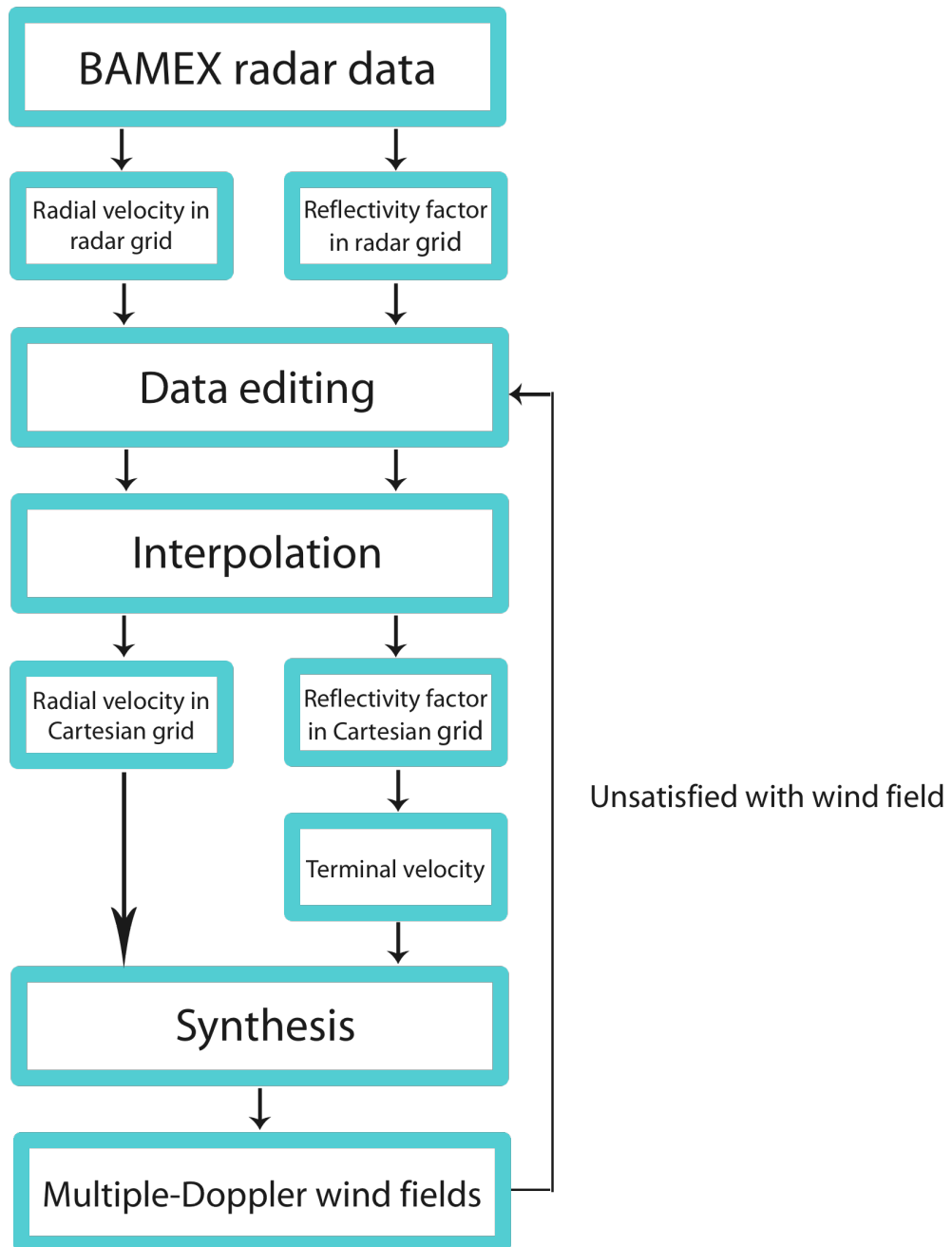


Figure 3.4: Flowchart explaining the data analysis process.

These values are used to create a three-dimensional wind field by vertically integrating the continuity equation:

$$\frac{\partial u}{\partial x} + \frac{\partial v}{\partial y} + \frac{1}{\rho} \frac{\partial(\rho w)}{\partial z} = 0 \quad (3.5)$$

Jorgensen et al. (1996) introduced a technique called the fore-aft scanning technique (FAST), which incorporates an antenna that is alternately scanning forward and aft of the plane normal to the flight track. With FAST, the fore and aft-pointed beams allow one area to be sampled twice in order to obtain two radial velocity measurements use in the calculation of the continuity equation. FAST was useful because until it was implemented, dual-Doppler analysis involved flying two orthogonal flight legs with only one fixed beam and then synthesizing the data from the two, individual legs. Problems with the “L-shaped” pattern included the amount of time taken to complete the two flight legs and having to execute a right-angle turn in the flight pattern (Jorgensen et al. 1996). Many weather phenomena that would be sampled by airborne radar evolve quickly, so the assumption of steady state during the time it would take to execute two flight legs would cause problems in the synthesis. Also, the shape of the weather phenomena is not always conducive to flying orthogonal flight legs (e.g. strong convection that would be ill advised to penetrate). The flight patterns and beam projections for both FAST and the “L-shaped” pattern can be seen in Fig. 3.5. During BAMEX, ELDORA and the NOAA P-3 used a variation of FAST proposed by Jorgensen et al. (1996). Since both radars used a dual-frequency technique, as described in the sections above, the resolution is superior to that of the original FAST technique. Also, since ELDORA has two antennas, the fore and

aft scans can be done simultaneously, aiding in even higher resolution.

While dual-Doppler analysis can provide a three-dimensional picture of the atmosphere, a drawback is that a boundary condition has to be assumed in order to calculate the vertical velocity from the continuity equation. In most analyses, it is assumed that  $w = 0$  at either the top or bottom boundary, depending on whether the integration is being calculated from the top or bottom of the boundary. While this is normally an acceptable assumption, there are situations where it is not. Severe attenuation can taint reflectivity values, which can, in turn, cause problems in calculating the terminal velocity. Assuming a boundary condition can be difficult due to the radar constraints of being able to scan at steep enough elevation angles in order to capture the top of the convection. Also, assuming a boundary condition can cause problems in the calculated vertical motion field if the convection is changing rapidly.

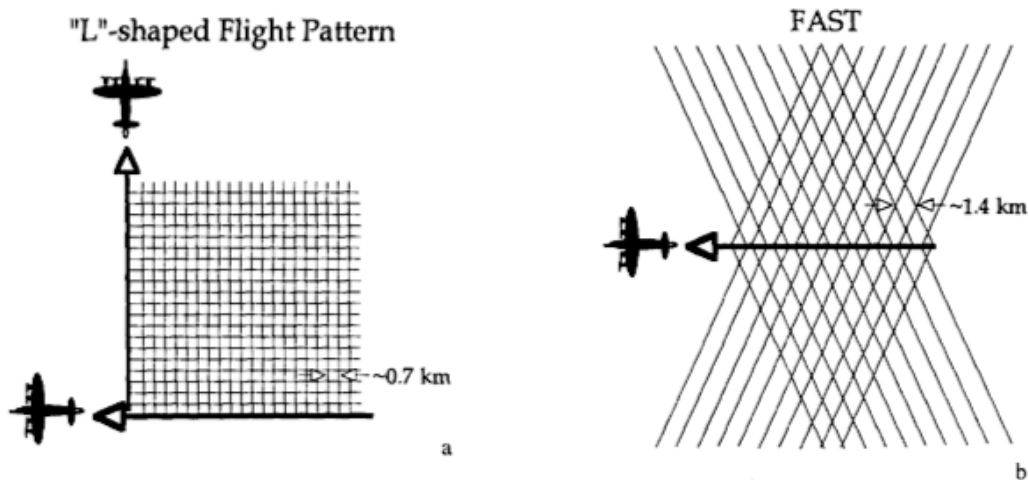


Figure 3.5: Horizontal projection of the individual beams for a) two quasi-orthogonal flight patterns ("L"-shaped flight pattern); b) fore/aft scanning technique for alternating forward and aft beams. Taken from Jorgensen et al. 1996).

## Quad-Doppler theory

The three-dimensional wind field can be solved for by using dual-Doppler data; however, if a quad-Doppler solution is available, it can provide a much more accurate reconstruction of the wind field. The quad-Doppler theory is based on taking four radial velocity measurements for a single target. When calculating the wind field, there are two possible solutions to choose: an over-determined dual-equation solution or an over-determined triple-equation solution. Often, if analysis is confined to the lower-levels, the dual-equation solution is used. This is done because at relatively low levels, where the elevation angles are small, the sampling plane is approximately horizontal. This would allow the dual-equation to provide a relatively accurate depiction of the horizontal flow field. However, at higher levels, where the elevation angle increases, the three-equation solution is often used. An over-determined solution to the triple-equation solution is used at the echo top in order to derive the vertical particle motion. This is a far better estimate than assuming  $w = 0 \text{ m s}^{-1}$ , which is done in dual-Doppler analysis. This is especially effective in areas of strong convection. In this study, the over-determined triple-equation solution was used and can be expressed as:

$$\begin{bmatrix} u \\ v \\ w \end{bmatrix} = A^{-1} \bar{a} \quad (3.6)$$

where

$$A = \begin{bmatrix} \sum_{i=1}^n l_{x_i}^2 & \sum_{i=1}^n l_{x_i} l_{y_i} & \sum_{i=1}^n l_{x_i} l_{z_i} \\ \sum_{i=1}^n l_{y_i} l_{x_i} & \sum_{i=1}^n l_{y_i}^2 & \sum_{i=1}^n l_{y_i} l_{z_i} \\ \sum_{i=1}^n l_{z_i} l_{x_i} & \sum_{i=1}^n l_{z_i} l_{y_i} & \sum_{i=1}^n l_{z_i}^2 \end{bmatrix} \quad (3.7)$$

and

$$\bar{a} = \begin{bmatrix} \sum_{i=1}^n l_{x_i} V_{r_i} \\ \sum_{i=1}^n l_{y_i} V_{r_i} \\ \sum_{i=1}^n l_{z_i} V_{r_i} \end{bmatrix} \quad (3.8)$$

and

$$\begin{aligned} l_{x_i} &= \sin \theta_i \cos \phi_i \\ l_{y_i} &= \sin \phi_i \\ l_{z_i} &= \cos \theta_i \cos \phi_i \end{aligned} \quad (3.9)$$

where  $l_{x_i}$ ,  $l_{y_i}$ ,  $l_{z_i}$  are direction cosines from the aircraft to the target.

It should be noted that the quad-Doppler solution is used where the sampled areas from both sets radars overlap, and a dual-Doppler solution is used where there is no overlap of radar coverage. During the 2-3 June 2003 case, this area of overlap from the two sets of dual-Doppler radars consisted of the most intense convective region and the region directly behind (i.e. to the west of) the convective line. In areas that were only sampled by ELDORA or the NOAA P-3, such as in front of the convective region and the stratiform region, respectively, a dual-Doppler solution was used to calculate the wind field.

### 3.2.2 Data editing

There are several steps that need to be taken in order to perform an accurate reconstruction of the three-dimensional wind field. Through the use of SOLO II (Oye et

al. 1995), a software program, the radar data can be edited to ensure a 'clean' and accurate data set.

The first step of editing radar data is correcting for the motion of the aircraft. Using radars mounted on an airborne platform adds sources of error that do not exist in ground-based radars. The radial velocities by the airborne radars contain both a meteorological component and a platform motion component (Bosart et al. 2002). While a ground based radar only has three degrees of freedom (azimuth angle, elevation angle, and range delay), airborne radar has nine degrees of freedom (Bosart et al. 2002). Of the nine, five are associated with the INS and/or the GPS, and they include ground speed, drift angle, pitch angle, roll angle, and aircraft vertical velocity. Three are attributed to the radar system. They are tilt angle, rotation angle, and range delay. The final source of error is the aircraft altitude. Revisiting Fig. 3.2 provides a visual in understanding the different errors. To ensure that these errors are minimized in the analysis, the navigational errors are removed by importing and applying correction factors into the SOLO II editing software. The correction factors were generated using techniques from Testud et al. (1995) and Bosart et al. (2002). The individualized correction factors for each leg and for each aircraft for the 2-3 June 2003 mission are in the Appendix. Without applying these corrections, Testud et al. (1995) and Bosart et al. (2002) both show that there are significant differences between the corrected radial velocities and the raw radial velocities, which can lead to inaccurate three-dimensional wind fields. The above-mentioned step also removes the motion of aircraft from the velocity data, resulting in a ground-relative velocity.

The next series of steps includes directly removing and correcting the ‘bad’ data from the raw, unedited fields. This includes removing the ground echoes, noisy data, and side lobes from both the reflectivity and velocity data. Next, if there are any radial velocity folds in the data, the data are unfolded, using the Barga and Brown (1980) technique. Recall that the unambiguous velocity of ELDORA is  $77.2 \text{ ms}^{-1}$ , and the unambiguous velocity of the NOAA P-3 is  $51.5 \text{ ms}^{-1}$  during BAMEX. These are relatively high unambiguous velocities; rarely did the NOAA P-3 and ELDORA data need to be unfolded for the 2-3 June 2003 mission. These steps are done using automatic commands in the Solo II software, which is efficient at removing a majority of the poor data; however, there are still areas that cannot be edited in the automatic edits.

The final step in completing the process is manually editing the data. It is the responsibility of the human data editor to manually remove the remaining bad areas of data that were not removed with automatic edits. The manual edits must be done cautiously, in order to appropriately remove the bad data while preserving the good data. Admittedly, this is a subjective process, but when done properly, it can ensure an excellent quality synthesis.

### *3.2.3 Converting to Cartesian grid*

For this study, a program called Reorder (Oye and Case 1995) was used for the interpolation from radar space to Cartesian space. Reorder allows the user to input the horizontal and vertical grid spacing, weighting function, and advection.

For the ELDORA interpolation, the horizontal and vertical grid-spacing were 400 and 600 m, respectively. Revisiting the ELDORA scanning modes for BAMEX in Table

1, the along-track beam spacing and sweep-angle beam were  $\sim 300$  m and  $1.4^\circ$ , respectively. The effective vertical spacing was calculated using simple trigonometry combined with the average distance from the aircraft to the convection during the 2-3 June 2003 event. Since the NOAA P-3 has coarser resolution in the horizontal than ELDORA, the flight legs where the ELDORA and NOAA P-3 data were merged for a quad-Doppler solution must use the coarser grid-spacing of the NOAA P-3. For the merged syntheses, the horizontal and vertical grid-spacing is 1200 and 600 m, respectively. These values were calculated similarly to ELDORA, with the NOAA P-3 having an along-track beam spacing and sweep angle of  $\sim 1200$  m and  $1.4^\circ$ , respectively (Table 3.2).

In order to obtain vertical velocities in later steps of the data analysis process, upper and lower boundaries had to be established and input into Reorder. The upper and lower physical boundaries of a convective system are typically from the storm top to the ground, and this is where the vertical velocities become zero. These physical boundaries are not always consistent with boundaries in the multiple-Doppler wind field, due to constraints of the radar systems. For both the ELDORA and NOAA P-3 analyses for the 2-3 June 2003, the lowest computational boundary was 0.45 km, and the upper computational boundary was 11.25 km.

In order to translate the radar data from radar space to a Cartesian grid, a filter or interpolation scheme had to be implemented. This study applied the Cressman filter (Cressman 1959). The Cressman filter weights points, accordingly:

$$W = \frac{(R^2 - r^2)}{(R^2 + r^2)} \quad (3.10)$$

where  $W$  is the weight applied to a particular point,  $R$  is the radius of influence,  $r$  is the distance from the observational point to the grid point. With this relationship, the closer the observational point is to the grid point, the more weight it is given in the interpolation.

For the legs with only ELDORA data, a radius of influence of 400 and 600 m in the horizontal and vertical, respectively, was used in both the reflectivity and wind fields. In the NOAA P-3 and merged data sets, a radius of influence of 1200 and 600 m in the horizontal and vertical, respectively, was used in both the reflectivity and wind fields. Larger radii of influence were also tested to test sensitivity of the radii used. This did not alter the results, ensuring the radii of influence used in this study to be sufficient.

Reorder also has an option to input the advection of the convection. For each leg, the advection of the storm was calculated using NEXRAD level III data from KGWX (Columbus Air Force Base, MS) by selecting certain points in the convection and plotting them from radar scan to scan. Also, a time close to the middle of each leg was chosen as the reference point to either advect data backward or forward in order to adjust for time-space evolution of the convection. If data were not advected there would be problems in both the horizontal and vertical planes that would result in miscalculations of the two- and three-dimensional flow fields. It is also important to note that each leg is over 15 minutes in time, and the convective system can be evolving during a leg and from leg to leg. It is assumed that during the individual legs there is good time continuity and steady state is assumed, and from one leg to another all features are able to be resolved. The details used in Reorder for the six legs from 2-3 June 2003 are listed in Table 3.3.

### 3.2.4 *Synthesizing data*

The Custom Editing and Display of Reduced Information in Cartesian Space (CEDRIC; Mohr et al. 1986) was used to synthesize the radar data. After the radar data were edited in SOLO II and interpolated from radar space to Cartesian space in Reorder, the data were synthesized in CEDRIC. In CEDRIC, the user can specify whether to use the dual- or triple-Doppler solution, the  $Z-V_T$  relationship, integration scheme, boundary conditions, etc. for the synthesis. It is in CEDRIC where the data from the multiple-Doppler radars is combined to derive a wind field. As mentioned in a previous section, to properly reconstruct the three-dimensional wind field, there are four quantities that need to be measured or calculated: the components of velocity ( $u$ ,  $v$ , and  $w$ ) and the terminal fall speed of a target ( $V_T$ ). The vertical motion is derived by integrating the mass continuity equation, and there are three different methods of integration: downward, using the upper boundary conditions, upward, using the lower boundary conditions, and a variational scheme. The variational approach requires the integration of the anelastic continuity equation to meet both lower and upper boundary conditions of  $w = 0 \text{ ms}^{-1}$  (O'Brien 1970). It has been found that integrating upward often causes an overestimate of the winds in the upper-levels. If there are errors in the derived wind field in the lower-levels, they will be amplified due to the larger magnitude of the density weighting in the lower-levels. For this reason, the downward integration or variational scheme is most often used in syntheses. This study used the variational scheme.

A Leise filter (Leise 1982) was applied in order to smooth the data. The Leise filter is a low-pass filter that incorporates a linear method and is able to work to the boundaries of a data set (Leise 1982). The purpose of filtering is to mitigate noise, isolate

a prominent signal, and assist in pattern recognition. To identify the flow features while minimizing noise or having excessively smoothed features, a four-step filter was applied to the ELDORA-only syntheses, and a three-step filter was applied to the combined ELDORA and NOAA P-3 syntheses. The four-step filtering of the ELDORA data effectively removed wavelengths less than 6.4 km in the horizontal, and the three-step filtering of the combined datasets effectively removed wavelengths of 9.6 km in the horizontal. It should be noted that due to the attenuation issues mentioned above, the reflectivity field was also filtered using a three-step Leise filter when the ELDORA and NOAA P-3 data were merged; this alleviated attenuation issues in the convective region.

CEDRIC also has the ability to calculate other meteorological fields after it calculates the components of the wind. This study utilized CEDRIC to compute vertical motion, divergence, vertical vorticity, horizontal vorticity, components of the vertical vorticity time tendency equations as well as a variety of other fields. The results of these syntheses will be discussed in Chapter 5 and 6.

## Chapter 4

### ENVIRONMENTAL CONDITIONS

#### **4.1 Synoptic and mesoscale environment**

The main focus of this study is to form a complete, detailed analysis of the 2-3 June 2003 MCS. While airborne radar is able to provide high-resolution data of the 2-3 June 2003 MCS, it is equally important to understand the larger-scale environment in which the MCS formed and matured. A brief overview of the synoptic and mesoscale environments will be summarized in this chapter.

On 2 June 2003 at 1200 UTC, there was a surface low located in north central Oklahoma (Fig. 4.1a). The low-pressure system is associated with a cold front oriented from NE to SW extending into Texas with a warm front stretching from Oklahoma through central Arkansas and Mississippi. Figures 4.1b-d show the eastward propagation of the system with time. While the cold front advances eastward, the warm front stalls over Arkansas and Mississippi, causing the system to occlude. Above the surface, there is south-southwesterly flow at 850 hPa advecting warm, moist air into the Gulf Coast region (Fig. 4.2a). At 500 hPa, there is a broad shortwave trough propagating through Oklahoma associated moderately strong ( $25\text{-}30\text{ m s}^{-1}$ ) southwesterly flow (Fig. 4.2b).

The upper-level jet stream is situated over the Northern and Central Plains, but there is relatively strong diffluence over the southern Gulf Coast region (Fig. 4.2c). Figures 4.3 displays NOWRAD composites of the BAMEX region for the morning (1400 UTC) and afternoon (1800 UTC) of 2 June 2003. At both times, there is widespread precipitation over Missouri, Iowa, and Illinois associated with a remnant mesoscale convective vortex (MCV) from the previous night's convection. There is also an MCS that traverses over Arkansas and southern Missouri in association with the low-pressure system. Ahead of the MCS, near eastern Tennessee and into northern Mississippi, an area of broad rain showers initiates. This area of convection was just north of where the 2-3 June 2003 MCS forms later in the day. These rain showers propagate eastward throughout the morning, leaving behind moist and cloudy conditions in the region; however, this cloud cover eroded in conjunction with the daytime heating, allowing surface temperatures to approach 25°C with dewpoints near 20°C in northern Mississippi by late afternoon (4.2b,c).

As the MCS in Arkansas approached the Mississippi border (~2200 UTC), it became more organized and entered an area where it would be sampled by BAMEX. Figure 4.4 shows the radar history of the squall line as it passes through Mississippi as well as the locations of the ground-based measurement platforms, including: mobile rawinsonde launches, the NOAA-operated wind profiler in Okolona, MS, and NWS-operated WSR-88Ds in the region. Figures 4.4a,b show the weak convection ahead of the MCS at the times closest to two of the mobile rawinsonde launches. While the convection is not very organized, it was enough to alter the preexisting environment where the 2-3 June 2003 MCS formed and moved over later in the afternoon.



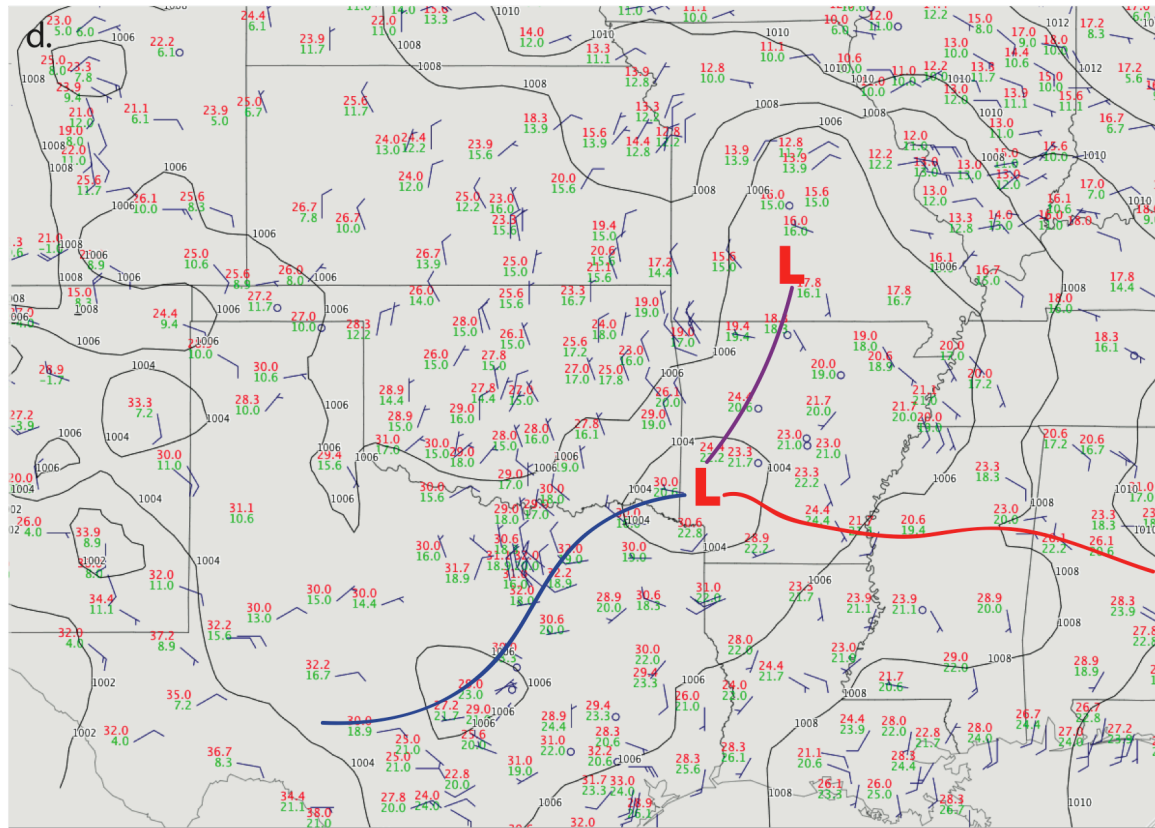
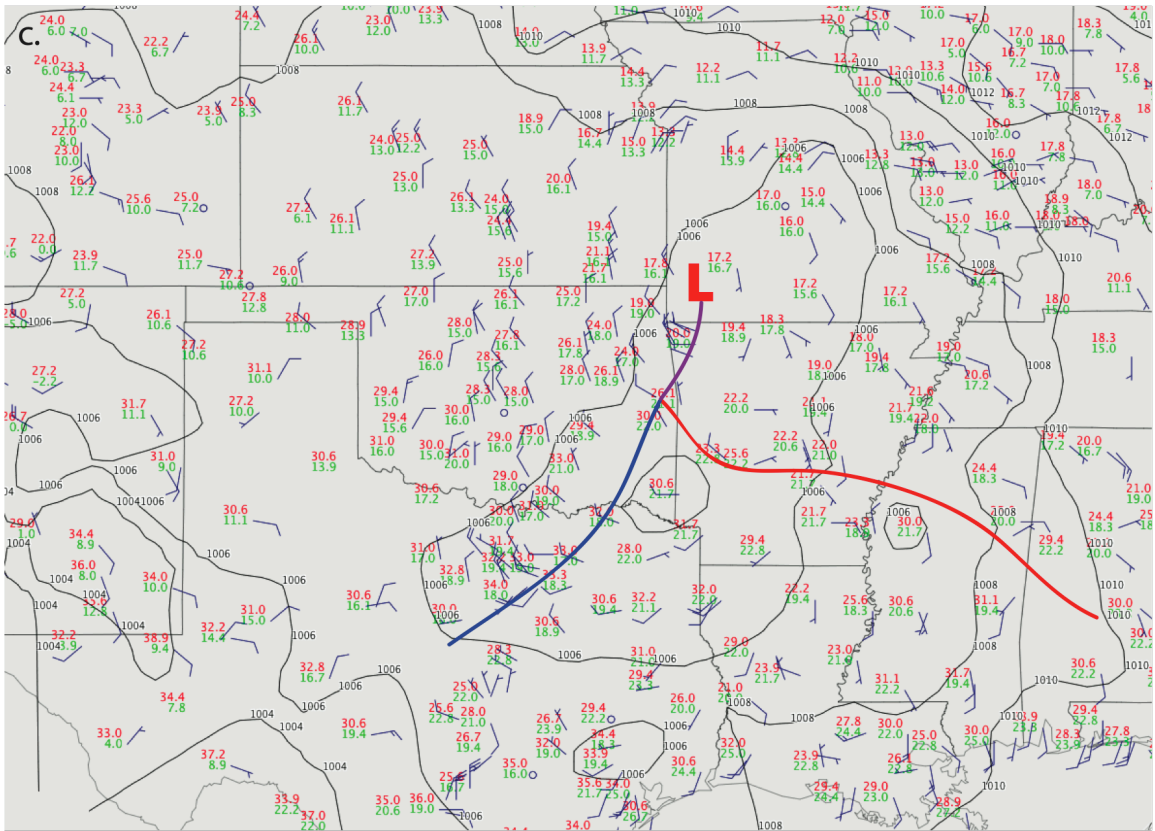
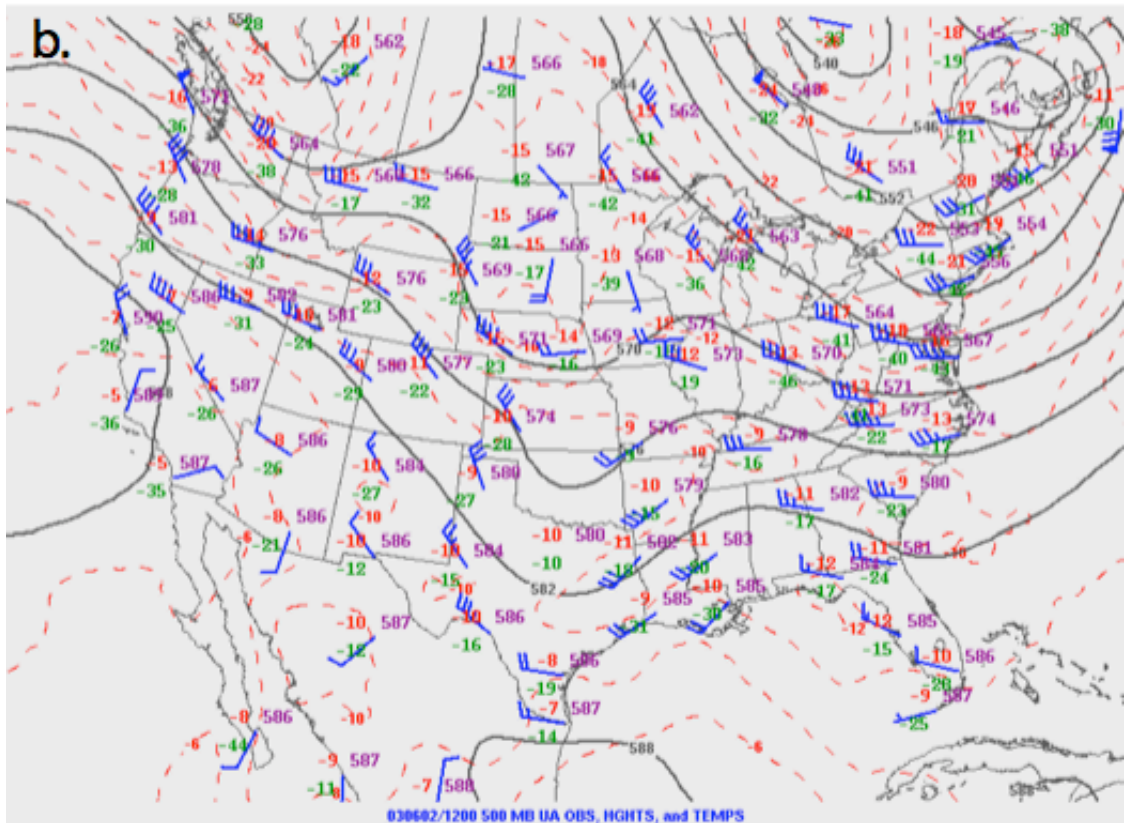
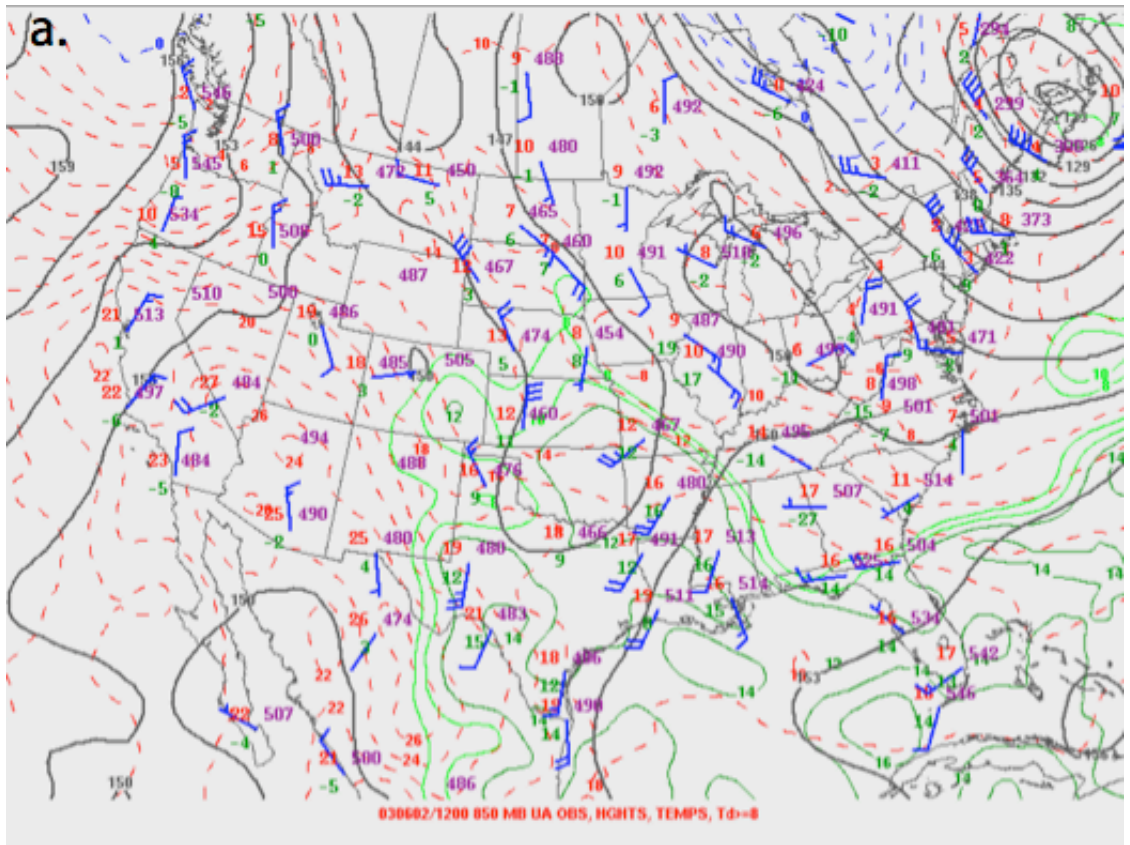


Figure 4.1: Surface maps from 2-3 June 2003 for the following times: (a.) 1200 UTC, (b.) 1800 UTC, (c.) 2200 UTC, and (d.) 0000 UTC. Temperature ( $^{\circ}\text{C}$ ) is displayed in red, dewpoint is displayed in green, and pressure is displayed by black lines, contoured every 2 hPa. Blue, red, and purple lines denote the location of the cold fronts, warm fronts, and occluded fronts, respectively.

Figures 4.4c-f show the evolution of the 2-3 June 2003 MCS from when the airborne radars began sampling the squall line until the final flight leg. The radar images of the MCS first display a relatively linear squall line with some small undulations within the line (Figs. 4.4c-e). In the radar image concurrent with the beginning of the final flight leg (Fig. 4.4f), there is a segment of the convective line that “bows” outward. While the appearance on radar does not resemble a classic bow echo, there are obvious signs of the line accelerating forward. Also observed in Figs. 4.4c-f is the stratiform region associated with the 2-3 June 2003 MCS. Overall, there is trailing stratiform in Figs. 4.4c-f; however, the trailing stratiform region in Figs. 4.4d,e has lower reflectivities directly behind the main portion of the convective line. Another important observation is the presence of stratiform parallel to the convective region in Figs. 4.4c-f, making this MCS a hybrid trailing/parallel stratiform mode. Finally, by observing the radar sequence of the MCS as well as the surface maps, the portion of the MCS being reviewed for this study is just to the north of the warm front associated with the low-pressure system.

Mobile soundings at 1735 and 1903 UTC (Figs. 4.5 and 4.6; both soundings from the same location given by the southernmost black stars in Fig. 4.4) show ample instability to support deep convection in northern Mississippi; however, the wind profiles exhibit weak shear. The soundings show moderate CAPE ranging from 1626 – 2320  $\text{J kg}^{-1}$ . The two soundings have similar shear profiles; the low-level shear (surface to 2.5



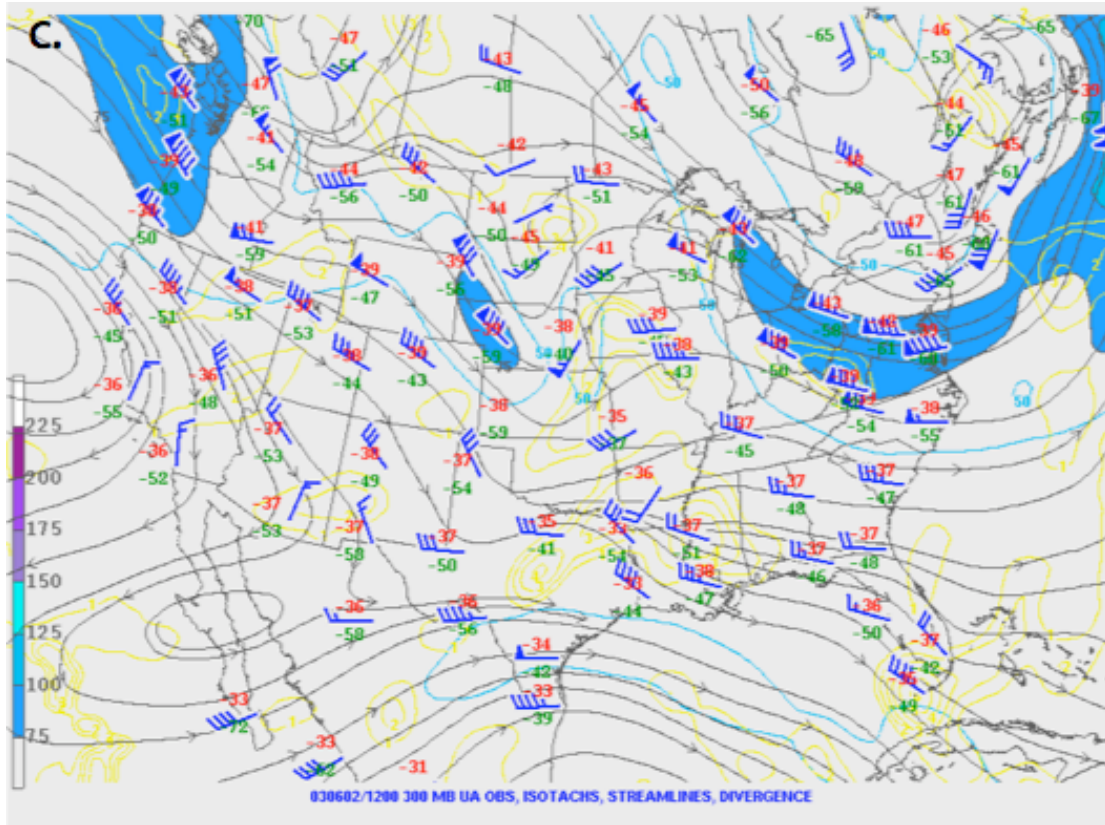


Figure 4.2: Upper-air maps at 1200 UTC on 2 June 2003: (a) 850 hPa; black lines are height (dm), red dashed lines are temperature ( $^{\circ}\text{C}$ ), green lines are mixing ratio ( $\text{g kg}^{-1}$ ), (b) 500 hPa; black lines are height (dm), (c) 300 hPa; black lines are streamlines, blue lines are isotachs (knots), and the yellow lines are divergence ( $10^{-3} \text{ s}^{-1}$ ).

km) is only  $5 \text{ m s}^{-1}$ , and the shear from the surface to 5.0 km is  $\sim 15 \text{ m s}^{-1}$ . If one compares these values to values used in simulations by Weisman and Davis (1998), the environmental shear for 2-3 June 2003 MCS would be considered weak. That study classifies shear as: weak ( $10 \text{ m s}^{-1}$  from surface to 2.5 km), moderate ( $20 \text{ m s}^{-1}$  from surface to 2.5 km), or strong and deep ( $30 \text{ m s}^{-1}$  from surface to 5.0 km). Evans and Doswell (2001) used observational data to investigate the environments in which derechoes occurred. They discovered that while most derechoes tend to form in high CAPE and shear environments, they can occur over a wide variety of wind shears,

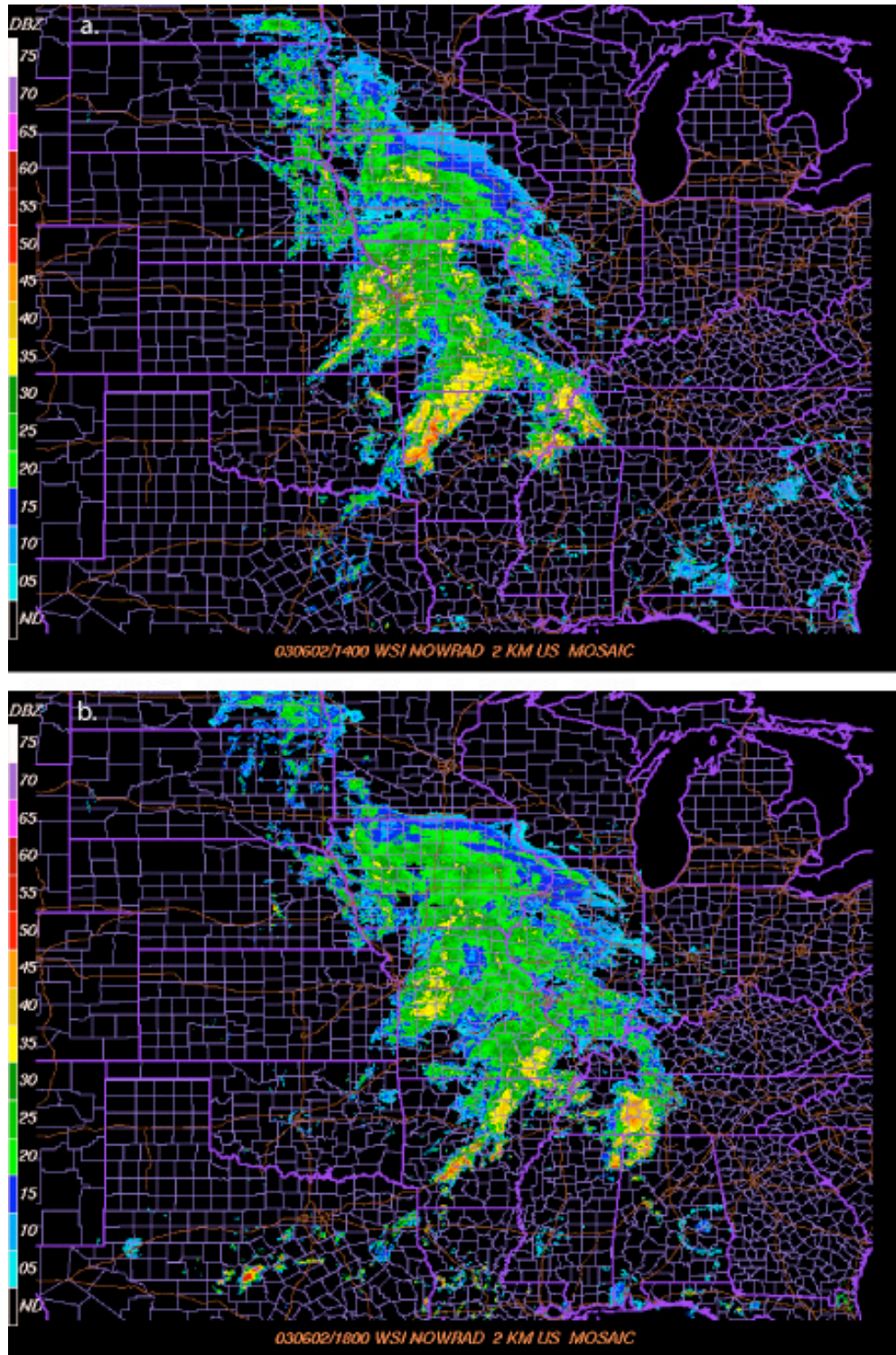


Figure 4.3: NOWRAD composites over the BAMEX region for 2 June 2003 at (a.) 1400 UTC and (b.) 1800 UTC.

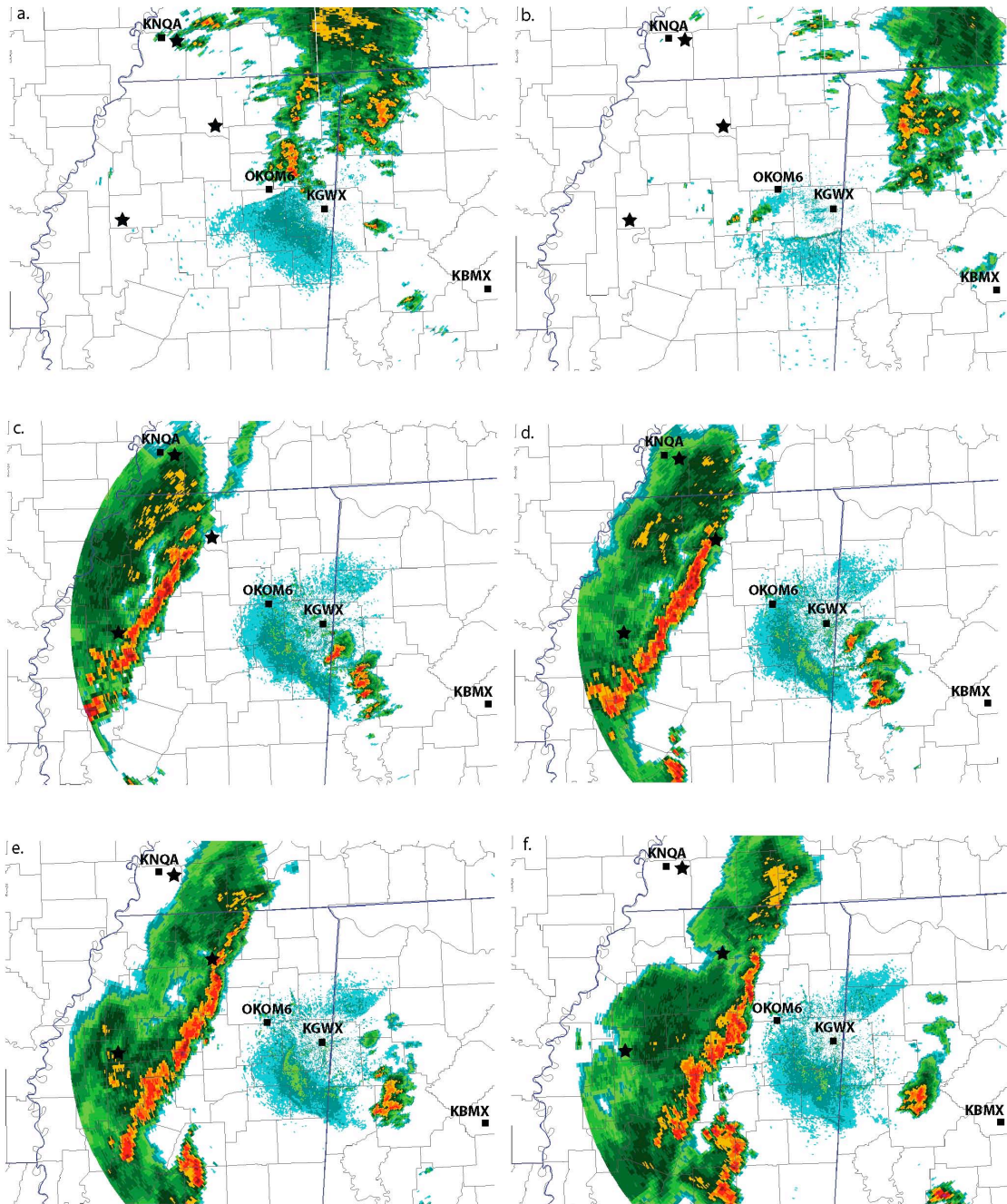


Figure 4.4: Sequence of composite radar images of squall line as it passed over Mississippi at (a.) 1730 UTC, closest time to the 1735 UTC mobile rawinsonde launch, taken at the southernmost black star, (b.) 1903 UTC, the exact time of the 1903 UTC mobile rawinsonde launch, taken at the southernmost black star, (c.) 2235 UTC, near the commencement of the first flight leg flown by ELDORA, (d.) 2300 UTC, near the end of the second flight leg (e.) 2330 UTC, near the beginning of the fourth flight leg, and (f.) 2359 UTC, between the fifth the sixth flight leg. The NWS radars (KNQA, KGWX and KBMX) and the NOAA wind profiler (OKOM6) are denoted by black squares. The black stars denote the locations of the mobile soundings.

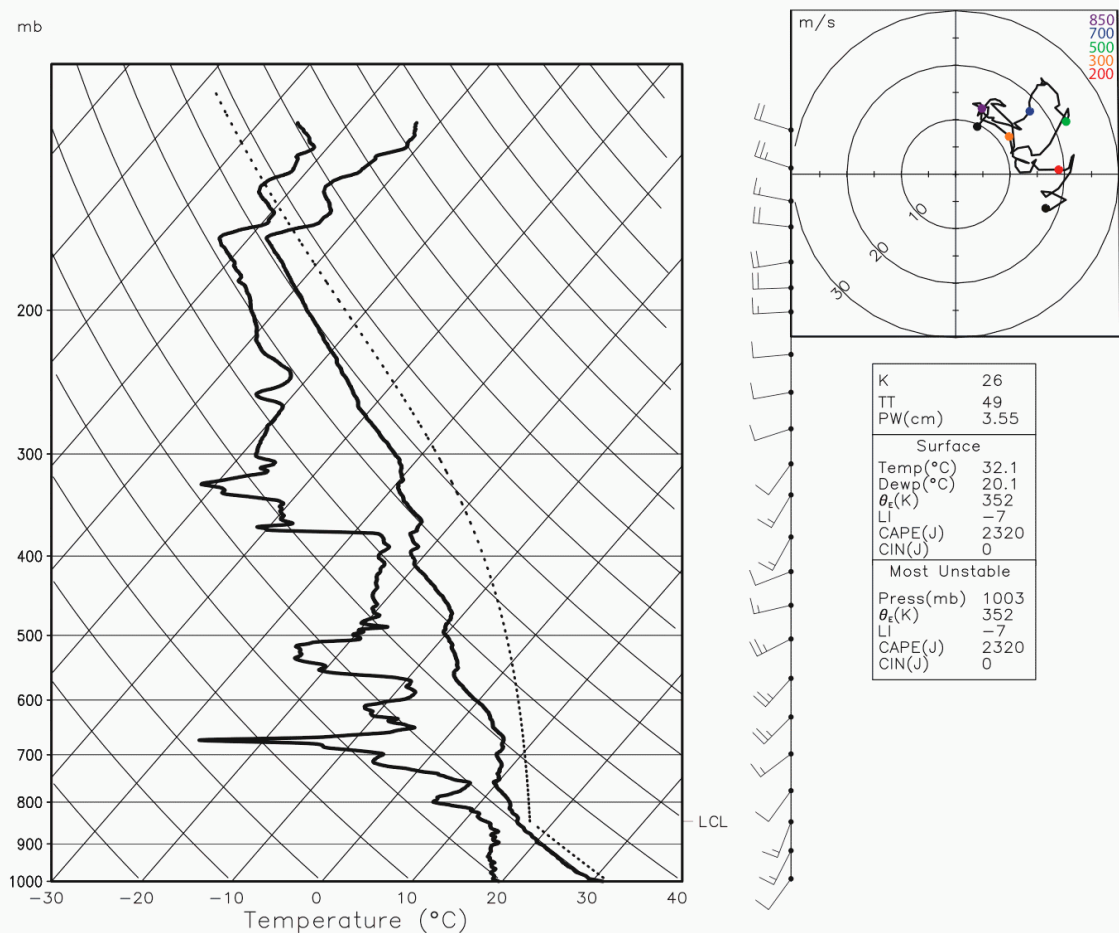


Figure 4.5: Mobile sounding from 90.48 W, 33.96 N (the southernmost mobile sounding location as seen in Fig. 4.1) at 1735 UTC.

including shears classified as weak and moderate by Weisman and Davis (1998) as well as the environment of the 2-3 June 2003 MCS. While bowed convection typically forms under moderately-to-highly sheared environments, it is possible to develop under weakly sheared conditions as well.

In addition, the pre- and post-convective wind profiles can be viewed from the Okolona, MS wind profiler (Fig. 4.7a). Overall, the pre-convective wind profiles show mostly unidirectional shear and are similar to the mobile soundings taken at 1735 and 1903 UTC, with the exception of the southeasterly flow near the surface. Hodographs from the Okolona, MS wind profiler were constructed for 2100 – 0000 UTC, which

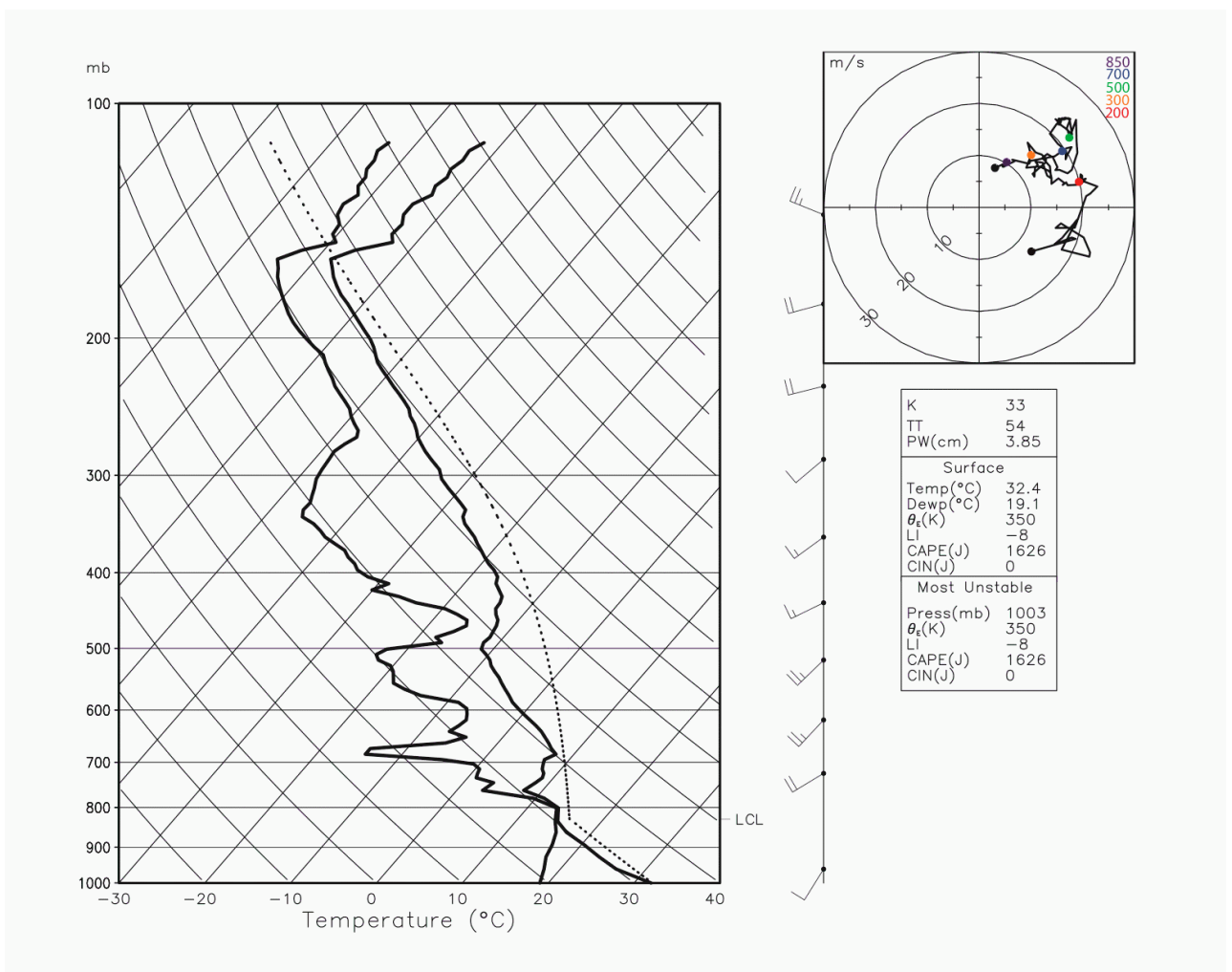


Figure 4.6: Mobile sounding from 90.48 W, 33.96 N (the southernmost mobile sounding location as seen in Fig. 4.1) at 1903 UTC.

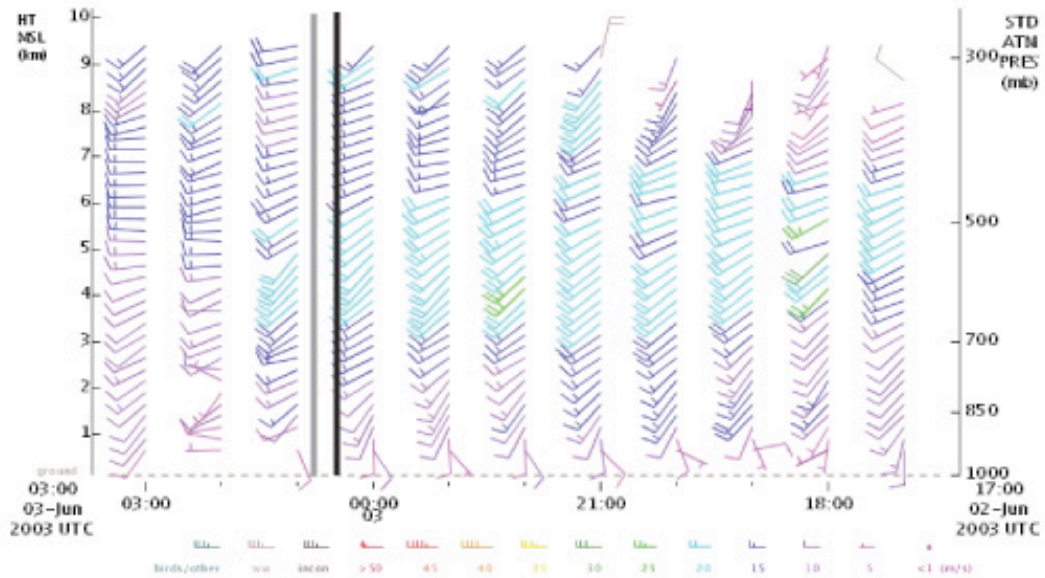
includes the organizational stages until the convection passes directly over the wind profiler (Fig. 4.8). The shear vector from the surface to 3.5 km is displayed to show there is a significant component of line-parallel shear.

The wind profiler also provided signal power (dB; measure of the backscattered power) and radial velocity ( $\text{m s}^{-1}$ ; positive when towards the ground and negative when away from the ground) from the Okolona, MS profiler are also displayed (Figs. 4.7b,c, respectively). The black and grey lines denote the passage of the convective line and stratiform regions, respectively, over the profiler. There is also a well defined transition

a.



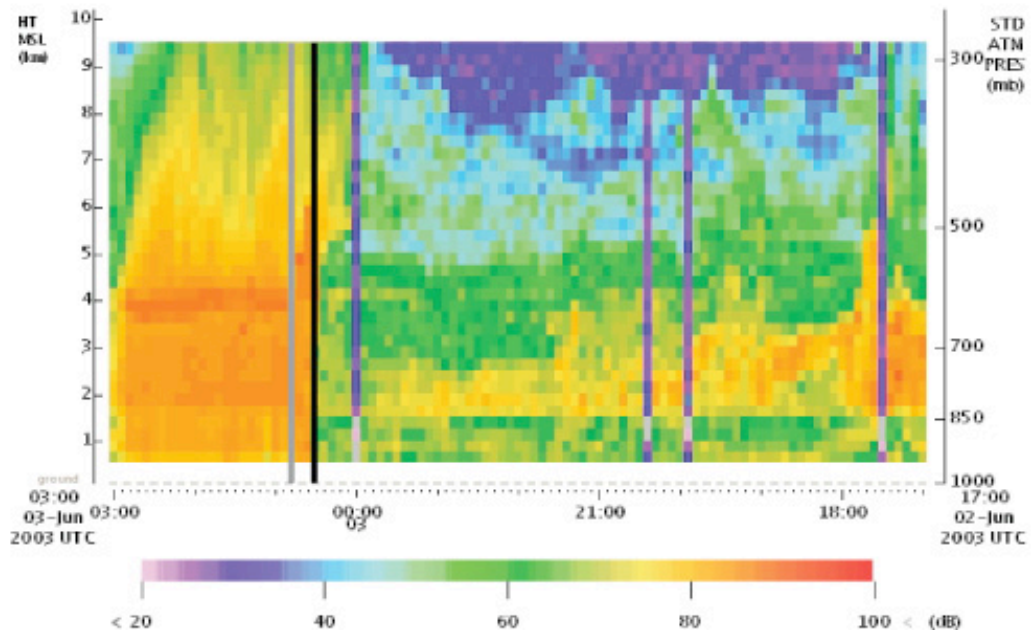
**OKOLONA, MS US Lat:34.08 Lon:-88.86 Elev:125m**  
WindSpeedDirection| Mode:310m | Res:60min | QC:good+INC+CONT+BIRO  
NOAA PROFILER NETWORK



b.



**OKOLONA, MS US Lat:34.08 Lon:-88.86 Elev:125m**  
SpectralPeakPower| Mode:310m | Beam:V | Res:6min | QC:good+INC+CONT+BIRO  
NOAA PROFILER NETWORK



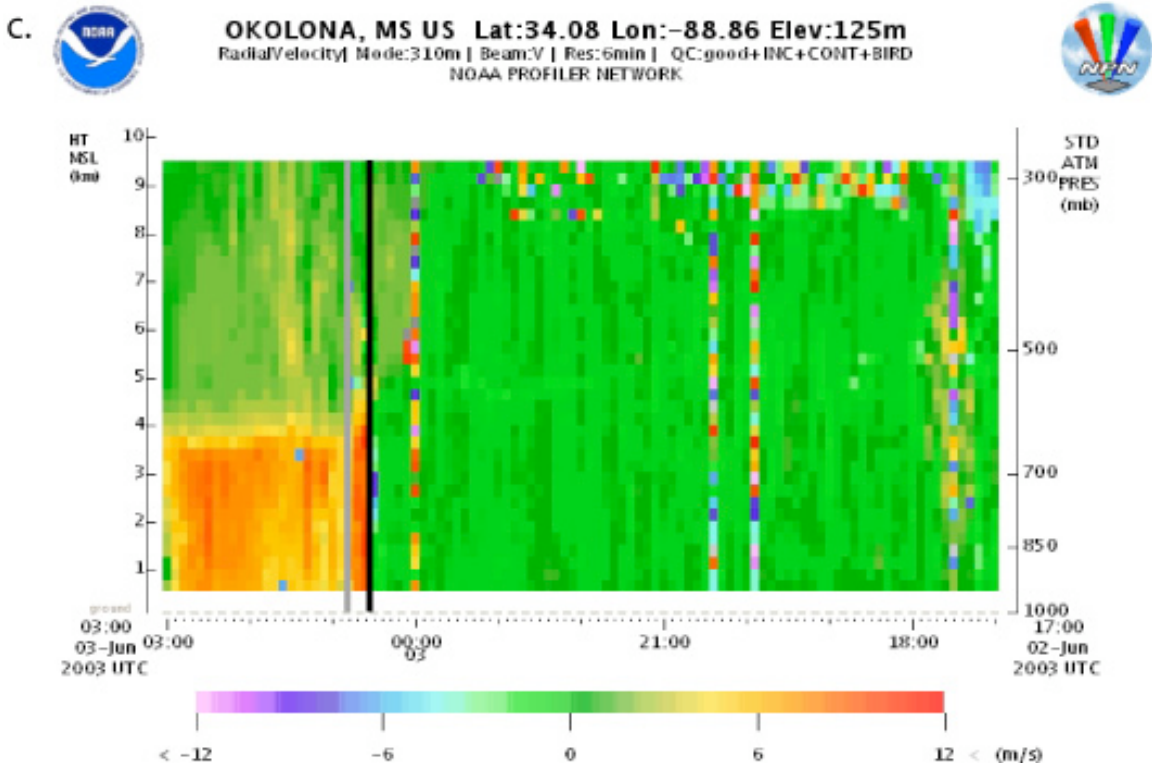


Figure 4.7: Profiler data from Okolona, MS from 1700 (2 June) – 0300 (3 June) UTC. (a.) wind profile ( $\text{m s}^{-1}$ ), (b.) signal power (dB), and (c.) radial velocity ( $\text{m s}^{-1}$ ). The black and grey lines denote the passage of the convective and stratiform regions, respectively, over the profiler.

zone between the convective and stratiform regions as well as a bright band near 4 km.

The signal power and radial velocity clearly capture the deep convective region, which is followed by a less intense trailing stratiform region. This agrees with the radar images in Figs. 4.3c-f.

## 4.2 Summary

On the morning of 2 June 2003, there was a surface low in Oklahoma that moved eastward into southern Missouri as the day progressed. In addition to an MCS that was associated with the frontal system, there was also widespread precipitation ahead of the

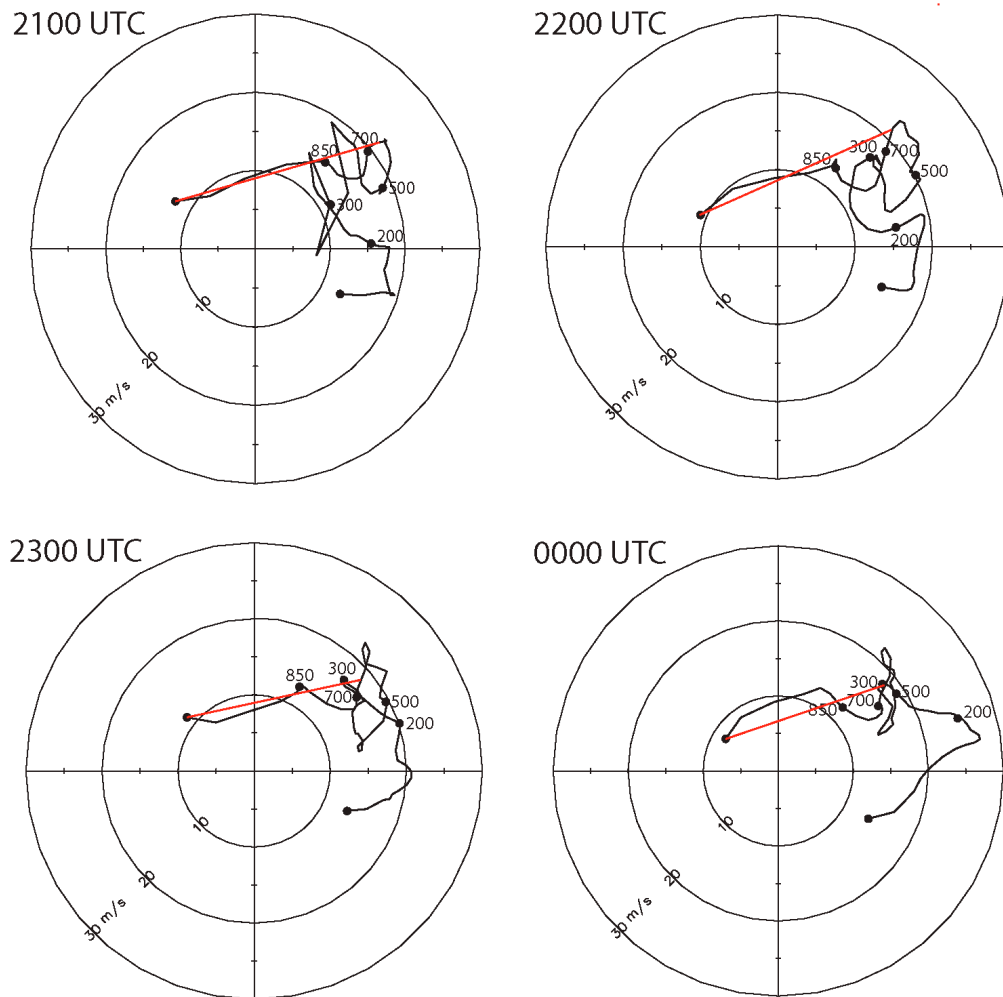


Figure 4.8: Hodographs from the Okolona, MS wind profiler for the time period from 2100 (2 June) – 0000 (3 June) UTC. Pressure levels (850, 700, 500, 300, and 200 hPa) are labeled. The red line denotes the 0 – 3.5 km shear vector.

MCS in eastern Tennessee and northern Mississippi. These rain showers propagated eastward throughout the late morning, leaving cloudy skies and a moist environment in the area where the 2-3 June MCS would eventually form and move over. Daytime heating allowed for temperatures to approach 25°C with dewpoints near 20°C.

Atmospheric soundings revealed ample instability for strong convection, but the vertical wind profiles did not exhibit strong vertical wind shear. The wind profiler in Okolona, MS displayed a similar environment. While there was only weak-to-moderate

vertical wind shear, there was a component of line-parallel shear, which will be significant when discussing the vertical vorticity patterns in the following chapters.

## Chapter 5

### OVERALL STRUCTURE OF THE SQUALL LINE

#### 5.1 Overall squall evolution

As discussed in the previous chapter, there was convection associated with the low-pressure system that was present throughout the day; however, it became more intense around 2030 UTC near the Arkansas/Mississippi border. It started to organize into a line around 2200 UTC, and conveniently, ELDORA and the NOAA P-3 commenced flight legs at 2230 UTC (2 June) and flew until 0020 UTC (3 June). ELDORA flew six, ~120 km flight legs during this time period (Fig. 5.1). Flight legs were conducted on a southwest/northeast axis parallel to the low-to-mid-level shear. The NOAA P-3 was able to coordinate with ELDORA to fly three, synchronized flight legs, allowing for quad-Doppler analysis during the 2<sup>nd</sup>, 5<sup>th</sup>, and 6<sup>th</sup> flight legs.

While the airborne radars were able to sample a good portion of the MCS, due to time and space constraints, the radars could not retain data from the entire MCS. Figure 5.2 provides the NOWRAD composite for BAMEX region in order to display the entire MCS, which, overall, retains reflectivity features similar to the trailing stratiform type as described by Parker and Johnson (2000). The MCS, itself, is the southern extension of an extensive area of precipitation centered over Illinois. The main focus of this study is

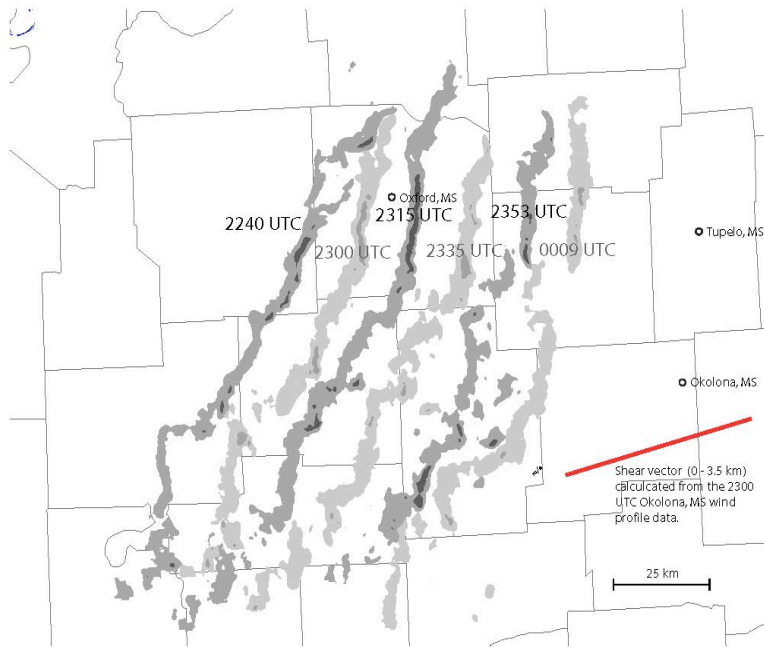
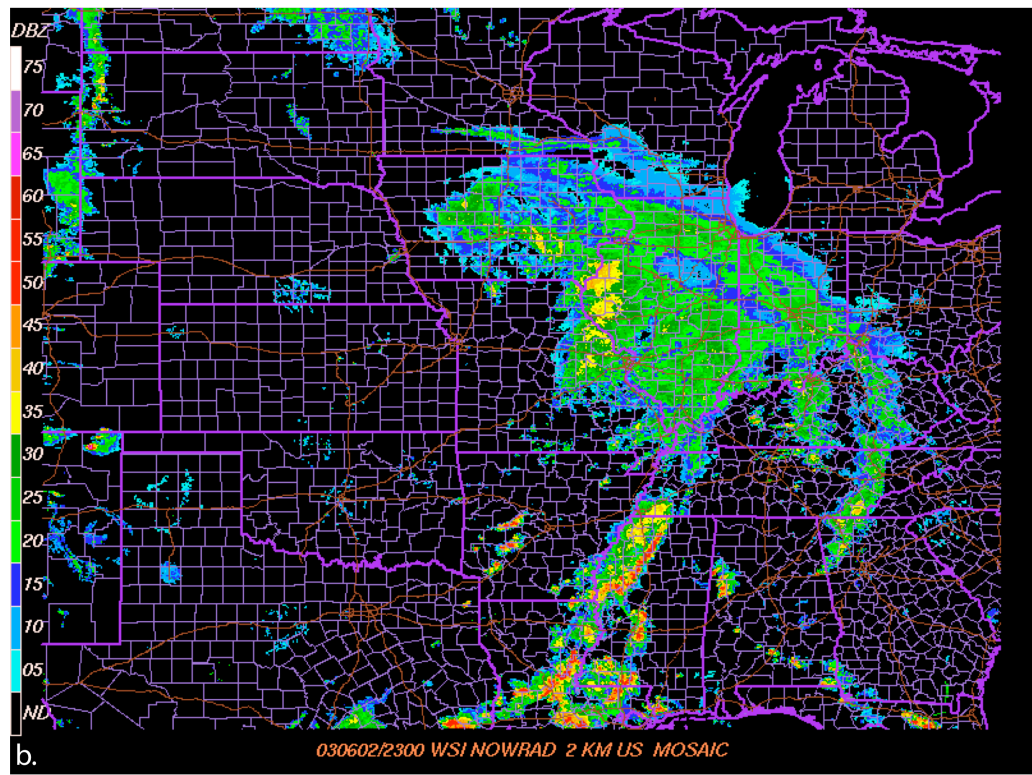
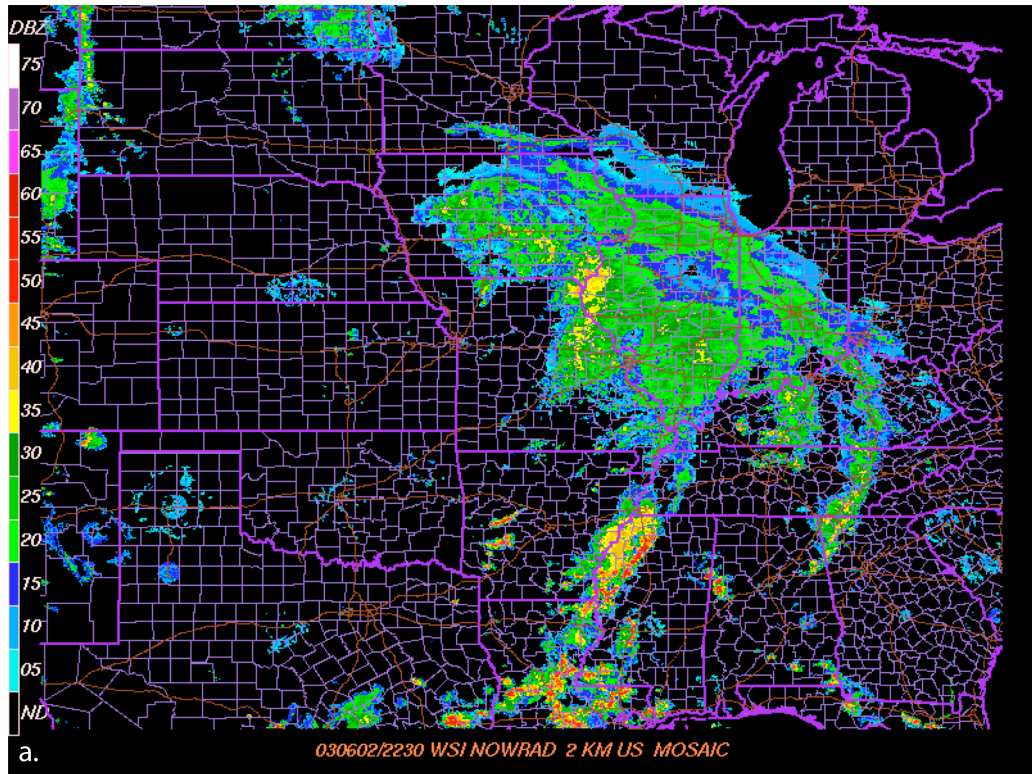


Figure 5.1: Analysis of the 2-3 June 2003 MCS as it moved over northern Mississippi. The 40 and 50 dBZ contours are drawn for the middle point of each of the six ELDORA flight legs. The alternating lighter and darker shades between the flight legs are used to differentiate features between the legs. The red line is the 0 – 3.5 km shear vector calculated from the 2300 UTC Okolona, MS wind profile data.

placed on the section of the MCS captured by the airborne radars, which were flying over northern Mississippi. Throughout the six flight legs, the portion of the convective line sampled by the airborne radars transitioned from linear to a bowed structure. The evolution of the reflectivity field can be seen in Fig. 5.3.

The first flight leg contains a mostly linear convective region, but embedded in the line are small bowed segments, which will be further investigated in the next chapter (Fig. 5.3a). Throughout the next two flight passes (Figs. 5.3b,c), the line remains fairly linear, but it also begins to show initial signs of becoming slightly convex, while still containing small, embedded bowed segments. In the first three flight legs, the convective line is solid and continuous, which is similar to what James et al. (2005) refers to as



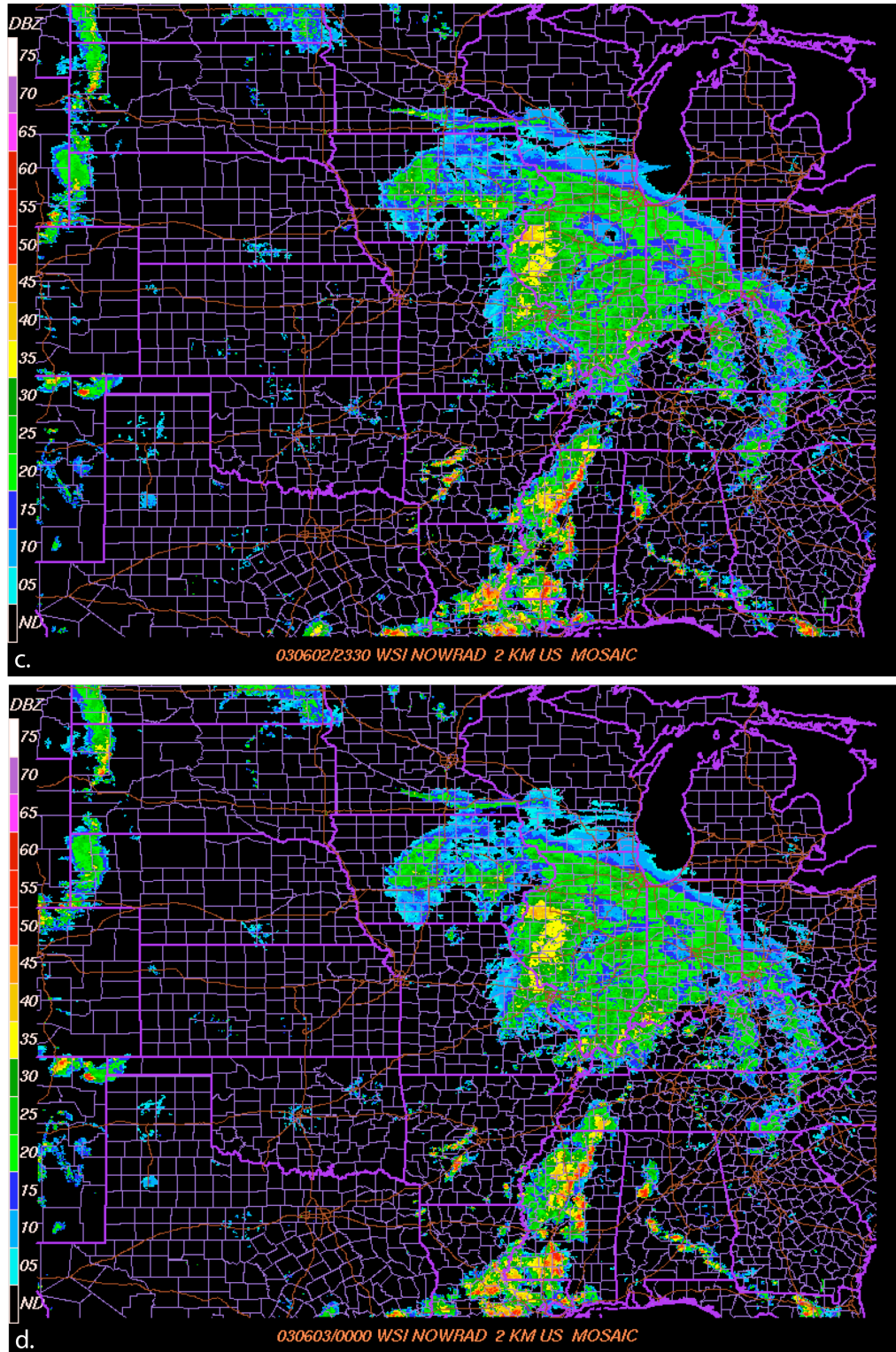
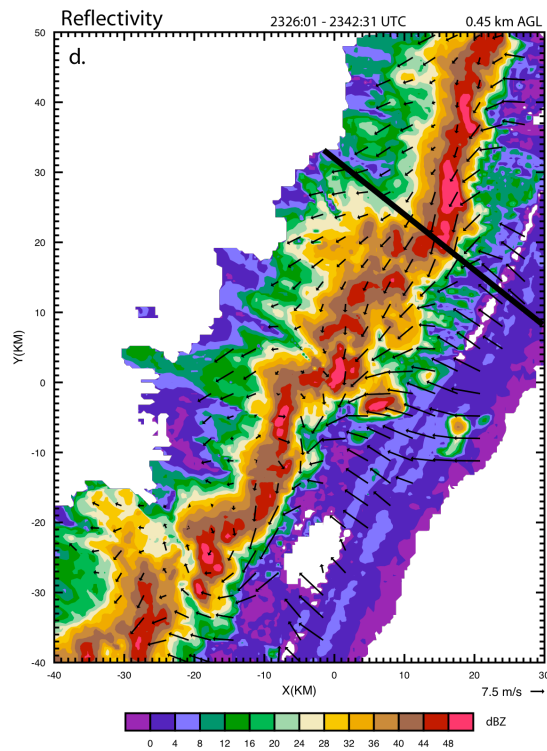
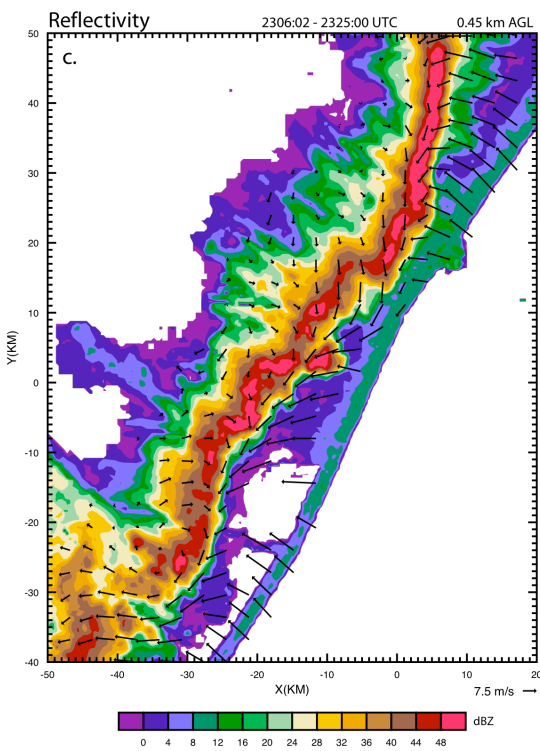
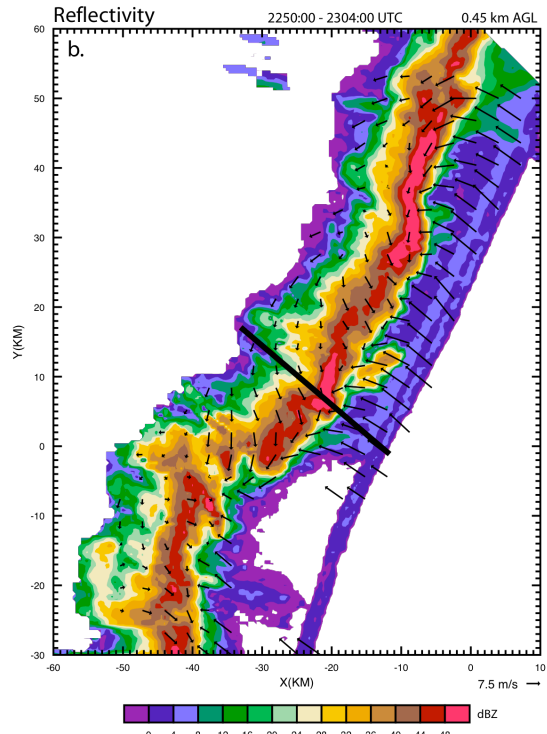
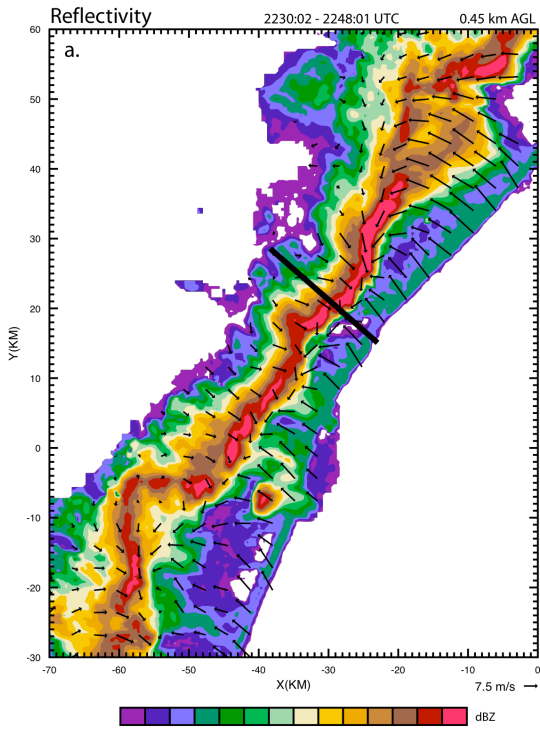


Fig. 5.2: NOWRAD composites of the BAMEX region for (a.) 2230 UTC, (b.) 2300 UTC, (c.) 2330 UTC, and (d.) 0000 UTC. The area of convection within the scope of this study is the MCS traversing across northern MS.

‘slabular.’” However, during the fourth flight pass, the convection near the middle of the line becomes less organized and more segmented, which is more characteristic of the ‘cellular’ classification by James et al. (2005; Fig. 5.3d). Essentially, this weakening divides the convective line into northern and southern segments. The division is denoted by a black line in Fig. 5.2d. The southern segment exhibits signs of bowing, while the northern area of convection is more linear in nature. In the fifth flight pass, the southern convective region becomes the main focus as it begins to actively “bow” outward (Fig. 5.3e). During this flight leg, there are also three convective cells ahead of the bowing convective line. These cells appear to be ingested by the convective line during the sixth flight leg, where the line becomes more organized and the most substantial bowing occurs (Fig. 5.3f). Within the larger-scale bow (~40 km), there are still small undulations within the convective line. One of the prominent features of the 2-3 June 2003 MCS, not obvious from Fig. 5.3 but more apparent at mid-levels, is a counter-rotating vortex couplet that begins to form in the third leg and becomes fully mature by the sixth leg. This counter-rotating couplet will be discussed in the following chapter; however, it is important to note that it begins to form as the convective system begins to bow.

The general flow characteristics throughout the flight legs exhibits the classic trailing stratiform model (Fig. 2.1). In the first leg, an approximate west-east cross-section is taken through one of the small-scale bowed segments (denoted by the black line in Fig. 5.3a). While the attenuation associated with ELDORA precludes sampling of the stratiform region, the convective region is still resolved well. At this stage, the updraft is nearly erect with updrafts greater than  $5 \text{ m s}^{-1}$ , and there are signs of



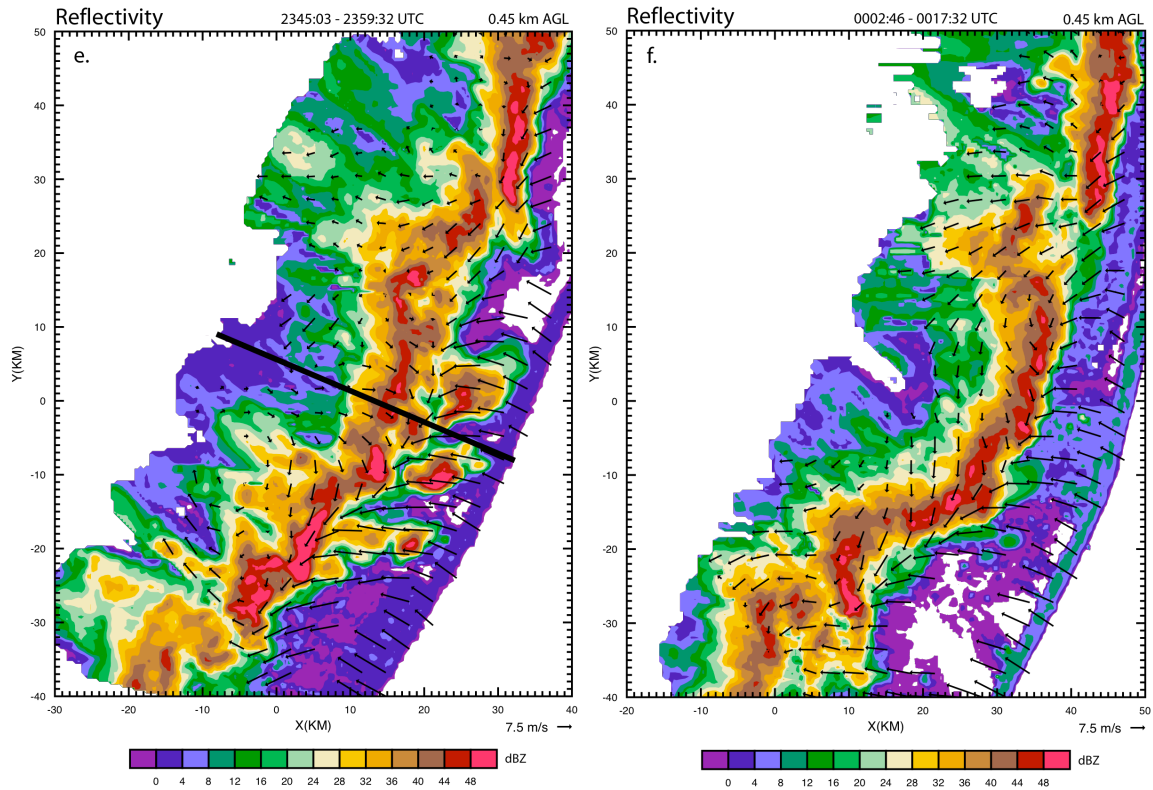


Figure 5.3: The storm-relative winds ( $\text{m s}^{-1}$ ) superimposed on the ELDORA reflectivity field (dBZ) at 0.45 km for all six flight legs (a.) 2230:02 – 2248:01 UTC, (b.) 2250:00 – 2304:00 UTC, (c.) 2306:02 – 2325:00 UTC, (d.) 2326:01 – 2342:31 UTC, (e.) 2345:03 – 2359:32 UTC, and (f.) 0002:46 – 0017:32 UTC. The black lines in (a.), (b.), and (e.) denote where cross-sections were taken in Fig. 5.4, Fig. 5.5, and Fig. 5.6, respectively. The black line in (d.) denotes the break between the northern and southern segments of the convective line.

descending rear-to-front flow (Fig. 5.4a,c). The most striking feature of this cross-section is the sloping, banded vorticity pattern (Fig. 5.4b). There is strong cyclonic vorticity at low levels ahead of the convective line extending upward into the convective line, and there is strong anticyclonic vorticity just behind the convective line. These strong bands of vorticity slope rearward with height. Also seen is an area of cyclonic vorticity at low levels just behind the anticyclonic band, but it is not as strong as the cyclonic vorticity ahead of the convective line. The banded vorticity pattern can be explained by the tilting

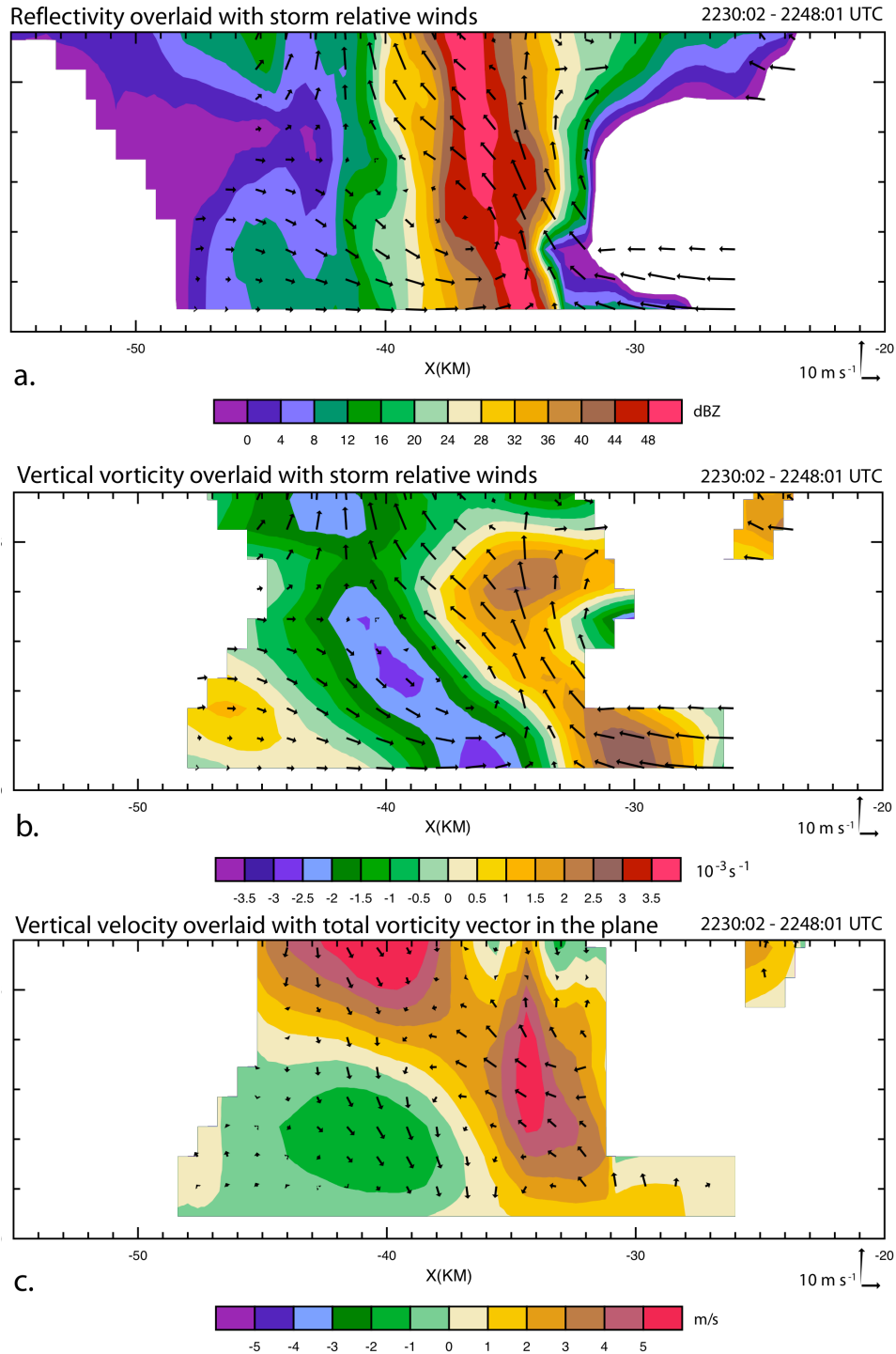


Figure 5.4: Series of approximately east-west cross-sections taken during the first leg using ELDORA analyses. (a.) Storm-relative wind vectors ( $\text{m s}^{-1}$ ) superimposed on the reflectivity (dBZ), (b.) Storm-relative wind vectors ( $\text{m s}^{-1}$ ) superimposed on vertical vorticity ( $\times 10^{-3} \text{ s}^{-1}$ ), and (c.) The total vorticity vector in the plane superimposed on vertical velocity ( $\text{m s}^{-1}$ ). The cross-section was taken through the area denoted by the black line in Fig. 5.3a.

of the environmental vorticity as it encounters the updraft (Fig. 5.4c). Upon examination of the total vorticity vector in the plane of the cross-section, it can be seen that ahead of the convective line, the vorticity vector crosses the strong, positive gradient associated with the updraft. Since the vector is pointing toward higher values, it is indicative of upward tilting. Similarly, on the backside of the updraft, where the vector is now pointing toward lower vertical velocities, there is downward tilting. The areas of upward and downward tilting are collocated with cyclonic and anticyclonic vorticity, respectively (Fig. 5.4b,c).

Approximate west-east cross-sections are also taken in the second and fifth legs, where quad-Doppler analyses are utilized. During the second flight pass, the main convective line is very erect (Fig. 5.5a). There is also a well-defined transition zone between the main convective line and the secondary reflectivity maximum associated with the stratiform region, and this zone is also collocated with a downdraft (Fig. 5.5a,c). There is pronounced ascending front-to-rear flow above a shallow (surface – 3 km) rear-inflow jet (Fig. 5.5c).

Figure 5.6 is a series of approximately west-east cross-sections taken during the fifth leg through the center of the counter-rotating vortex couplet, which is also near the apex of the bowed convection. There are several striking features, which are consistent with strong convective lines with trailing stratiform precipitation regions (e.g., Houze et al. 1989). The reflectivity field (Fig. 5.6a) depicts a strong, leading convective region with updrafts greater than  $5 \text{ m s}^{-1}$  (Fig. 5.6b), as well as a defined “bright band” near 3 km. There is stronger and more elevated rear-inflow than in the first and second flight passes, which Rotunno et al. (1988) and Weisman et al. (1988) attribute to a more

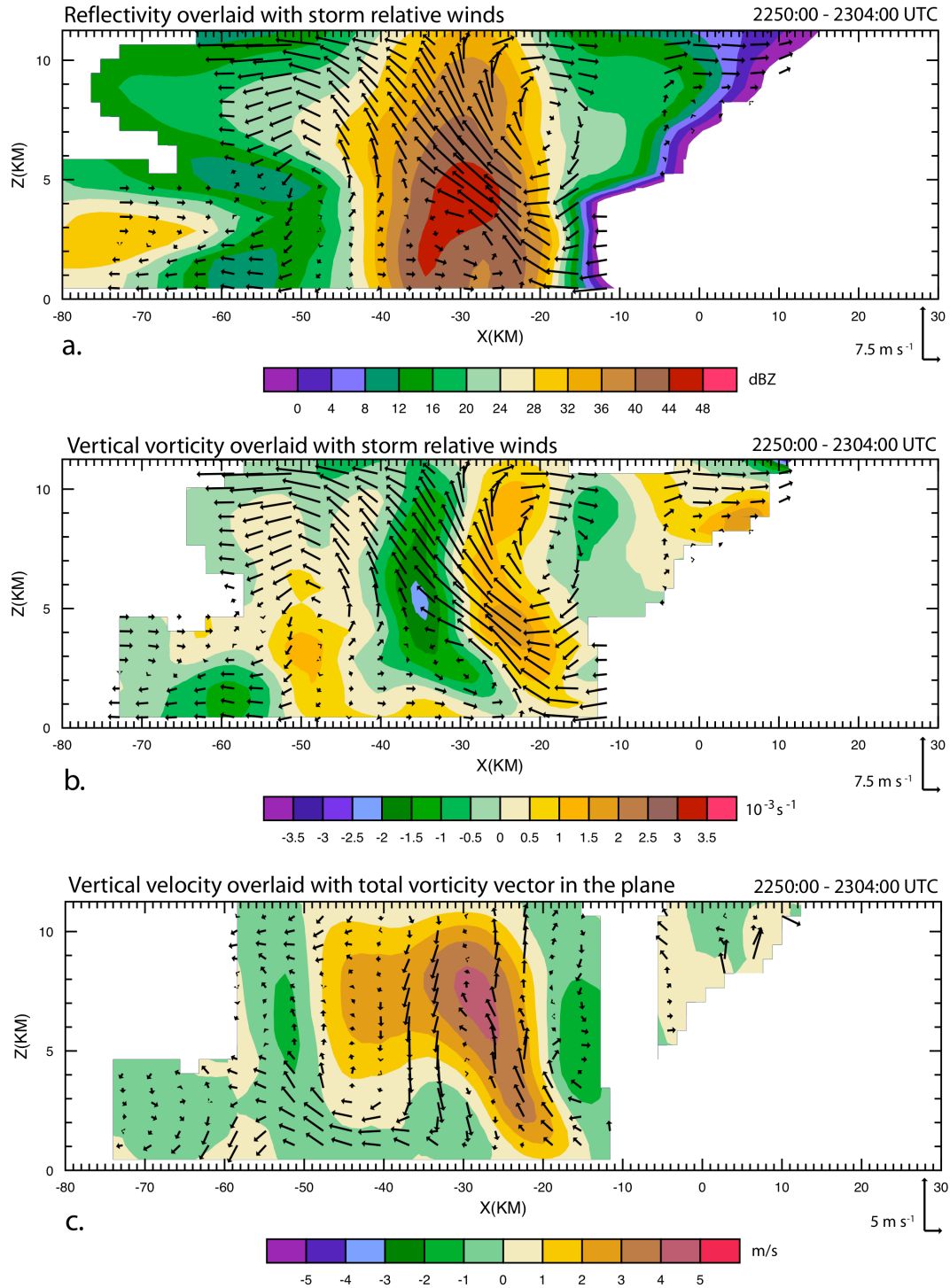


Figure 5.5: Series of approximately east-west cross-sections taken during the second leg using quad-Doppler analyses. (a.) Storm-relative wind vectors ( $m s^{-1}$ ) superimposed on the reflectivity (dBZ), (b.) Storm-relative wind vectors ( $m s^{-1}$ ) superimposed on vertical vorticity ( $\times 10^{-3} s^{-1}$ ), and (c.) The total vorticity vector in the plane superimposed on vertical velocity ( $m s^{-1}$ ). The cross-section was taken through the area denoted by the black line in Fig. 5.3b.

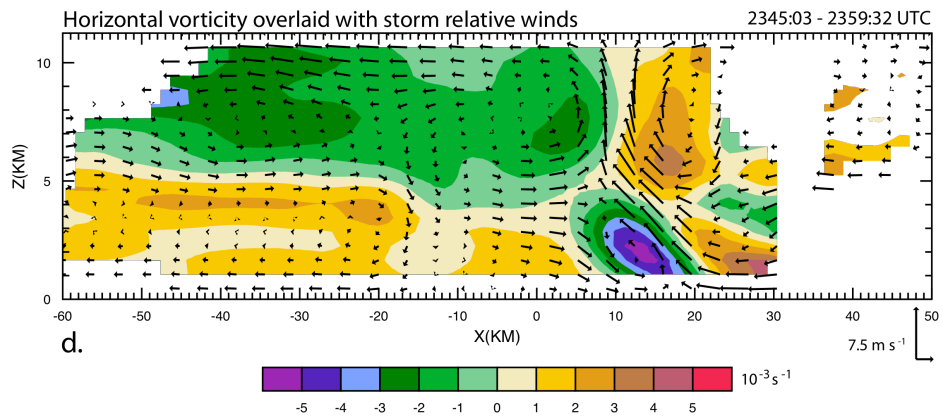
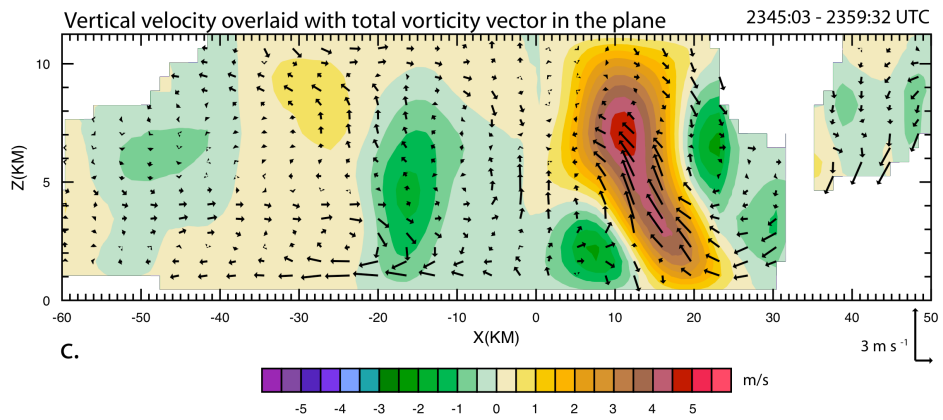
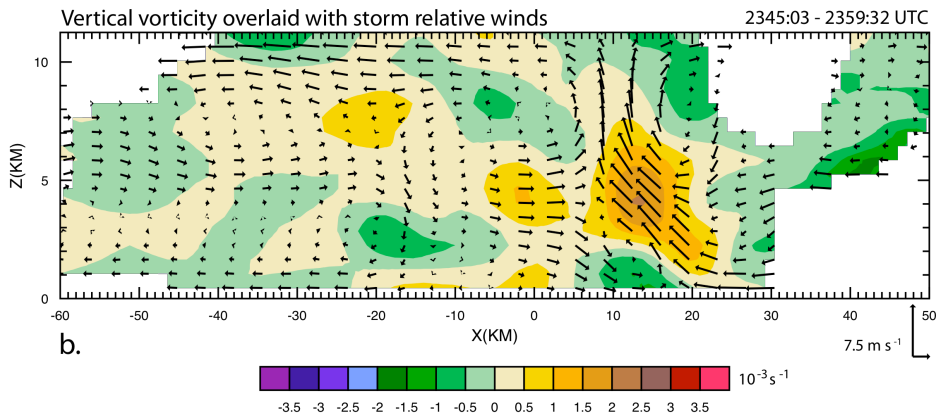
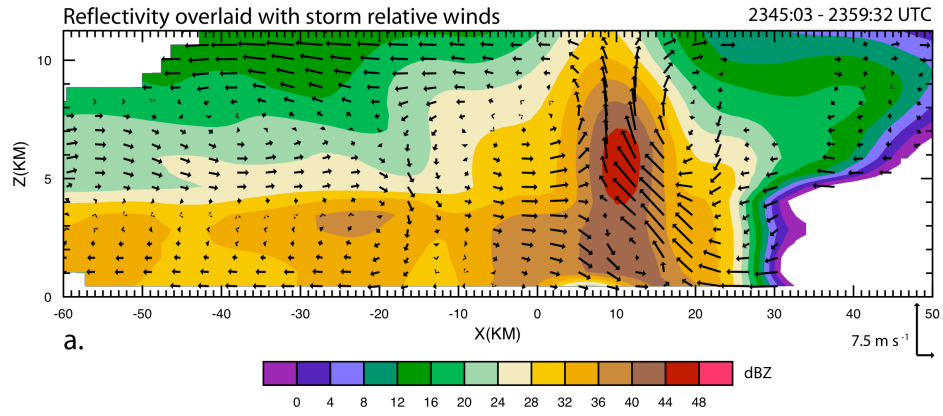


Figure 5.6: Series of approximately east-west cross-sections taken during the fifth leg using quad-Doppler analyses. (a.) Storm-relative wind vectors ( $\text{m s}^{-1}$ ) superimposed on the reflectivity (dBZ), (b.) Storm-relative wind vectors ( $\text{m s}^{-1}$ ) superimposed on vertical vorticity ( $\times 10^{-3} \text{ s}^{-1}$ ), (c.) The total vorticity vector in the plane superimposed on vertical velocity ( $\text{m s}^{-1}$ ), and (d.) Storm-relative wind vectors ( $\text{m s}^{-1}$ ) superimposed on horizontal vorticity. The cross-section was taken through the area denoted by the black line in Fig. 5.3e.

optimal balance between the cold-pool and the environmental low-level vertical shear.

The horizontal vorticity field displayed in Fig. 5.6c shows pattern also agrees with RKW theory. There is an area of strong negative horizontal vorticity ( $> -5 \times 10^{-3} \text{ s}^{-1}$ ) between the front to rear ascending current and the rear to front descending flow as is caused by the buoyancy gradients near the edge of the cold pool. The positive horizontal vorticity seen in the low-levels just ahead of the convective line is resultant of the environmental low-level vertical shear. The balance between the negative horizontal vorticity associated with the cold pool shear and the positive vorticity associated with the environmental low-level shear allow for a strong, erect updraft. Furthermore, the buoyancy gradients between the dense, surface cold pool and the warm, buoyant, ascending front to rear flow create their own horizontal vorticity. Figure 5.6d shows positive horizontal vorticity in conjunction with the cold pool region with negative horizontal vorticity atop the cold pool. The circulation generated from this vorticity pattern will act to enhance the rear-inflow.

Weisman and Davis (1998) take similar cross-sections through the center of counter-rotating vortices in a simulated squall line in order to investigate the general characteristics flow field associated with mesoscale vortices (Fig. 5.7). While some results from their study agree with the findings of this study, there are also some differences. As discussed in the previous chapter, there is weak-to-moderate

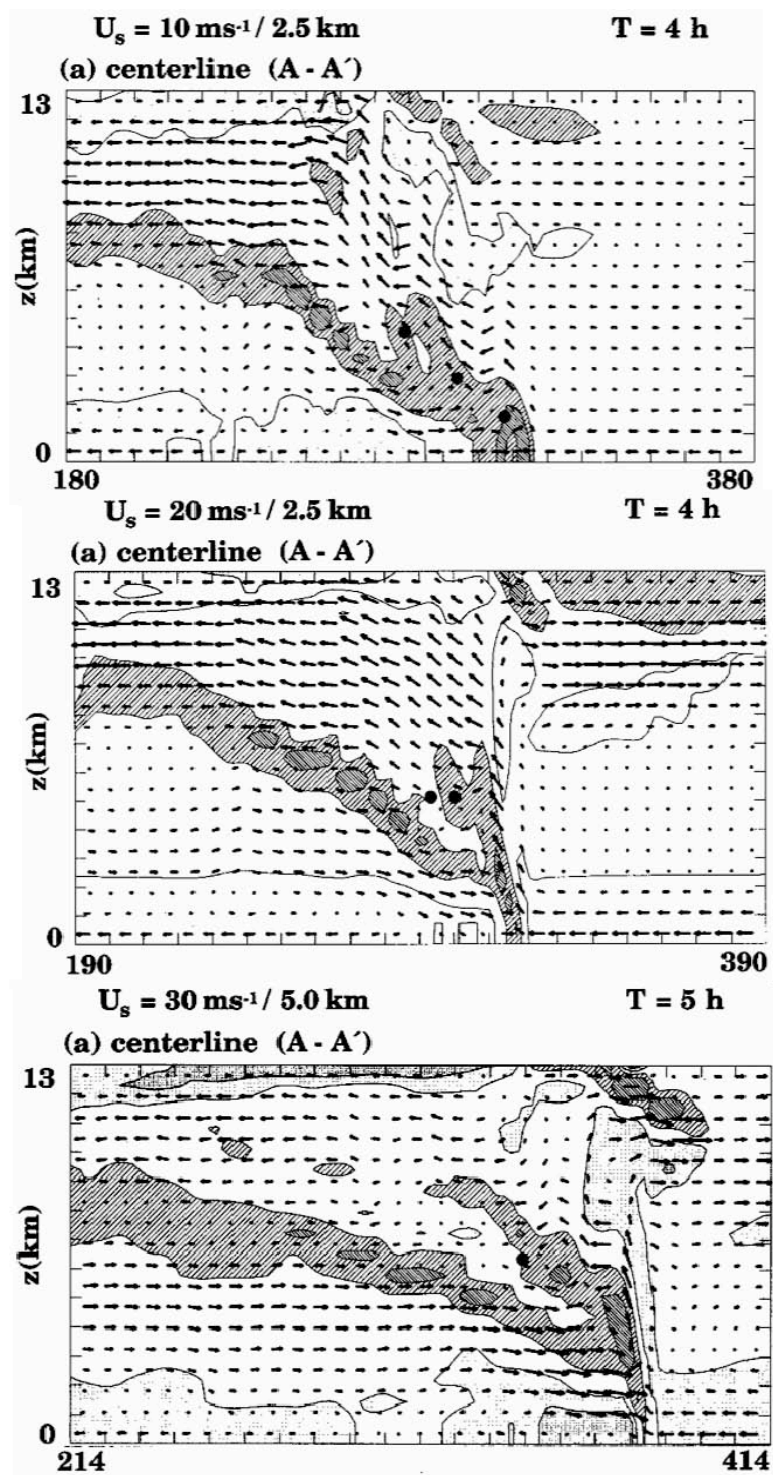


Figure 5.7: East-west vertical cross-sections through the centerline of the vortex couplet. Storm-relative winds were superimposed on horizontal vorticity for (a.)  $10 \text{ m s}^{-1}$ , (b.)  $20 \text{ m s}^{-1}$ , and (c.)  $30 \text{ m s}^{-1}$ . Taken from Weisman and Davis (1998).

environmental shear during the 2-3 June 2003 MCS. According to Weisman and Davis (1998), simulations with similar, weak shear ( $10 \text{ m s}^{-1}$  over the lowest 2.5 km; Fig. 5.7a) do not have as deep and strong updrafts or as much elevated rear-inflow as compared to the 2-3 June 2003 MCS (Fig. 5.6d). The cross-sections taken in the fifth flight leg is more consistent with the stronger and deeper shear simulations ( $20 \text{ m s}^{-1}$  over the lowest 2.5 km and  $30 \text{ m s}^{-1}$  over the lowest 5 km; Figs. 5.7b and 5.7c, respectively). Also, stronger shear simulations from Weisman and Davis (1998) show a similar storm evolution to the 2-3 June 2003 (i.e. organized bowing convection, both on the small and large scale), while their weak shear simulation did not produce significant, organized convection. It is also important to recall Weisman and Davis (1998) use environmental profiles with a shear vector perpendicular to the convective line, whereas the 2-3 June 2003 MCS has a component of along-line shear, which could account for the observable differences.

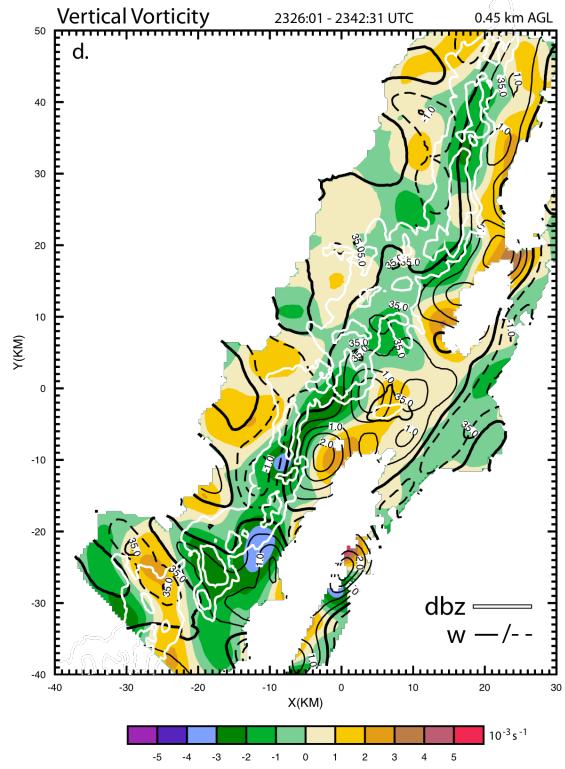
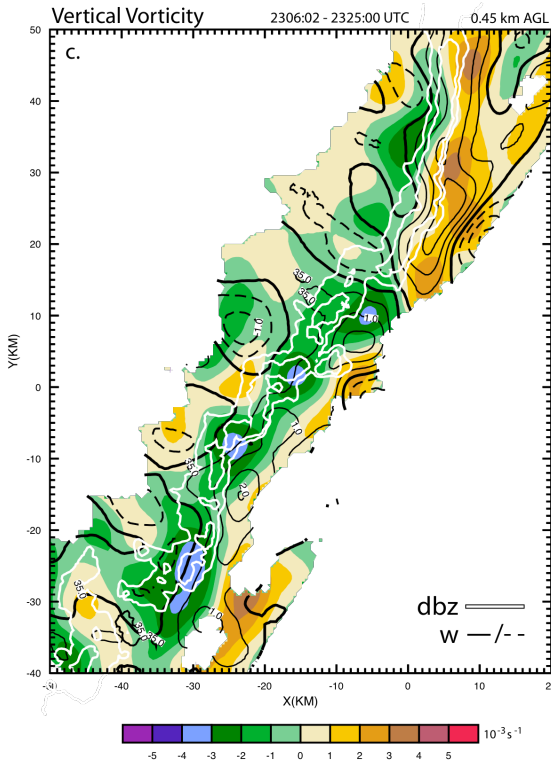
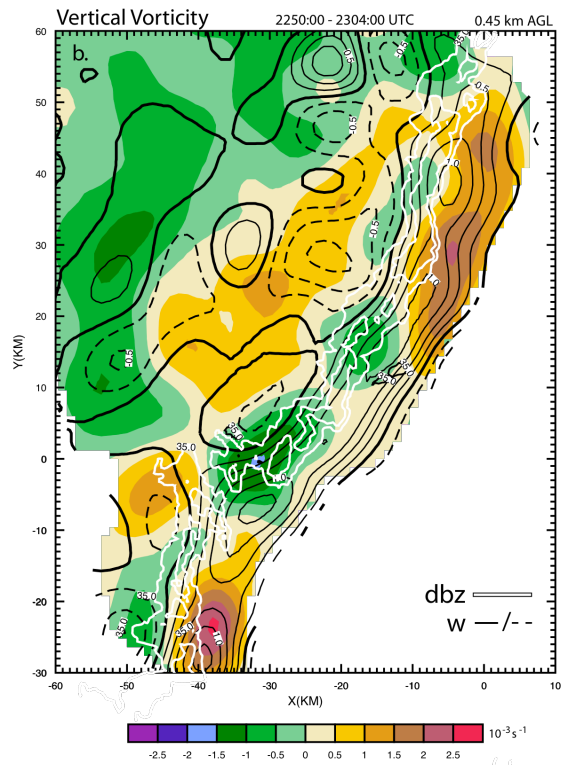
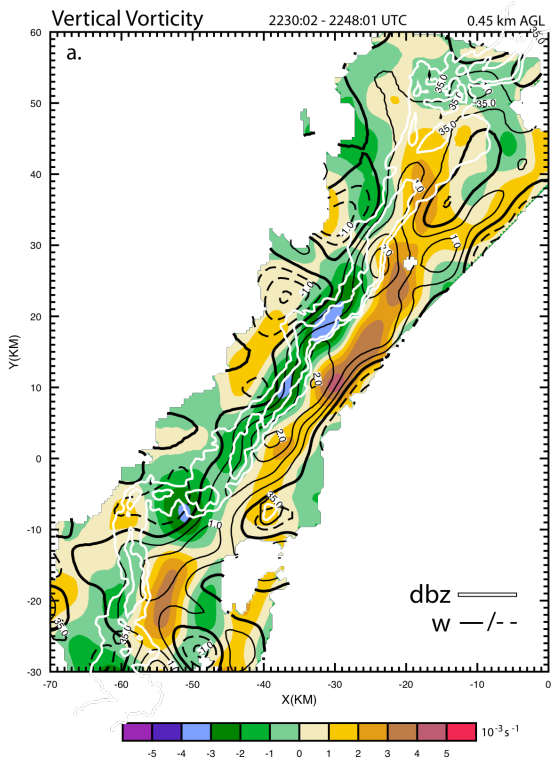
## **5.2 Banded vorticity pattern**

The 2-3 June MCS exhibited a vertical vorticity pattern that has been discussed only briefly in the literature (Zhang et al. 1989, BH91, and Zhang 1992). While typical MCSs have been documented to develop cyclonic (anticyclonic) vertical vorticity in the northern (southern) end of the storm, the 2-3 June MCS exhibits a banded vertical vorticity structure that is parallel to the convective line. The area ahead of the convective line is associated with cyclonic vorticity while the convective line and the area directly behind the line are associated with anticyclonic vorticity. While the convective line

evolves from a linear system to a bowed system, in general, the banded vorticity structure is retained.

In the first flight leg, there is a mostly continuous strip of anticyclonic vertical vorticity (generally, less than 10 km in width) associated with the convective line, and there is a continuous area of cyclonic vertical vorticity just ahead of the convective line (Fig. 5.8a). Quad-Doppler analysis is available for the second leg, allowing for both the convective and stratiform regions to be examined (Fig. 5.8b). While the general cyclonic/anticyclonic vorticity pattern is present near the convective line, there are some breaks within the anticyclonic band where weak cyclonic vorticity is present. Behind the anticyclonic band, there is a larger band of cyclonic vorticity, similar to the pattern seen in BH91 and reproduced in simulations by Zhang et al. (1989) and Zhang (1992). In the third and fourth legs, there is a continuous anticyclonic vorticity band associated with the convective line, and while the data ahead of the convective line are sparse, there is still evidence of the cyclonic vorticity band (Figs. 5.8c,d).

In the fifth leg, the banded cyclonic/anticyclonic structure is still present; however, there is another vorticity feature that is present (Fig. 5.8e). Behind the bowing convective region, there is an area of cyclonic (anticyclonic) vorticity near the northern (southern) end (developing vorticity couplet outlined by grey box in Fig. 5.8e). While this vortex couplet will be explored in future sections, it is important to note that the couplet is present in conjunction with the banded vorticity pattern. In the final leg, there are still traces of the banded vorticity pattern, but the pattern becomes somewhat disjointed as the system becomes significantly bowed (Fig. 5.8f). The northern end of the



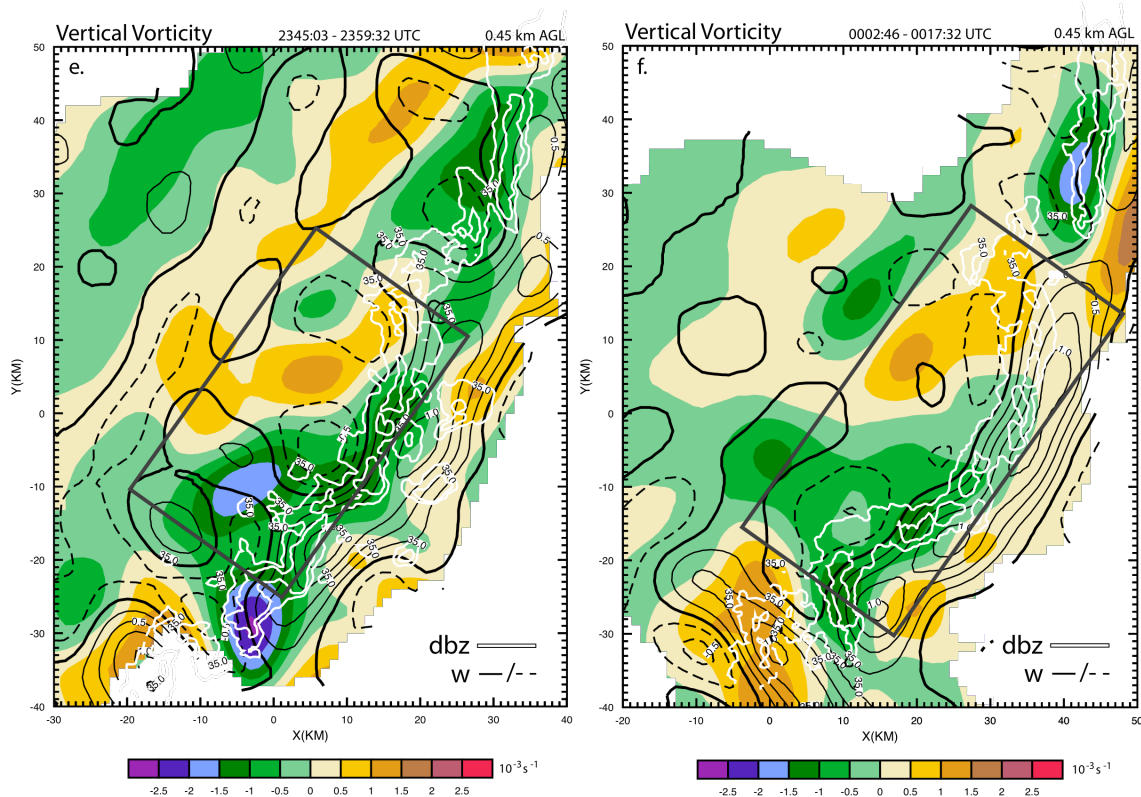


Figure 5.8: Vertical velocity ( $\text{m s}^{-1}$ ) and reflectivity (dBZ) at 0.45 km superimposed on the vertical vorticity ( $\times 10^{-3} \text{ s}^{-1}$ ) for the six flight legs: (a.) 2230:02 – 2248:01 UTC, (b.) 2250:00 – 23:04:00 UTC, (c.) 2306:02 – 2325:00 UTC, (d.) 2326:01 – 2342:31 UTC, (e.) 2345:03 – 2359:32 UTC, and (f.) 0002:46 – 0017:32 UTC. The first, third, and fourth flight legs (a., c., and d., respectively) are ELDORA analyses. The second, fifth, and sixth legs (b., e., and f., respectively) are quad-Doppler analyses. In all images, the 35 and 45 dBZ contours are denoted by white lines and use ELDORA reflectivity values. In the ELDORA only analyses, the vertical velocity is contoured every  $0.5 \text{ m s}^{-1}$ , and in the quad-Doppler analyses, the vertical velocity is contoured every  $0.25 \text{ m s}^{-1}$  (black lines). The grey boxes in (e.) and (f.) are where the vortex couplet begins to form in the low-levels, which is in conjunction with the larger-scale bowing.

bow is associated with cyclonic vorticity, while the middle and southern portion of the bow is associated with anticyclonic vorticity (denoted by grey box in Fig. 5.8f).

Due to the uniqueness of the cyclonic/anticyclonic vorticity bands, it is important to determine the reason for its existence. Recall that from the surface to 3.5 km, the environmental shear vector had a significant component parallel to the convective line (Figs. 4.5, 4.6, and 4.8). In many squall lines, the shear vector is perpendicular to the

convective line (e.g., Rotunno et al. 1988). In that type of environment, as discussed in Chapter 2, the tilting of environmental horizontal vorticity by the storm-scale downdraft generates cyclonic (anticyclonic) vertical vorticity in the northern (southern) region of the convective line. However, it is obvious from Fig. 5.8 that the typical vertical vorticity pattern does not readily occur in the 2-3 June MCS. The departure from this archetypal pattern is related to the along-line shear component.

It is hypothesized that the ambient horizontal vorticity, which has a component normal to the convective line, is tilted upward as it encounters the updraft, generating cyclonic vertical vorticity. The horizontal vorticity is then tilted downward in the gradient between the convective updraft and downdraft. This mechanism would produce anticyclonic vertical vorticity directly behind the cyclonic vertical vorticity, creating a banded vorticity pattern near the convective line. This is the exact structure seen and discussed in Fig. 5.4b,c. Once the horizontal vorticity has been tilted into the vertical, vertical vorticity can then be stretched, amplifying the bands. The validity of this hypothesis was examined by calculating the tilting and stretching terms of the vertical vorticity time tendency equation:

$$\frac{\partial \zeta}{\partial t} = - \left( u \frac{\partial \zeta}{\partial x} + v \frac{\partial \zeta}{\partial y} \right) - w \frac{\partial \zeta}{\partial z} - (\zeta + f) \left( \frac{\partial u}{\partial x} + \frac{\partial v}{\partial y} \right) - \left( \frac{\partial w}{\partial x} \frac{\partial v}{\partial z} - \frac{\partial w}{\partial y} \frac{\partial u}{\partial z} \right) \quad (5.1)$$

The first term on the right hand side is the horizontal vorticity advection, the second term is the vertical vorticity advection, the third term is the stretching term, and the last term is the tilting/twisting term. It is important to note that the tilting term can change the sign of the vertical vorticity, while the stretching term can only act to amplify or reduce the magnitude of the vertical vorticity (as long as  $\zeta$  exceeds  $f$ ).

Figure 5.9 displays the tilting and stretching values for the first flight pass at 1.05 km. Also, the hodograph from the Okolona, MS wind profiler at 2200 UTC is included on Fig. 5.9a in order to show the shear vector in relation to the convective line. As expected, there is strong upward tilting ahead of the convective line (some areas  $> 5 \times 10^{-6} \text{ s}^{-1}$ ), while the area near and behind the convective line is largely covered by negative values, indicating downward tilting (Fig. 5.9a). There is also strong stretching and amplification of the preexisting vertical vorticity (Fig. 5.9b). In fact, when the tilting and stretching terms are summed, there are strong positive values ahead of and parallel to the convective line, and negative values associated with and behind the convective line (not shown). These bands are also collocated with the cyclonic and anticyclonic bands, showing that both tilting and stretching contribute to the observed vertical vorticity field. The second and fifth flight legs show similar tilting patterns (Fig. 5.10a and 5.11a). Both legs are associated with positive tilting ahead of the convective line, with predominantly negative tilting associated with and behind the convective line. Another key feature to observe is the parallel orientation of the positive and negative tilting terms in the stratiform region. Overlaying both the vertical velocity field and the horizontal vorticity vectors on the tilting term reveals that the banded tilting structure is a direct result of the horizontal vorticity vectors being nearly perpendicular to the vertical velocity field (Figs. 5.10a and 5.11a).

The stretching term in the second leg has large negative values behind the southern part of the convective line, where there is already strong preexisting anticyclonic vorticity (Fig. 5.10b). In fact, a large, negative stretching term is present on the southern part of the convective line in all six legs, amplifying the vertical vorticity.

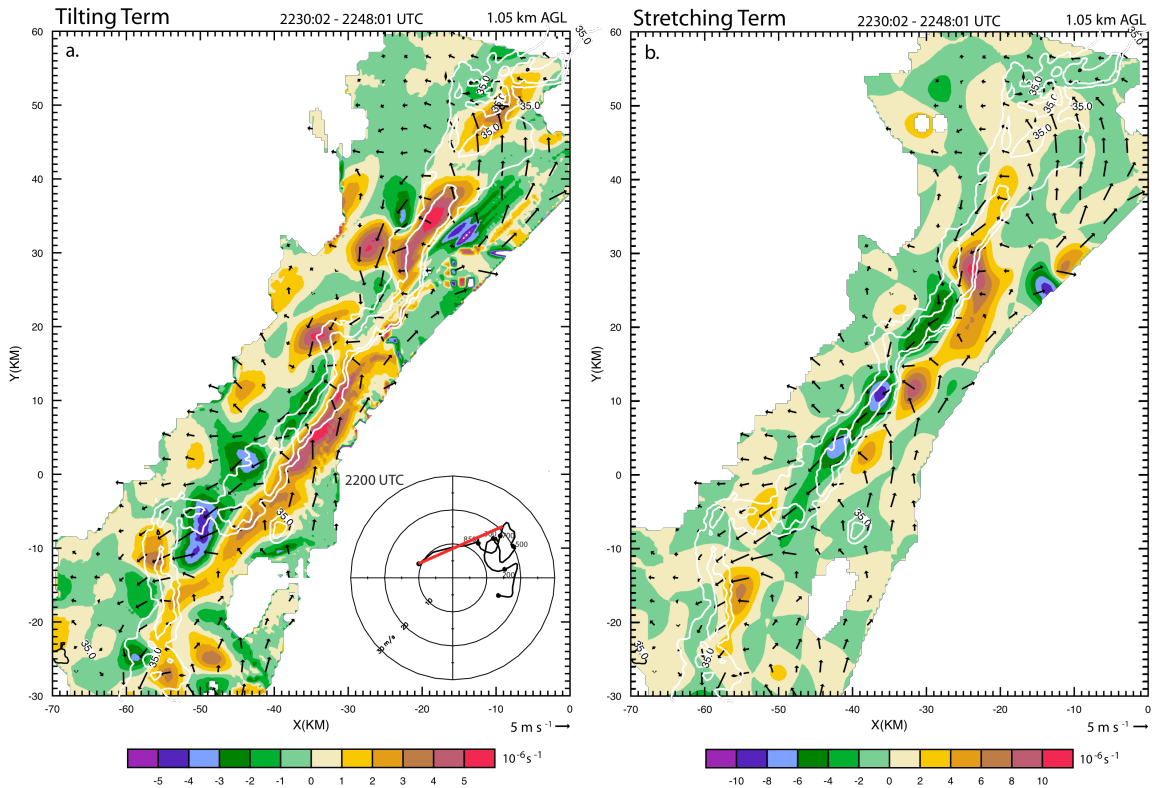


Figure 5.9: The tilting and stretching terms calculated from the ELDORA analyses for the first flight leg (2230:02 – 2248:01 UTC) at 1.05 km. (a.) Horizontal vorticity vectors are superimposed on the tilting term ( $\times 10^{-6} \text{ s}^{-1}$ ). The 35 and 45 dBZ lines are contoured in white. The hodograph from 2200 UTC from the Okolona wind profiler is included with the 0 – 3.5 km shear vector denoted by the red line. (b.) Horizontal vorticity vectors are superimposed on the stretching term ( $\times 10^{-6} \text{ s}^{-1}$ ). The 35 and 45 dBZ lines are contoured in white.

In the first leg (Fig. 5.9), the cyclonic/anticyclonic vertical vorticity pattern is already present, which indicates that vertical vorticity was already being generated from the tilting of the horizontal vorticity. In certain areas along the convective line, namely the southernmost end, the tilting term is the dominant term, which would be expected in the earlier times of the convection’s lifecycle. When comparing the magnitudes of the tilting versus the stretching terms in the second and fifth legs (Figs. 5.10 and 5.11), the southern end of the convective line typically exhibits a dominant tilting term ahead of the

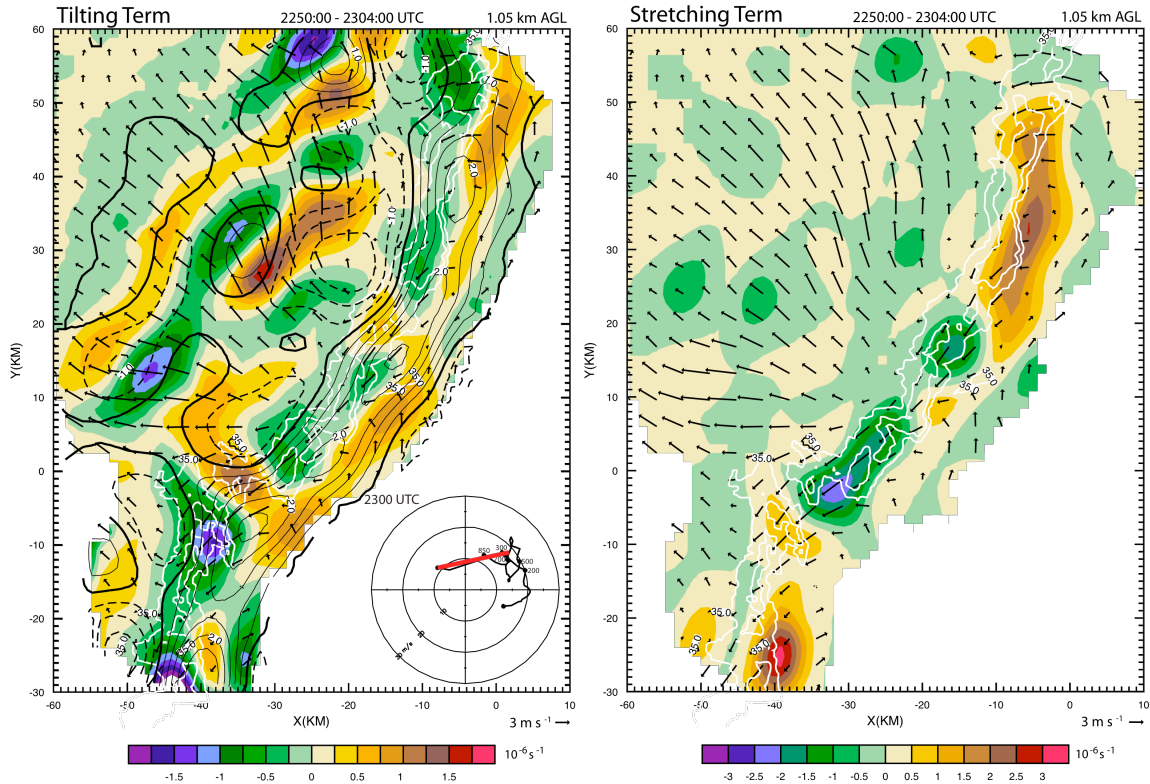
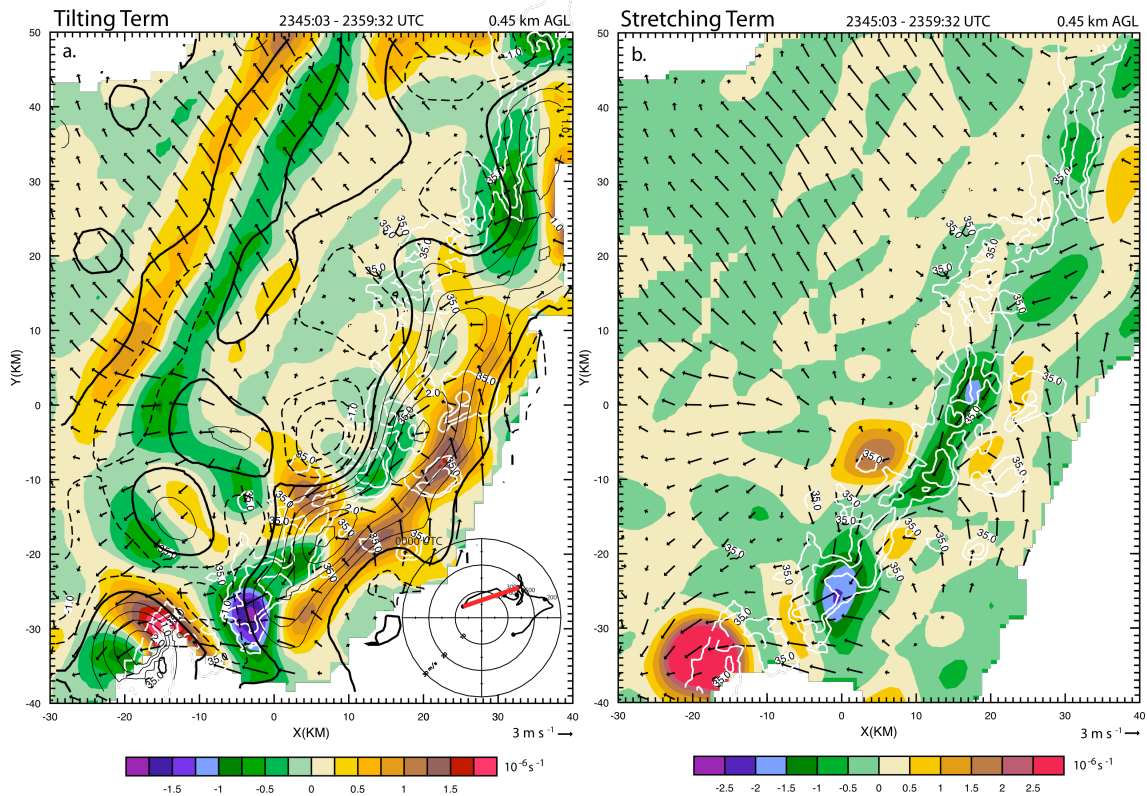


Figure 5.10: The tilting and stretching terms calculated from quad-Doppler analyses for the second flight leg (2250:00 – 2304:00 UTC) at 1.05 km. (a.) Horizontal vorticity vectors are superimposed on the tilting term ( $\times 10^{-6} \text{ s}^{-1}$ ). The 35 and 45 dBZ lines (from ELDORA) are contoured in white. The vertical velocity is contoured at  $0.5 \text{ m s}^{-1}$  and is denoted with black lines. The hodograph from 2300 UTC from the Okolona wind profiler is included with the 0 – 3.5 km shear vector denoted by the red line. (b.) Horizontal vorticity vectors are superimposed on the stretching term ( $\times 10^{-6} \text{ s}^{-1}$ ). The 35 and 45 dBZ lines (from ELDORA) are contoured in white.

convective line in association with the cyclonic vorticity, while the stretching term is the dominant term behind the line in association with the anticyclonic vorticity.

### 5.3 Discussion

The only observational study to discuss a banded vorticity pattern is BH91, which investigated the 10-11 June 1985 squall line during PRE-STORM. The same system, including the banded vorticity pattern, was successfully simulated by Zhang et al. (1989)



5.11: The tilting and stretching terms calculated from quad-Doppler analyses for the fifth flight leg (2345:03 – 2359:32 UTC) at 1.05 km. (a.) Horizontal vorticity vectors are superimposed on the tilting term ( $\times 10^{-6} \text{ s}^{-1}$ ). The 35 and 45 dBZ lines (from ELDORA) are contoured in white. The vertical velocity is contoured at  $0.5 \text{ m s}^{-1}$  and is denoted with black lines. The hodograph from 0000 UTC from the Okolona wind profiler is included with the 0 – 3.5 km shear vector denoted by the red line. (b.) Horizontal vorticity vectors are superimposed on the stretching term ( $\times 10^{-6} \text{ s}^{-1}$ ). The 35 and 45 dBZ lines (from ELDORA) are contoured in white, anticyclonic vertical vorticity. In the stratiform region, there is not a distinct pattern in the stretching term as there is in the tilting term (Figs. 5.10b and 5.11b).

and Zhang (1992). While BH91 acknowledge the cyclonic band ahead of the convective region, it is not within the scope of their study, due to data collection restraints. They conclude that the mid-level banded structure within the stratiform region is from tilting of the horizontal vorticity that is associated with the subsidence gradients present in the stratiform in conjunction with the descending rear-inflow jet. Once the vertical vorticity is generated via tilting processes, it is stretched, amplifying the vertical vorticity.

However, their calculations show that stretching is a factor of 2 – 10 less than the tilting. Interestingly, the MCS they were studying also displayed an along-line wind component, similar to the 2-3 June 2003 MCS. They hypothesize that this resulted in horizontal vorticity vectors that were perpendicular to the convective system, which would allow for the upward and downward tilting of horizontal vorticity within the subsidence of the stratiform region, producing a banded vorticity structure.

While there are striking similarities between this study and BH91 (i.e. banded vorticity structure and along-line shear), there are also differences. Namely, their study focused on the mid-level vorticity structure within the stratiform region, whereas this study places an importance on the low- and mid-level cyclonic/anticyclonic vorticity pattern associated with both the convective and stratiform regions. Since this study was able to use high-resolution dual- and quad-Doppler analyses, the convective region can be investigated with confidence for all six legs, and coverage of the stratiform is available for three legs. The other large difference between the current study and BH91 are the scales on which the events occurred. The width of the anticyclonic band in the BH91 study was on the scale of 50 km, whereas, in this study, the anticyclonic band rarely exceeded 10 km.

This study agrees with BH91 in regards to their hypothesis that tilting is the major mechanism that drives the banded structure in the stratiform region. As discussed above, there is a banded structure in the tilting term within the stratiform region (Figs. 5.10a and 5.11a), which directly related to the vertical velocity field and the horizontal vorticity vectors that are oriented perpendicular to the convective line. While BH91 looked exclusively at the mid-levels, evidence of this tilting pattern is present at both the low-

and mid-levels in this study (the mid-level tilting plots are not shown). Also similar to BH91, there are no coherent patterns in the stretching term, and the magnitudes of the stretching term are small in comparison to the tilting term in the stratiform region.

Zhang (1992) focused on the wake low that developed in the stratiform region of the 10-11 June 1985 squall line; however, mechanisms for the banded vertical vorticity structure along the convective were also offered. In agreement with this study, they concluded, through their simulations, that the upward and downward tilting of the horizontal vorticity creates the cyclonic and anticyclonic band, with stretching then amplifying the vorticity.

A key relationship between the studies involving the 10-11 June 1985 squall line and this study is the component of along-line shear. Convection with along-line shear has only recently been delved into by Parker (2007a,b), and it is often associated with parallel stratiform regions or highly asymmetric trailing stratiform regions. There have been many observational and modeling studies which investigate line-end vortices within a line-perpendicular shear environment and/or that are associated with a trailing stratiform region, but not much work has been completed on the ability for systems with an along-line wind shear component to produce line-end vortices. The cross-sections seen in Figs. 5.4, 5.5, and 5.6 are typical of a trailing stratiform MCS; however, trailing stratiform MCSs often develop dominant cyclonic vorticity in the northern portion of the storm. While this particular MCS eventually develops a counter-rotating couplet with a more typical structure, the parallel, banded vorticity structure associated with the convective line remained throughout all six legs, which is atypical of trailing stratiform MCSs. While the system does display characteristics typically seen in MCSs, it also

develops and maintains features that have not been commonly observed, which is strongly related to the environmental shear profile.

## Chapter 6

### VORTICES WITHIN THE MCS

The 2-3 June 2003 MCS contained meso- $\gamma$  vortices along the convective line as well as a counter-rotating vortex couplet that formed behind the convective line. A description of the vortices will be given and the processes of their formation and maintenance will be discussed.

#### 6.1 Small-scale vortices

##### 6.1.1 Overview of small-scale vortices

Throughout the time period in which data was collected during the 2-3 June 2003 MCS, several meso- $\gamma$  (5 – 15 km) vortices were observed. While emphasis in the literature has been placed on low-level meso- $\gamma$  vortices (e.g. Davis and Weisman 1994, Trapp and Weisman 2003, Wakimoto et al. 2006, and Atkins and St. Laurent 2009), this study attempts to investigate the low- and mid-level vortices. The unique banded vorticity structure will be revisited, as both anticyclonic and cyclonic vortices are observed within the vorticity bands during the six flight legs.

In the first leg, there are several small-scale, cyclonic and anticyclonic vortices that are embedded within the cyclonic and anticyclonic bands, respectively,

## Storm-relative winds and reflectivity superimposed on vertical vorticity

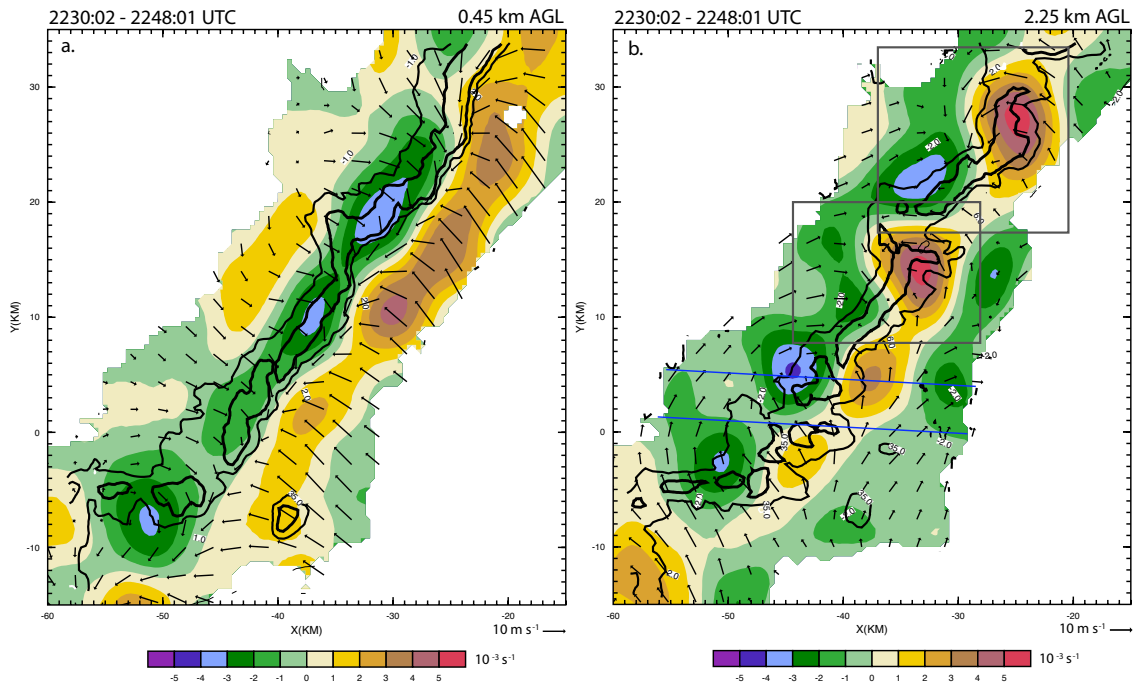


Figure 6.1: ELDORA reflectivity (dBZ), vertical velocity ( $m s^{-1}$ ), and storm-relative winds superimposed on the vertical vorticity ( $s^{-1}$ ) field at (a.) 0.45 km AGL and (b.) 2.25 km AGL. The black lines are reflectivity; the thin line is 35 dBZ, and the thick line is 45 dBZ. The blue lines in (b.) denote where cross-sections were taken, which can be seen in Figs. 6.7 and 6.12. The grey boxes in (b.) highlight the small-scale convective bowed segments.

in both the low- and mid-levels (Fig. 6.1a,b). The vortices embedded within the cyclonic and anticyclonic bands are spread throughout the span of the line. The cyclonic vortices are located on or ahead of the convective line, and the anticyclonic vortices are directly behind the convective line. The two northernmost pairs of cyclonic and anticyclonic vortices are associated with small-scale bowed convective segments ( $\sim 15$  km long; marked by the grey boxes in Fig. 6.1b). The cyclonic vortices are located on the northern part of the bowed segment, while the anticyclonic vortices are associated with the southern area of the bowed segment. The counter-rotating circulations have concentrated rear-inflow between the vortices, which is coincident with the bowed region. While on a

## Storm-relative winds and reflectivity superimposed on vertical vorticity

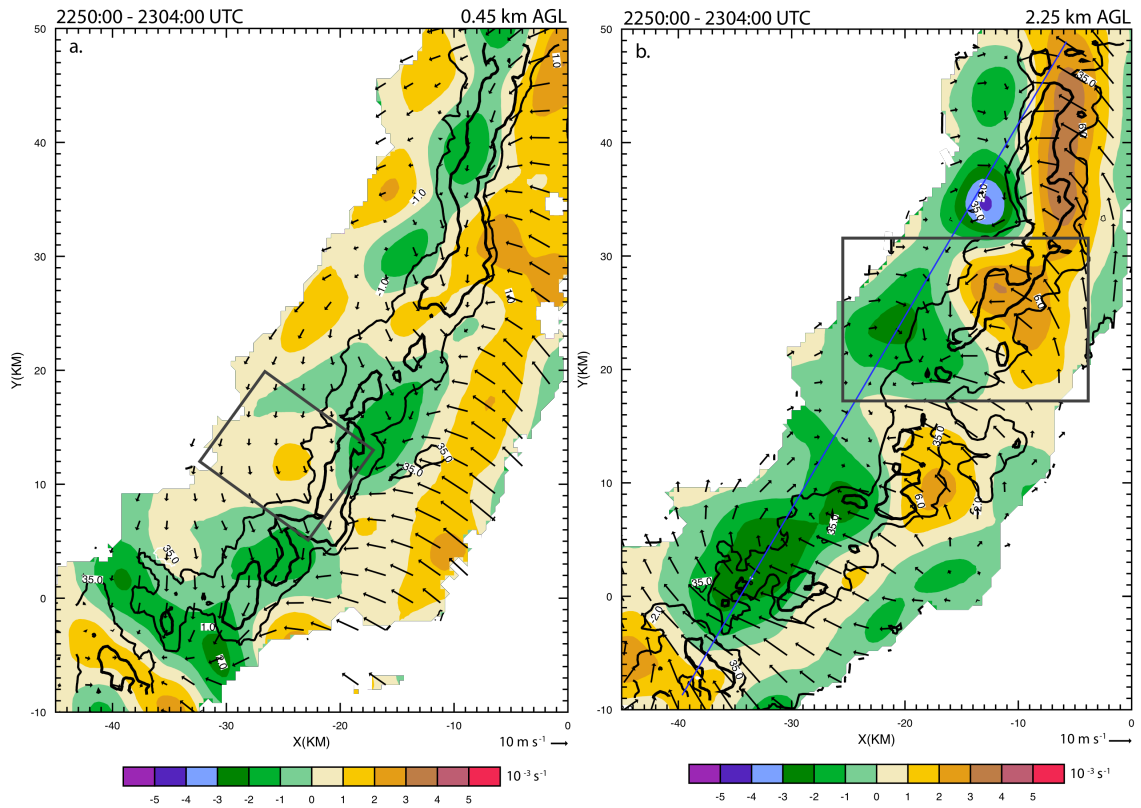


Figure 6.2: ELDORA<sup>1</sup> reflectivity (dBZ), vertical velocity ( $\text{m s}^{-1}$ ), and storm-relative winds superimposed on the vertical vorticity ( $\text{s}^{-1}$ ) field at (a.) 0.45 km AGL and (b.) 2.25 km AGL. The black lines are reflectivity; the thin line is 35 dBZ, and the thick line is 45 dBZ. The blue line in (b.) denote where a cross-section was taken, which can be seen in Fig. 6.14. The grey box in (a.) denotes the area of cyclonic vortex development. The grey box in (b.) denotes a pair of cyclonic and anticyclonic vortices.

significantly smaller scale than a classic bow echo, these counter-rotating vortices display similar characteristics (e.g. cyclonic (anticyclonic) vorticity in the northern (southern) end and concentrated rear-inflow).

<sup>1</sup> ELDORA analyses were used for the 2<sup>nd</sup>, 5<sup>th</sup>, and 6<sup>th</sup> legs when discussing the small-scale vortices, even though quad-Doppler analyses were available. In order to accurately compare the vortices from one leg to the next, using the ELDORA analyses provided better continuity. However, when discussing larger features, i.e. the mid-level vortex couplet, quad-Doppler analysis was used again.

During the second leg, there is still evidence of cyclonic and anticyclonic vortices along the length of convective line, but a majority of the vortices are not as strong or defined as they were in the previous leg, especially at 0.45 km (Fig. 6.2a,b). In both the low- and mid-levels, the northernmost cyclonic vortices from the previous leg have become an elongated area of enhanced cyclonic vorticity on the northern end of the convective line. At 2.25 km, the anticyclonic vortices from the first leg have also changed in size and strength; there are two negative vorticity maxima on the southern portion of the convective line that begin to merge together, forming an area of enhanced anticyclonic vorticity on the southern line-end. Near the center of the convective line, a cyclonic and anticyclonic vortex pair have counter-rotating circulations with enhanced rear-inflow (marked by the grey box in Fig. 6.2b).

The third leg also contains numerous cyclonic and anticyclonic vortices at low- and mid-levels (Fig. 6.3a,b). At 0.45 km, there are several anticyclonic vortices spread throughout the length of the convective line, and the band of anticyclonic vorticity is continuous. However, at 2.25 km, there is a marked change in the vorticity pattern behind the convective line. A cyclonic vorticity maximum ( $3.6 \times 10^{-3} \text{ s}^{-1}$ ) is embedded within the anticyclonic band, and it is located between two strong anticyclonic vortices ( $\sim 5.5 \times 10^{-3} \text{ s}^{-1}$ ). The velocity field (not shown) displays an area of enhanced rear-inflow between the cyclonic vortex and the anticyclonic vortex to the south of the cyclonic vortex. This developing counter-rotating vortex couplet will become the focus of the next section. Also, at 2.25 km, there are strong cyclonic and anticyclonic vortex pairs on the northern and southern line-ends. The small-scale, line-end vortex couplets are associated with enhanced rear-inflow and undulations in the reflectivity field. These

### Storm-relative winds and reflectivity superimposed on vertical vorticity

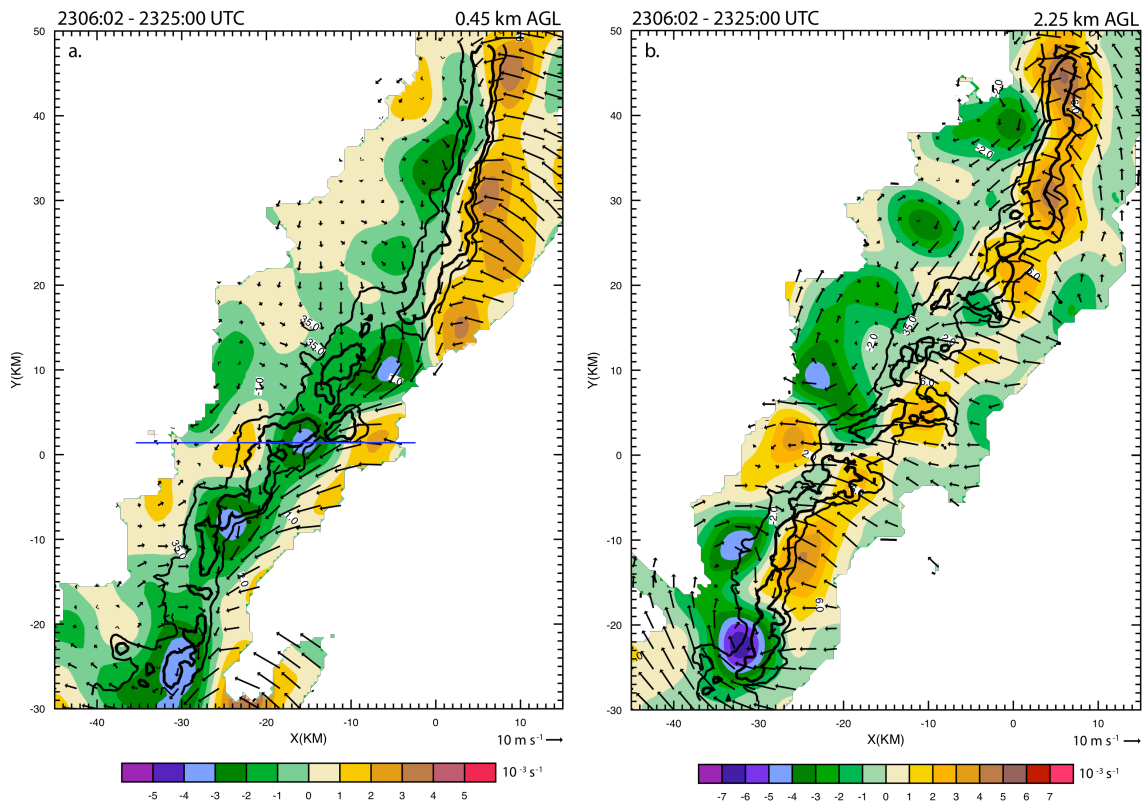


Figure 6.3: ELDORA reflectivity (dBZ), vertical velocity ( $\text{m s}^{-1}$ ), and storm-relative winds superimposed on the vertical vorticity ( $\text{s}^{-1}$ ) field at (a.) 0.45 km AGL and (b.) 2.25 km AGL. The black lines are reflectivity; the thin line is 35 dBZ, and the thick line is 45 dBZ. The blue line in (a.) denotes where cross-sections was taken, which can be seen in Fig. 6.10.

characteristics are similar to the previous legs; however, the vortex couplets have transitioned from being present across the entire convective line to being mainly on the ends of the convective segment that was sampled by the airborne radar.

In the fourth flight leg, at 2.25 km, the two strong anticyclonic vortices that were anchored to the southern end of the convective line in the third leg have begun to merge together (Fig. 6.4b). The anticyclonic vortex is still directly behind the convective line, but it now seems to become part of an independent larger-scale counter-rotating vortex

## Storm-relative winds and reflectivity superimposed on vertical vorticity

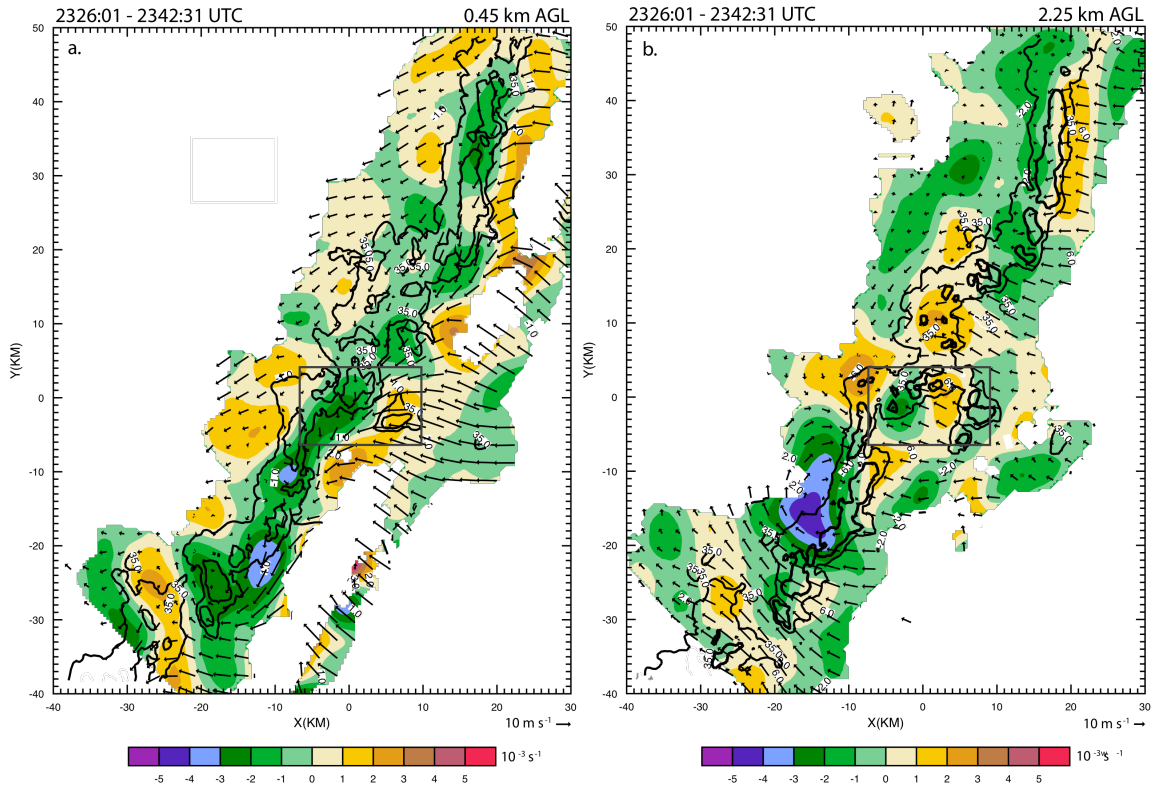


Figure 6.4: ELDORA reflectivity (dBZ), vertical velocity ( $\text{m s}^{-1}$ ), and storm-relative winds superimposed on the vertical vorticity ( $\text{s}^{-1}$ ) field at (a.) 0.45 km AGL and (b.) 2.25 km AGL. The black lines are reflectivity; the thin line is 35 dBZ, and the thick line is 45 dBZ. The grey box represents a forming pair of vortices.

couplet rather than being just one of the small-scale vortices within the cyclonic/anticyclonic banded vorticity pattern. In general, the banded vorticity pattern seen in the previous legs at 2.25 km is not as coherent in the fourth leg; however, it is still present in the low-levels (Fig. 6.4a).

Whereas the notable vorticity features in the first three legs are the small-scale vortices associated with the convective line, the vorticity field in the later legs becomes more affected by the counter-rotating vortices on the southern portion of the convective line. In the fifth flight leg, there are several, weak, small-scale cyclonic and anticyclonic

## Storm-relative winds and reflectivity superimposed on vertical vorticity

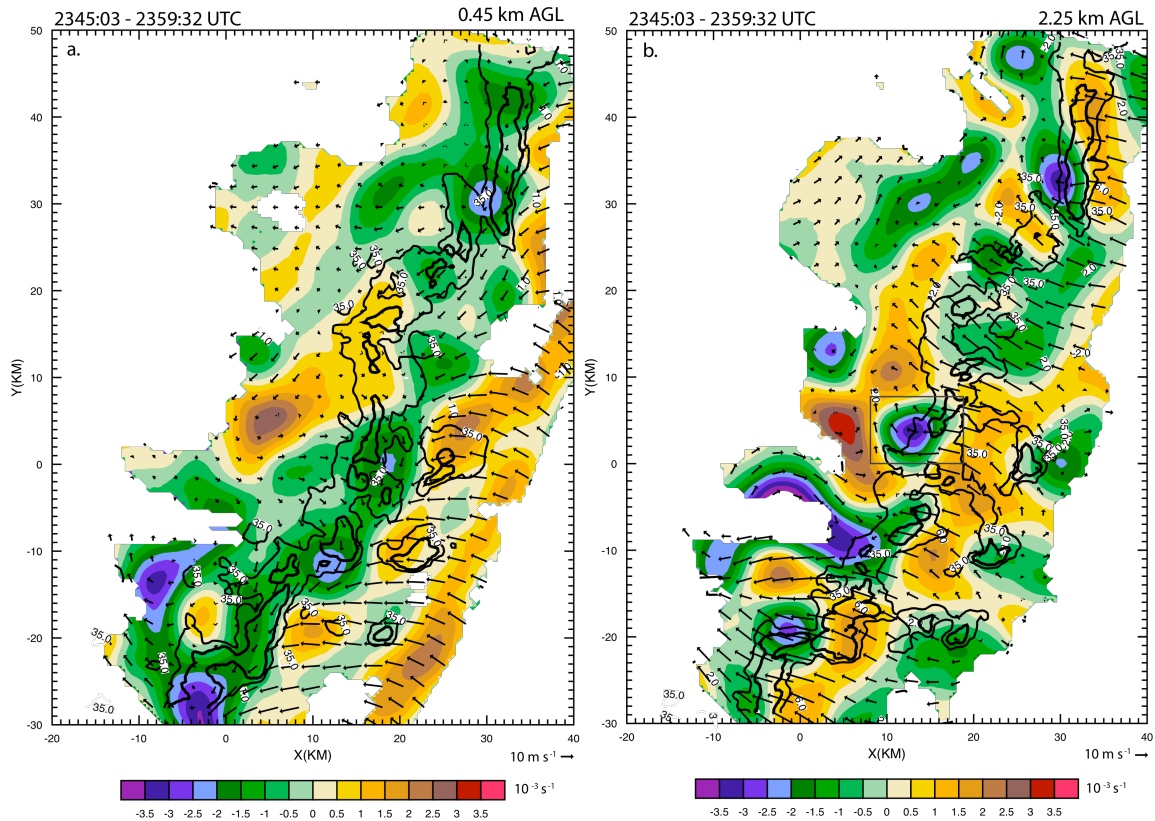


Figure 6.5: ELDORA reflectivity (dBZ), vertical velocity ( $\text{m s}^{-1}$ ), and storm-relative winds superimposed on the vertical vorticity ( $\text{s}^{-1}$ ) field at (a.) 0.45 km AGL and (b.) 2.25 km AGL. The black lines are reflectivity; the thin line is 35 dBZ, and the thick line is 45 dBZ. The grey box denotes an anticyclonic vortex, which will be referenced in the text.

maxima and minima within the cyclonic and anticyclonic bands, respectively, at 0.45 km (Fig. 6.5a). While there is evidence of the counter-rotating vortex couplet at 0.45 km, it has shifted away from the convective region, toward the stratiform region. At 2.25 km, the main feature is the counter-rotating vortex; however, there is a pronounced anticyclonic vorticity minima forming between the convective line and the cyclonic vortex (denoted by grey box in Fig. 6.5b).

In the sixth leg, at 2.25 km, there are several cyclonic and anticyclonic vortices associated with the bowed convective region (Fig. 6.6b). Ahead of the bow, there are

## Storm-relative winds and reflectivity superimposed on vertical vorticity

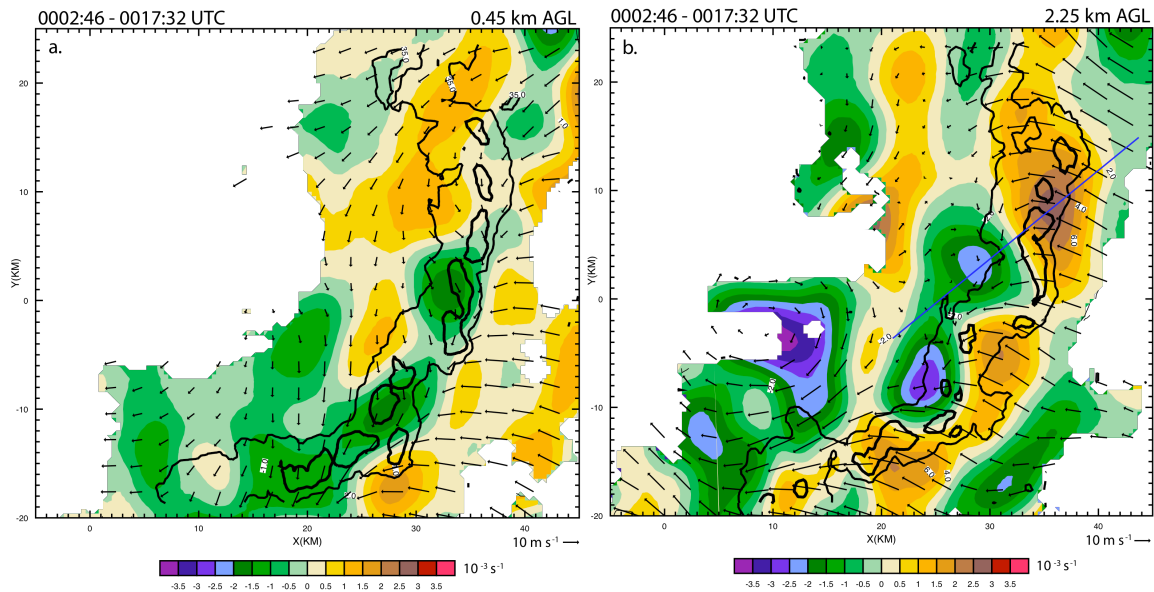


Figure 6.6: ELDORA reflectivity (dBZ), vertical velocity ( $\text{m s}^{-1}$ ), and storm-relative winds superimposed on the vertical vorticity ( $\text{s}^{-1}$ ) field at (a.) 0.45 km AGL and (b.) 2.25 km AGL. The black lines are reflectivity; the thin line is 35 dBZ, and the thick line is 45 dBZ. The blue line in (b.) denote where a cross-section was taken, which can be seen in Fig. 6.11.

two cyclonic maxima, and on the backside of the convective region there are two anticyclonic minima. The two areas are associated with small undulations in the reflectivity field within the larger-scale bowing of the convective line (denoted by grey box in Fig. 6.6b).

### 6.1.2 Vortexgenesis

In the first flight leg, the vortices along the convective line have already formed and are well-defined, most notably at 2.25 km (Fig. 6.1b). In order to investigate the processes which form and maintain the meso- $\gamma$  vortices, cross-sections were taken through a cyclonic and anticyclonic vortex pair (Fig. 6.7). As discussed in the previous chapter, the cyclonic/anticyclonic banded vorticity pattern is generated via the tilting of the

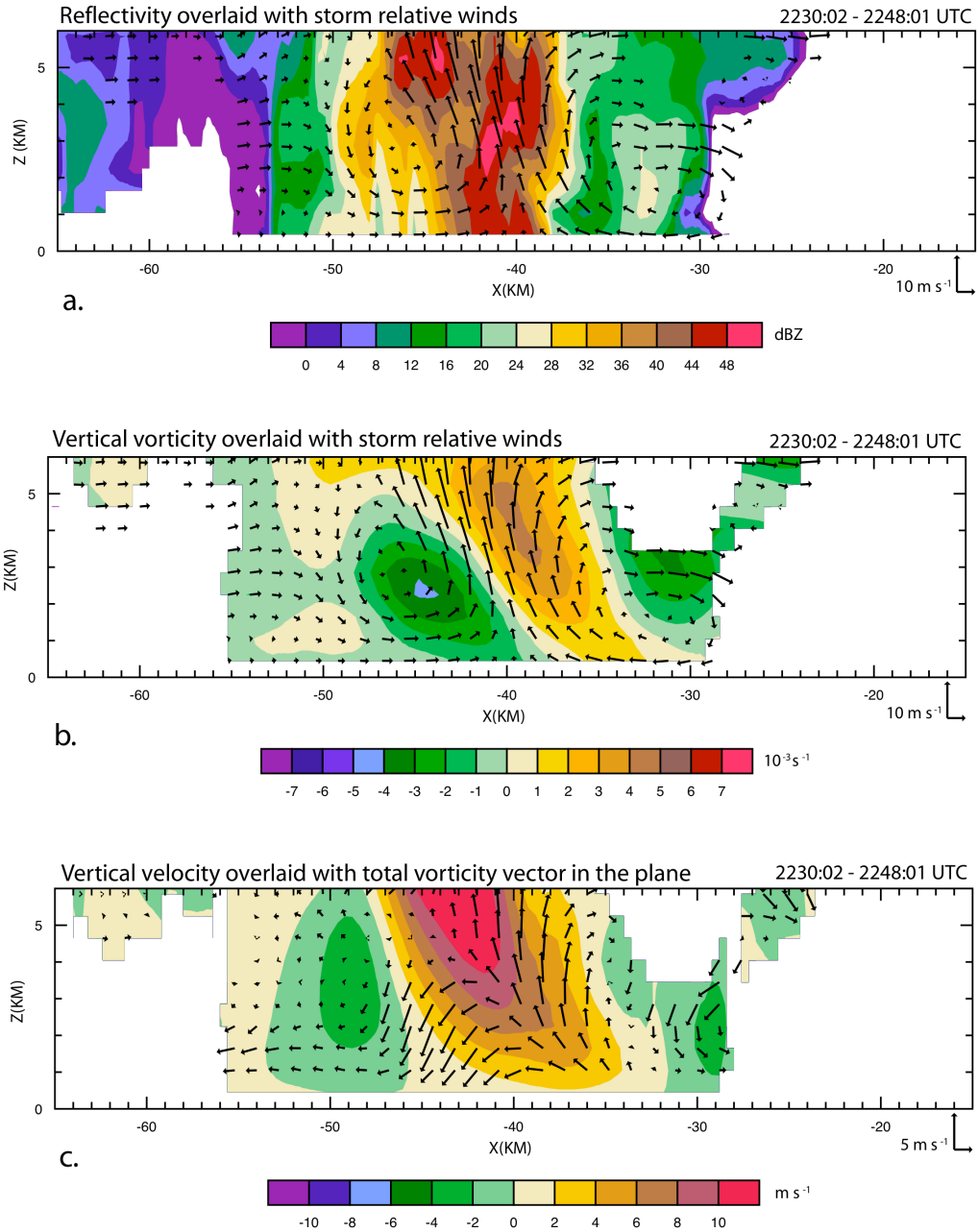


Figure 6.7: ELDORA analysis of (a.) reflectivity (dBZ), (b.) vertical vorticity ( $s^{-1}$ ), and (c.) vertical velocity ( $m s^{-1}$ ) through a pair of cyclonic and anticyclonic vortices during the first flight leg. The storm-relative wind vectors are superimposed on the reflectivity (a.) and vertical vorticity (b.) fields. The total vorticity vector in the plane of the cross-section is superimposed on the vertical velocity field (c.) The location of the cross-section is denoted by the northernmost blue line in Fig. 6.1b.

environmental horizontal vorticity into the vertical within the convective updraft. The cross-section reveals a vertical vorticity maximum and minimum for both the cyclonic and anticyclonic vortices, respectively, at mid-levels between 2 and 5 km (Fig. 6.7b). The cross-section of the vertical velocity overlaid with the vorticity vector in the plane of the cross-section exhibits upward tilting on the front edge of the updraft, which would generate cyclonic vertical vorticity (Fig. 6.7c). On the backside on the updraft where the vectors cross the negative vertical velocity gradient, there is downward tilting, which creates anticyclonic vertical vorticity. Note the bands of vertical vorticity (Fig. 6.7b) are nearly straddling the deep, convective updraft (Fig. 6.7c). The band of anticyclonic vorticity behind the convective line is located in the zone between the updraft and downdraft with an area of weak cyclonic vorticity behind the anticyclonic minimum, showing how tilting within the vertical velocity gradients can generate vertical vorticity. Horizontal maps of the vorticity budget for the first flight pass through 1.05 km and 2.25 km AGL are shown in Figs. 6.8 and 6.9, respectively. Tilting and stretching terms (Figs. 6.8b and 6.9b) were calculated, and the combined contribution from both terms was also computed (Figs. 6.8c and 6.9c). At 1.05 km, the three southernmost anticyclonic vortices are associated with negative tilting while there is a continuous strip of positive tilting ahead of the convective line (Fig. 6.8b). The stretching term at 1.05 km reveals negative stretching behind the convective line, with minima associated with several of the anticyclonic vortices (Fig. 6.8c). Similarly, there is positive stretching ahead of the convective line that is associated with the cyclonic vorticity maxima. At 2.25 km, while the negative tilting term behind the convective line is not as nearly a continuous as it was at 1.05 km, the values are similar or stronger. The positive and negative stretching term

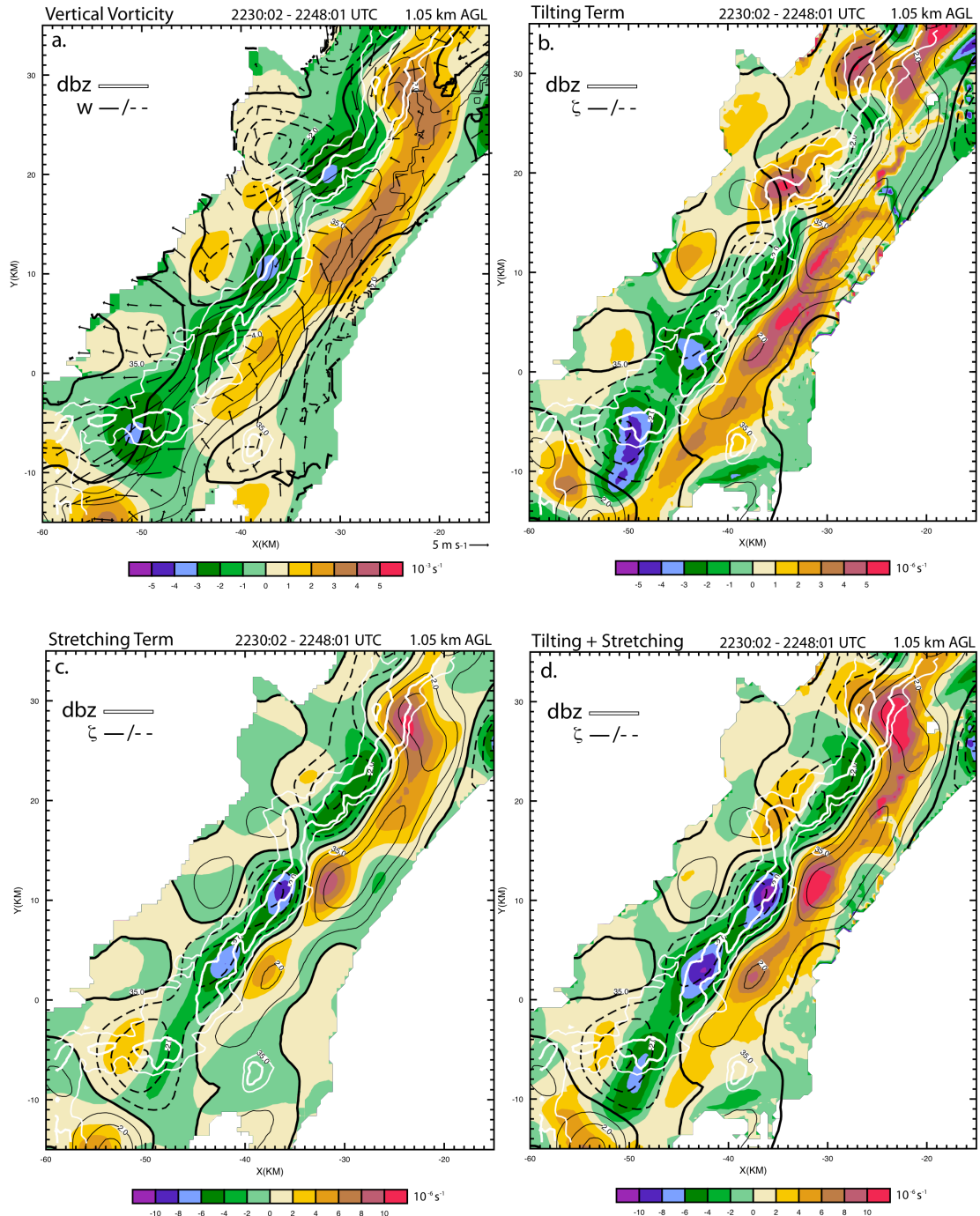


Figure 6.8: ELDORA analysis at 1.05 km AGL of (a.) vertical vorticity ( $s^{-1}$ ), (b.) the tilting term of the vertical vorticity time tendency equation ( $s^{-1}$ ), (c.) the stretching term of the vertical vorticity time tendency equation ( $s^{-1}$ ), and (d.) the combination of the tilting and stretching terms ( $s^{-1}$ ). Reflectivity (dBZ) is superimposed on all four plots; the thin line is 35 dBZ, and the thick line is 45 dBZ. In (a.) the vertical velocity ( $m s^{-1}$ ) and horizontal vorticity vectors are superimposed on the vertical vorticity. The vertical velocity is contoured every 1  $m s^{-1}$ . The vertical vorticity is superimposed on (b.), (c.), and (d.). The vertical vorticity is contoured every  $1 \times 10^{-3} s^{-1}$ .

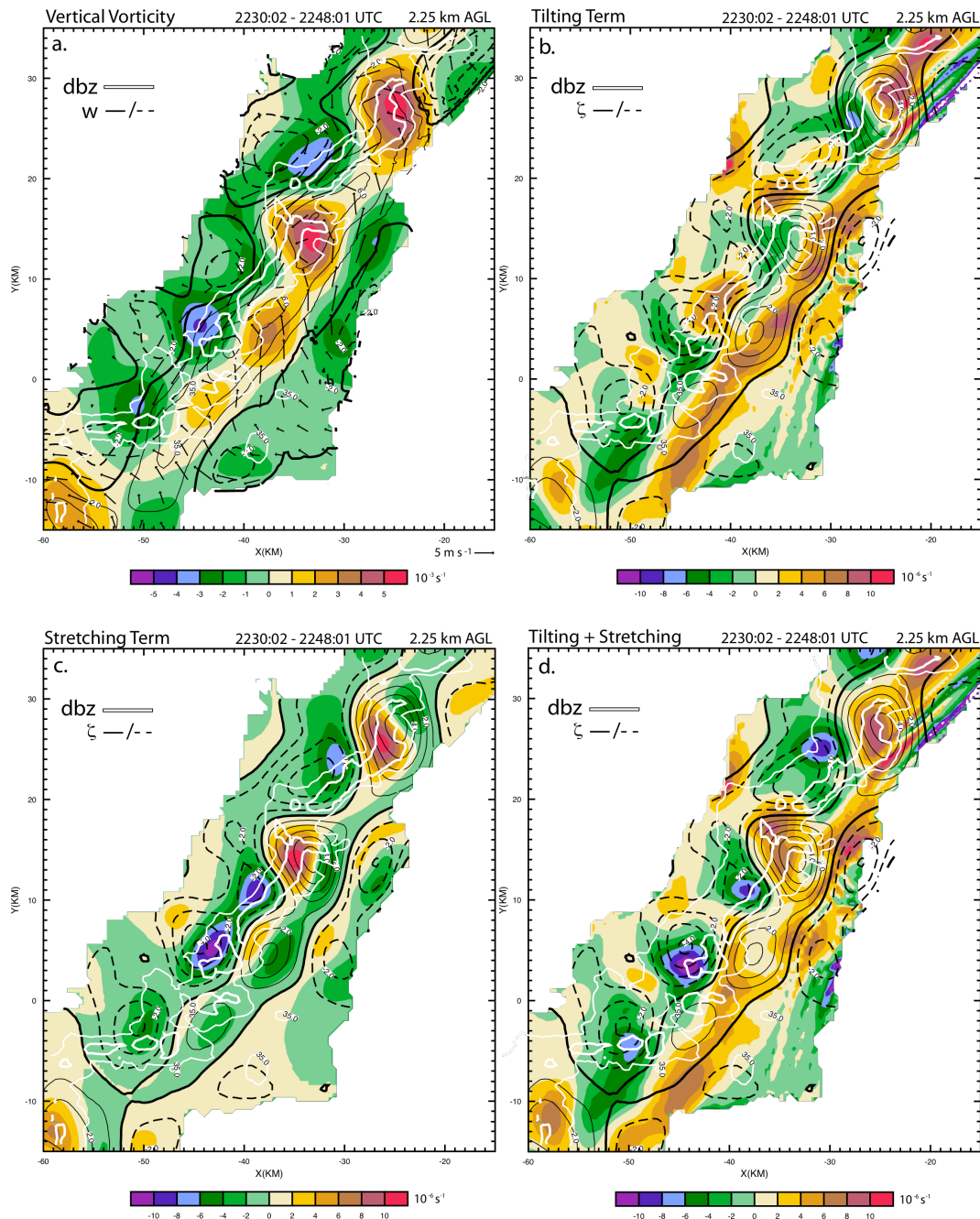


Figure 6.9: ELDORA analysis at 2.25 km AGL of (a.) vertical vorticity ( $s^{-1}$ ), (b.) the tilting term of the vertical vorticity time tendency equation ( $s^{-1}$ ), (c.) the stretching term of the vertical vorticity time tendency equation ( $s^{-1}$ ), and (d.) the combination of the tilting and stretching terms ( $s^{-1}$ ). Reflectivity (dBZ) is superimposed on all four plots; the thin line is 35 dBZ, and the thick line is 45 dBZ. In (a.) the vertical velocity ( $m s^{-1}$ ) and horizontal vorticity vectors are superimposed on the vertical vorticity. The vertical velocity is contoured every  $1 m s^{-1}$ . The vertical vorticity is superimposed on (b.), (c.), and (d.). The vertical vorticity is contoured every  $1 \times 10^{-3} s^{-1}$ .

is still nicely aligned with the cyclonic and anticyclonic vertical vorticity, respectively (Fig. 6.9b,c). These horizontal maps reveal what has been seen in vertical cross-sections. In the low-levels, there is strong positive tilting ahead of the line with more localized negative tilting behind the line. The areas of localized negative tilting are associated with vertical vorticity minima. Stretching, at both the low- and mid-levels further concentrates the vertical vorticity.

By the first flight leg, the vortex pairs are already formed and present at both low- and mid-levels. While it is clear that the tilting of the horizontal vorticity produces the vertical vorticity pattern, it would be beneficial to observe a pair of vortices forming and maturing. Fortunately, a pair of vortices begins to form along the convective line during the third flight pass, and their maturation is captured through the final flight leg. While becoming just visible in lowest 2 km, the pair of vortices is not yet clearly visible at mid-levels (Fig. 6.3a; the vortices in question are located near the blue line). Cross-sections of the vertical vorticity, vertical velocity, and the tilting term reveal what has been hypothesized (Fig. 6.10). From the lowest resolvable level to ~3.0 km there is cyclonic vorticity ahead of the convective line with anticyclonic vorticity behind the convective line with the couplet being the strongest in the lowest 1.0 km AGL (Fig. 6.10a,b). There is also positive tilting ahead of the convective line and negative tilting behind the convective line with maximum tilting occurring ~3 km (Fig. 6.10d). There is a locally strong updraft ( $>7 \text{ m s}^{-1}$ ) that is aiding in the strong tilting (Fig. 6.10c).

In the fourth leg, the pair of vortices becomes more defined at 2.25 km (denoted by grey box Fig. 6.4b), and by the fifth flight leg, the anticyclonic vortex becomes stronger and more defined in the mid-levels (Fig. 6.5b). In these two legs, vertical cross-

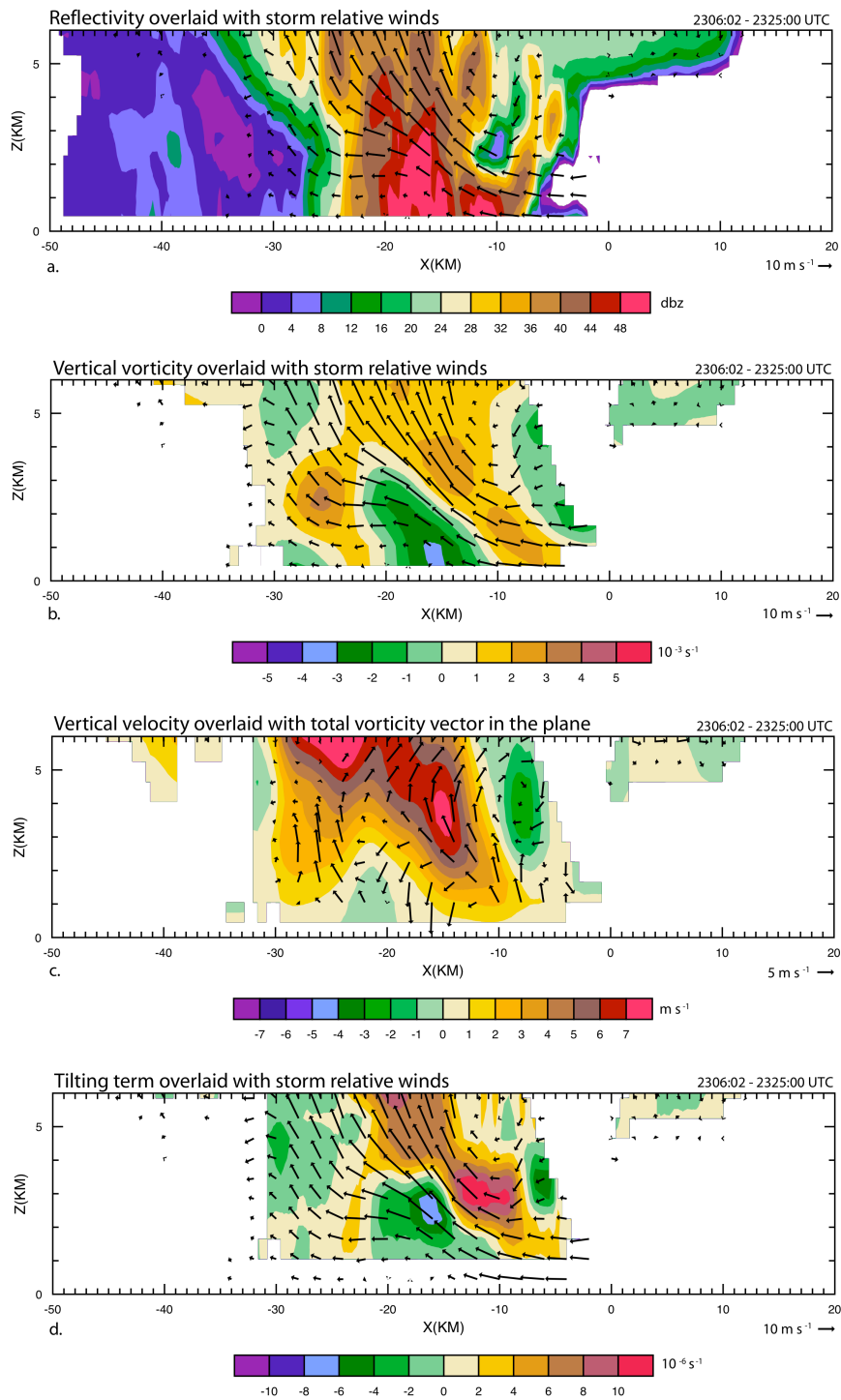


Figure 6.10: Vertical cross-section using ELDORA analysis during the third leg of (a.) reflectivity (dBZ), (b.) vertical vorticity ( $s^{-1}$ ), (c.) vertical velocity ( $m s^{-1}$ ), and (d.) the tilting term ( $s^{-1}$ ) from the vertical vorticity time tendency equation. The storm-relative wind vectors are superimposed on the reflectivity (a.), vertical vorticity (b.), and tilting term (d.). The total vorticity vector in the plane of cross-section is superimposed on the vertical velocity field (c.) The blue line in Fig. 6.3a denotes the location of the cross-section.

sections through the forming vortices reveal that as the vortices mature, they become stronger and more elevated (not shown). There is still a significant component of tilting, especially near 3 km, but the stretching term begins to contribute more as well.

In the sixth flight leg, the cyclonic/anticyclonic vortex pair becomes well defined at 2.25 km (Fig. 6.6b), and it is also associated with undulations in the reflectivity field. Vertical cross-sections through the couplet (Fig. 6.11) exhibit similar features through the mature vortex couplet in the first leg (Fig. 6.7), such as a mid-level maximum in the vertical vorticity that straddles a strong updraft (Fig. 6.11b,c). The cross-section also has a stronger and deeper downdraft than the one seen in the third leg, when the vortex pairs were in their formative stages. There is a negative tilting minimum at mid-levels, and unlike the third flight leg, there is minimal negative tilting in the lowest levels. This would suggest that strong tilting of the horizontal vorticity in the lowest levels originally forms the vortices. With time, and through stretching and tilting at mid-levels, the vortices become stronger and more elevated.

A key question to address is why some areas developed these vortex pairs and other areas did not. It has been established that, overall, there was a banded vertical vorticity pattern with cyclonic vorticity ahead of the convective line and anticyclonic vorticity associated on the backside of the convective line. As discussed above, cross-sections were taken through one of these pairs of vortices, and they revealed that strong tilting of horizontal vorticity was occurring in association with a vigorous updraft and downdraft. Another set of cross-sections was taken in an area where there was not a pair of anticyclonic and cyclonic vortices (Fig. 6.12). These cross-sections reveal that there is still a banded vorticity pattern; however, it is much weaker with the cyclonic vorticity

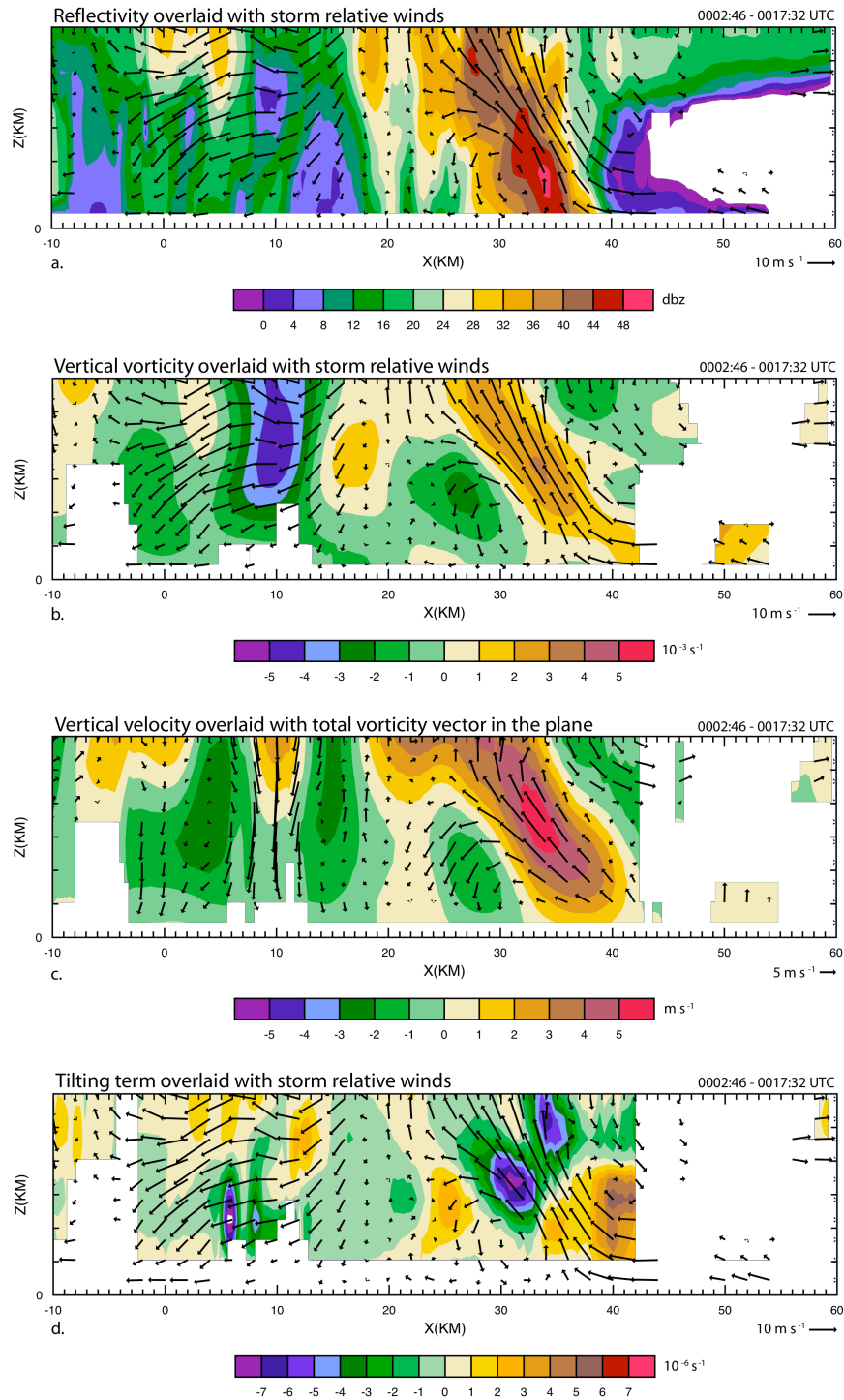


Figure 6.11: Vertical cross-section using ELDORA analysis during the sixth leg of (a.) reflectivity (dBZ), (b.) vertical vorticity ( $s^{-1}$ ), (c.) vertical velocity ( $m s^{-1}$ ), and (d.) the tilting term ( $s^{-1}$ ) from the vertical vorticity time tendency equation. The storm-relative wind vectors are superimposed on the reflectivity (a.), vertical vorticity (b.), and tilting term (d.). The total vorticity vector in the place of the cross-section is superimposed on the vertical velocity field (c.) The blue line in Fig. 6.6b denotes the location of the cross-section.

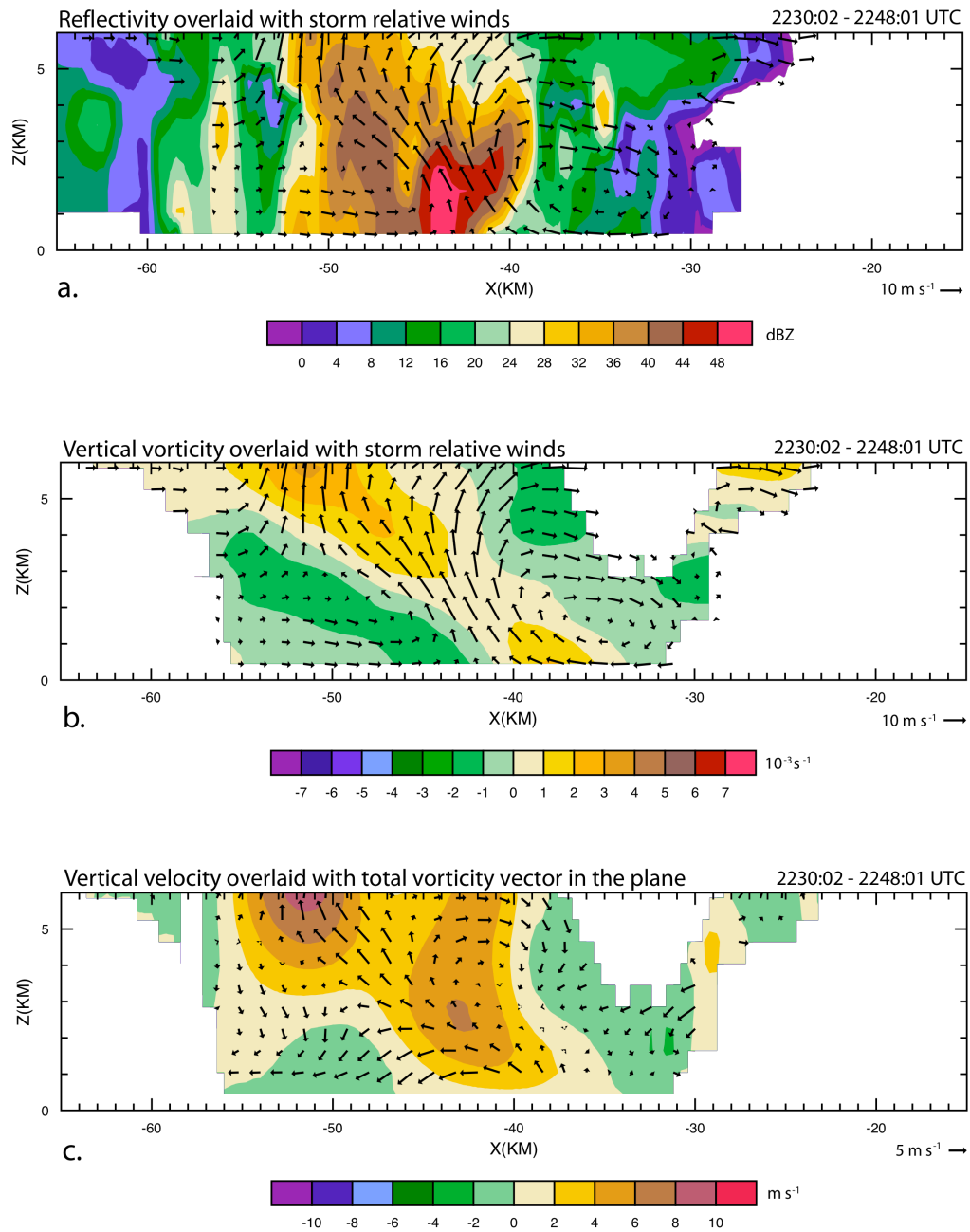


Figure 6.12: ELDORA analysis of (a.) reflectivity (dBZ), (b.) vertical vorticity ( $s^{-1}$ ), and (c.) vertical velocity ( $m s^{-1}$ ) through a pair of cyclonic and anticyclonic vortices during the first flight leg. The storm-relative wind vectors are superimposed on the reflectivity (a.) and vertical vorticity (b.) fields. The total vorticity vector in the plane of the cross-section is superimposed on the vertical velocity field (c.) The location of the cross-section is denoted by the southernmost blue line in Fig. 6.1b.

values  $\sim 0.5 - 1.5 \times 10^{-3} \text{ s}^{-1}$  and the anticyclonic vorticity values  $\sim -1.25 \times 10^{-3} \text{ s}^{-1}$ . While the banded pattern is visible, there is no concentration of vertical vorticity in the mid-levels as seen in the cross-sections through the vortex pairs, and the banded pattern is more sloped. The vertical velocity field is not as impressive, with maximum updrafts approaching  $7 \text{ m s}^{-1}$ . The downdraft is also weaker and shallower than the downdraft in conjunction with the pair of vortices. Due to the weaker vertical velocity field, the tilting of the horizontal vorticity is not as strong as the tilting associated with the vortex pairs. While it is present in the cross-section through the area of the convective line without a vortex pairing, it is not as prominent as it is through the vortex pairs. The stretching is also not as strong, causing less amplification of the vortex (not shown).

It has been established that the areas with locally vigorous updrafts are associated with the vortices along the convective line. The exact mechanism for the production of the strong updraft is difficult to pinpoint; however, there are several ideas that can be addressed. It is possible that the convective line is interacting with boundaries ahead of the storm, causing increased convergence in certain areas. Also, the outflow from the locally stronger downdrafts could accelerate faster than the outflow from the weaker downdrafts, which will cause enhanced convergence ahead of the accelerating outflow. The enhanced convergence caused by the divergent outflow will lead to locally stronger updrafts. If this mechanism were in place, it could also explain the small-scale bowed segments (10 – 20 km) that are seen in all six of the flight legs. The local acceleration of the downdraft, in conjunction with the cold pool, could cause the convective line to locally bow out. Lastly, the topography of northern Mississippi does have some undulations due to hills or forested areas. These differences in terrain could cause areas

of enhanced lift as well. Whatever the mechanism(s), areas with vigorous updrafts are often areas with enhanced tilting, which cause cyclonic vertical vorticity to be produced ahead of the upward motion while anticyclonic vertical vorticity is produced on the backside of the updraft. Results from this study show that after the horizontal vorticity is tilted into the vertical, stretching then amplifies the vertical vorticity.

## **6.2 Mid-level counter-rotating vortices**

In addition to the small-scale vortices associated with the convective line, a mid-level counter-rotating vortex also forms and matures during the six flight legs sampled by the airborne radars. During the second flight leg, the vortices show initial signs of formation, and by the end of the sixth flight leg, the counter-rotating vortices have matured and are associated with the bowing convective region. While the system is on the smaller side of the bow echo spectrum (~50 km), it still displays characteristics seen in bowing convective systems.

At the lowest-resolvable level in the second leg, the band of anticyclonic vertical vorticity is discontinuous with weak cyclonic vorticity infiltrating between areas of enhanced anticyclonic vorticity (denoted in Fig. 6.2a with a grey box). This area of cyclonic vorticity forms where there is positive tilting in the previous leg (Fig. 6.9b), indicating that the tilting in the first leg aided in the vertical vorticity pattern seen in the second leg. Additionally, approximate north-south cross-sections are taken in the second leg where the vortex couplet begins to form (Fig. 6.13). The shallow anticyclonic vorticity minima (Fig. 6.13a) are collocated with areas of strong negative stretching (Fig. 6.13b), which act to strengthen the preexisting anticyclonic vorticity minima.

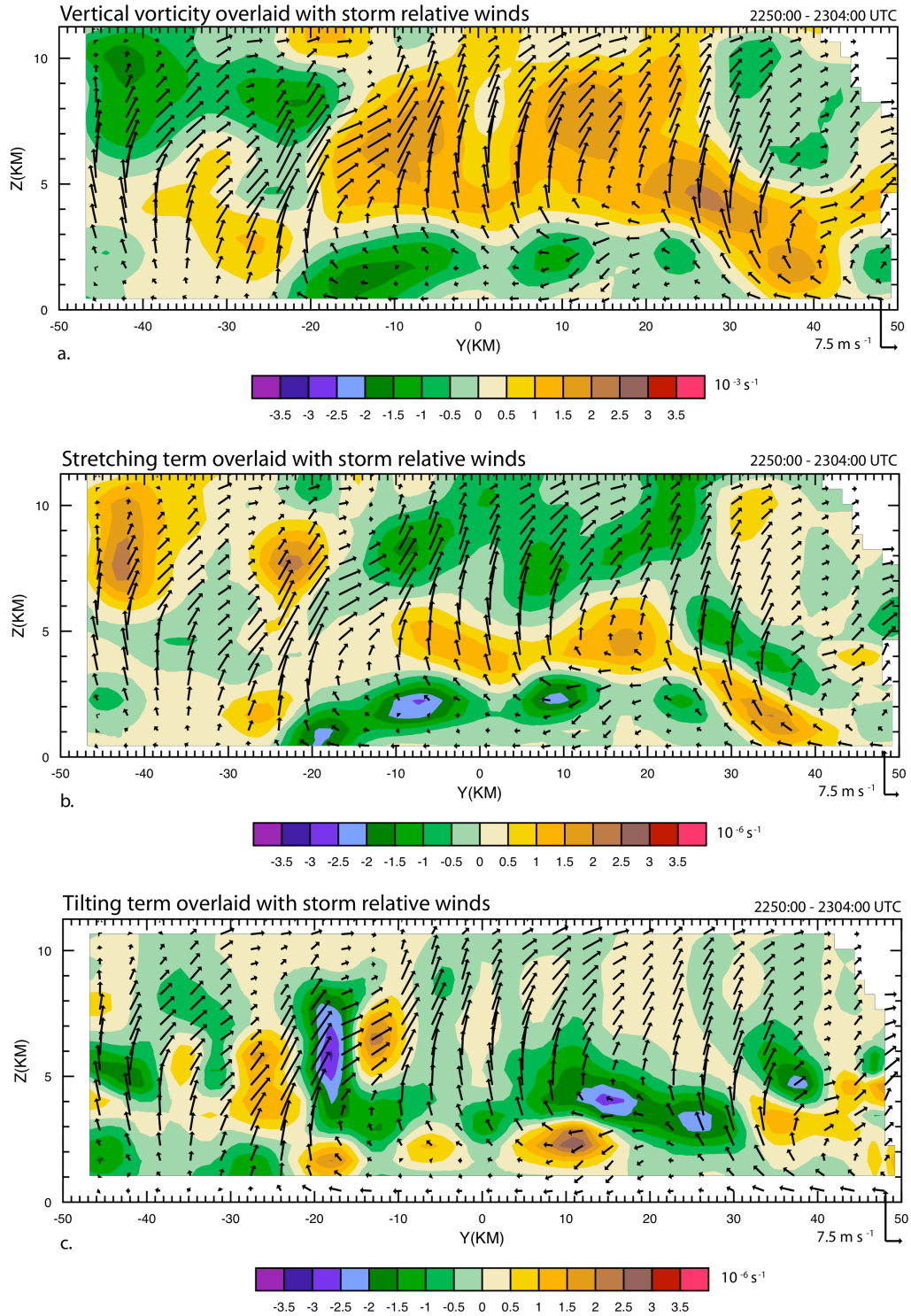


Fig. 6.13: Quad-Doppler storm-relative winds superimposed on (a.) vertical vorticity ( $s^{-1}$ ), (b.) the stretching term ( $s^{-1}$ ), and (c.) tilting term ( $s^{-1}$ ) for the second flight leg. The cross-section was taken through the axis denoted by the blue line in Fig. 6.2b.

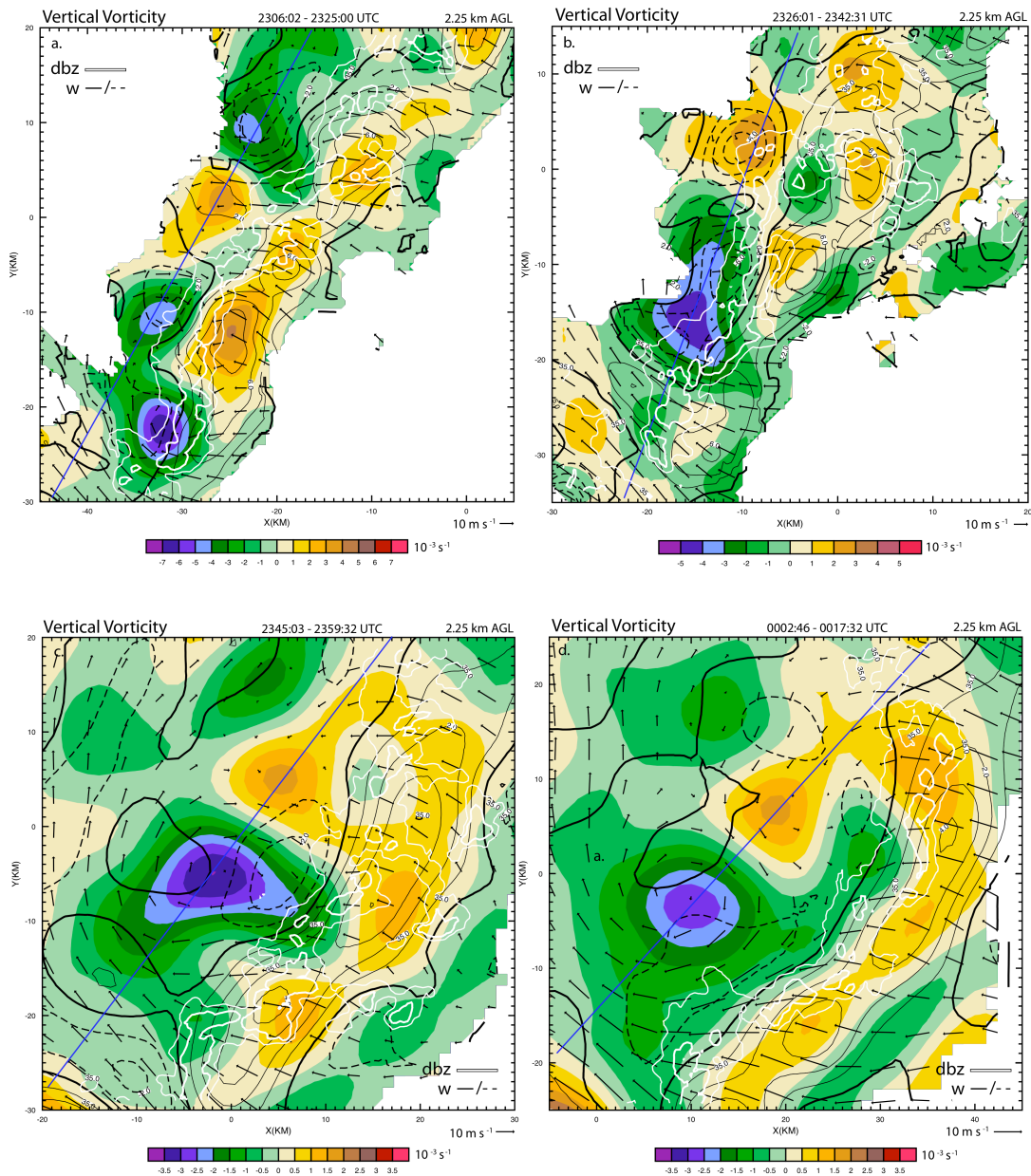


Figure 6.14: Horizontal cross-sections at 2.25 km AGL of vertical velocity ( $\text{m s}^{-1}$ ) superimposed on vertical vorticity ( $\text{s}^{-1}$ ) from (a.) 2306:02 – 2325:00 UTC, (b.) 2326:01 – 2342:31 UTC, (c.), 2345:03 – 2359:32 UTC, (d.) 0002:46 – 0017:32 UTC. Vertical velocity is contoured every  $1 \text{ m s}^{-1}$  in (a.) and (b.). In (c.) and (d.) the vertical velocity is contoured every  $2 \text{ m s}^{-1}$ . ELDORA analyses were completed in (a.) and (b.), and quad-Doppler analyses were conducted in (c.) and (d.). Blue lines indicate where vertical cross-sections are taken in Fig. 6.15b-e.

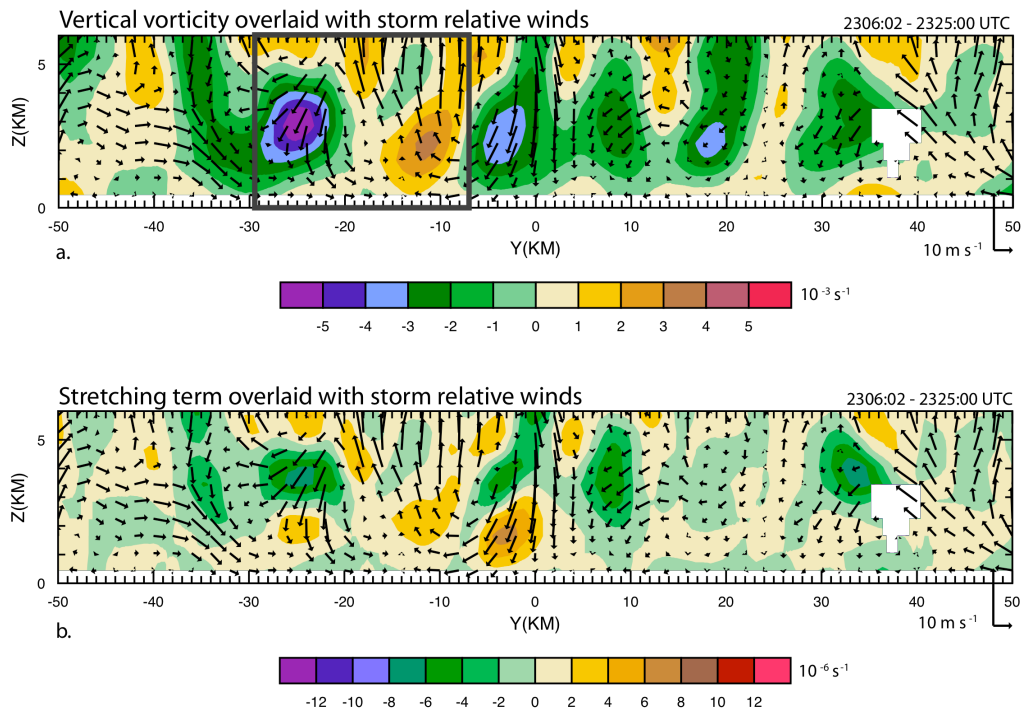


Fig. 6.15: ELDORA storm-relative winds superimposed on (a.) vertical vorticity ( $\text{s}^{-1}$ ), (b.) the stretching term ( $\text{s}^{-1}$ ), and (c.) tilting term ( $\text{s}^{-1}$ ) for the third flight leg. The cross-section was taken through the axis denoted by the blue line in Fig. 6.14a.

Interestingly, there are two areas of positive tilting in the low-levels (Fig. 6.13c), which are roughly located in between the anticyclonic minima and where there is weak cyclonic vorticity in the lowest 1 km.

In the horizontal plane, the first visual evidence of the mid-level counter-rotating vortex couplet is seen in the third leg (Fig. 6.14a). As discussed previously, there are two distinct, strong anticyclonic vortices on the southern end of the system. One is anchored to the end of the convective line and is able to interact more freely with the environment ahead of the convective line; the second anticyclonic vortex is behind the convective line, and its anticyclonic circulation is beginning to interact with the circulation from the developing cyclonic vortex to the north. The cyclonic vortex that forms behind the convective line is within the anticyclonic band, and it is the only cyclonic circulation that forms and matures behind the convective line throughout the time period sampled by the

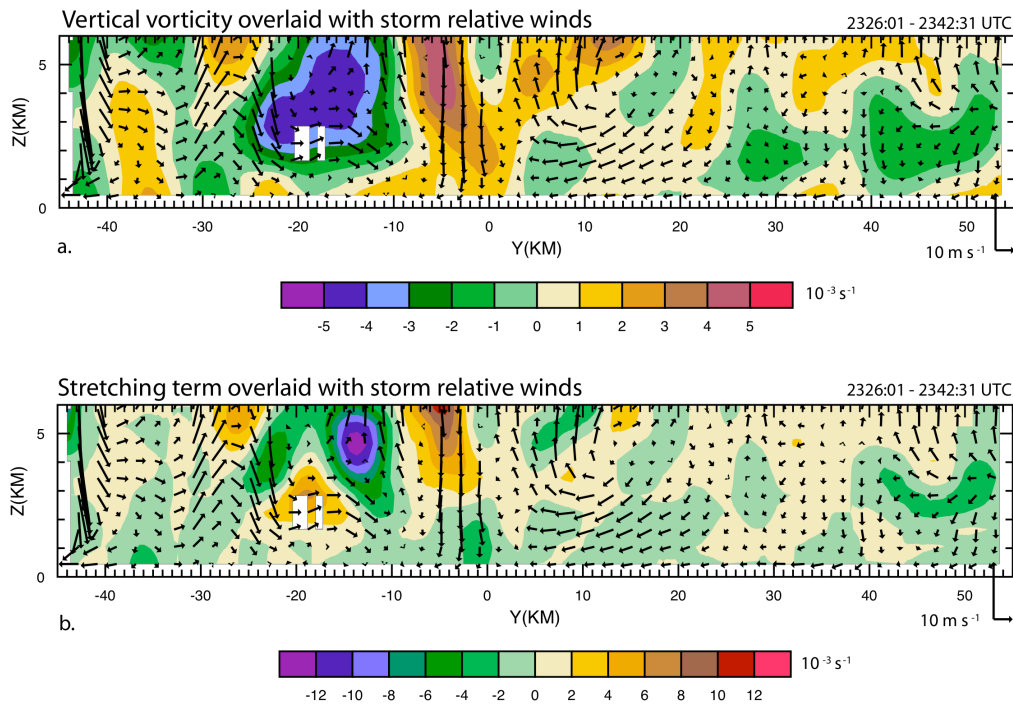


Fig. 6.16: ELDORA storm-relative winds superimposed on (a.) vertical vorticity ( $s^{-1}$ ), (b.) the stretching term ( $s^{-1}$ ), and (c.) tilting term ( $s^{-1}$ ) for the fourth flight leg. The cross-section was taken through the axis denoted by the blue line in Fig. 6.14b.

airborne radar. This cyclonic vortex develops from where there was weak cyclonic vorticity in the second leg at the lowest levels.

An approximate north-south cross-section through the developing couplet in the third leg clearly shows the developing cyclonic vortex between the two anticyclonic vortices (couplet in grey box in Fig. 6.15a). This is a marked change from the approximate north-south cross-section through the anticyclonic band during the second flight pass (Fig. 6.13a) where the band was still continuous above 1.0 km. The mentioned areas of positive tilting between the anticyclonic vorticity minima in the second flight leg aided in the generation of cyclonic vertical vorticity seen in the third leg. In addition, the stretching term is plotted and shows positive stretching in

association with the developing cyclonic vortex, while there is negative stretching above 2.5 km in association with the anticyclonic vortex (Fig. 6.15b). Curiously, there is an area of positive stretching in the lowest 3.0 km associated with the anticyclonic vortex to the north of the cyclonic vortex, which will act to diminish the that anticyclonic vortex by the fourth leg.

By the fourth leg, the developing counter-rotating vortex couplet becomes better defined, and the anticyclonic vortex that was to the north of the couplet dissipates (Fig. 6.14b). Fig. 6.16a displays an approximate north-south cross-section through the counter-rotating vortex couplet during the fourth flight pass, and compared to the cross-sections from the previous flight leg, both vortices have strengthened with the vertical vorticity maxima shifted from the low-levels to the mid-levels. Most of this strengthening is due to effects from stretching (Fig. 6.16b), with strong negative stretching collocated with the anticyclonic vortex and positive stretching collocated with the cyclonic vortex. By this leg, when considering the vorticity budget, the effects from stretching are far greater than the effects from the tilting (not shown).

In the fourth leg, the two southern anticyclonic circulations from the third leg merge, causing the anticyclonic vortex to be spatially dominant and stronger than the cyclonic vortex, which is seen in both the horizontal and the vertical profiles. The counter-rotating vortices are still anchored on the backside of the convective line, and the vortex couplet is associated with some bowing in the convective line (Fig. 6.14b).

In the fifth and sixth flight legs, the vortex couplet begins to move away from the convective line toward the stratiform region (Fig. 6.14c,d). The vortices are becoming more symmetric, and there is enhanced rear-inflow concentrated between the vortices that

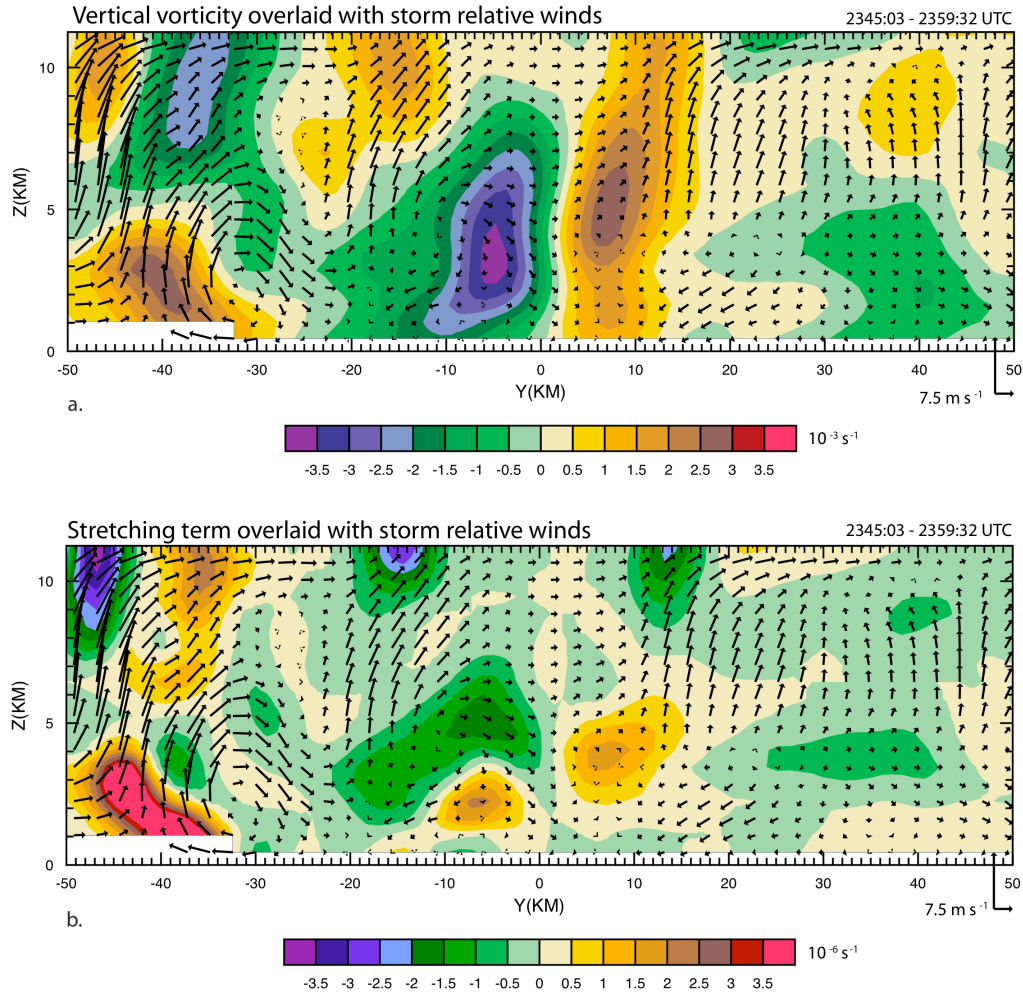


Fig. 6.17: Quad-Doppler storm-relative winds superimposed on (a.) vertical vorticity ( $\text{s}^{-1}$ ), (b.) the stretching term ( $\text{s}^{-1}$ ), and (c.) tilting term ( $\text{s}^{-1}$ ) for the fifth flight leg. The cross-section was taken through the axis denoted by the blue line in Fig. 6.14c.

extend to the convective line. While the counter-rotating vortex couplet matures, it is still obvious that even after the final flight pass, the anticyclonic vortex is still dominant.

As the couplet matures, there is pronounced bowing of the convective line (Fig. 14c,d).

While bowing is observed in the fourth leg, the most significant bowing occurs in the final two legs, which is in conjunction with the maturation of the vortex couplet as well as the enhanced counter-rotating flow between the two vortices. Consistent with typical bowed convection, the southern end of the system is dominated by anticyclonic vorticity,

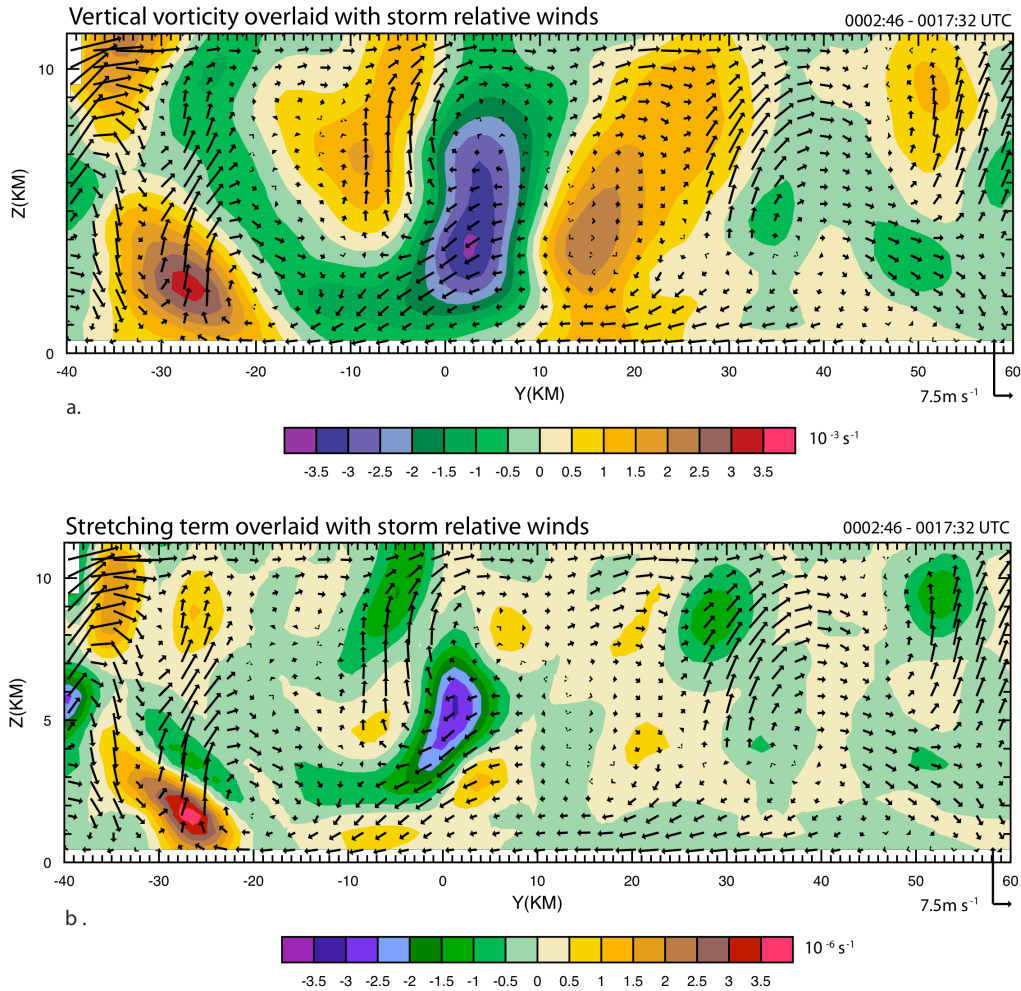


Fig. 6.18: Quad-Doppler storm-relative winds superimposed on (a.) vertical vorticity ( $\text{s}^{-1}$ ), (b.) the stretching term ( $\text{s}^{-1}$ ), and (c.) tilting term ( $\text{s}^{-1}$ ) for the sixth flight leg. The cross-section was taken through the axis denoted by the blue line in Fig. 6.14d.

while there is cyclonic vorticity in the northern end of the storm. Interestingly, as the couplet moves rearward to the stratiform region, the cyclonic/anticyclonic banded structure associated with the convective line begins to reestablish itself.

Approximate north-south cross-sections in the fifth and sixth leg show the vertical extent of the cyclonic and anticyclonic vortices; whereas the vortex couplet was initially contained to the low-levels, by the later flight legs, evidence of the couplet extends to the upper-levels, with a maximum in the mid-levels (Figs. 6.17a and 6.18a). The stretching

term in the fifth flight leg agrees with the strengthening seen in the mid-levels (Fig. 6.17b). There are positive and negative stretching maximums and minimums, respectively, in the mid-levels, which relate well to the strengthening observed in the mid-levels. Curiously, when observing the stretching term in the sixth flight leg, there is a strong stretching term in the mid-levels associated with the anticyclonic vortex, but there is not a coherent stretching pattern seen in conjunction with the cyclonic vortex (Fig. 6.18b). Unfortunately, the sixth leg was the final flight leg, so it is impossible to see how this affected the vortex couplet.

After analysis when the cyclonic and anticyclonic vortices that later became the counter-rotating vortex couplet were beginning to form in the first two legs, it was the tilting of the horizontal vorticity that generated the vorticity maximums and minimums. However, after the vortices were formed, in the following legs (3 – 6), it was the stretching that lead to the significant strengthening of the vortex couplet. As the couplet matured and migrated away from the convective line toward the stratiform region, it was maintained by system-generated processes.

### **6.3 Discussion**

There have been several modeling and observational studies which discuss low- and mid-level vortices (e.g. Weisman and Davis 1998; Trapp and Weisman 2003; Wakimoto et al. 2006; Wheatley and Trapp 2008). An overwhelming majority of studies regarding vortices within MCSs occur in environments where the environmental shear vector is perpendicular to the convective line; however, the 2-3 June 2003 MCS occurred in an environment which contained an along-line shear component. This environment contributed to the observed cyclonic/anticyclonic banded vorticity structure, which has

several similarities to the vertical vorticity patterns observed in Zhang et al. (1989), BH91, Zhang (1992). In addition to the banded vorticity pattern, the 2-3 June 2003 MCS produced vortices at low- and mid-levels.

The 2-3 June 2003 MCS contains mesovortices 5-15 km in horizontal scale in proximity to the convective line as well as a mid-level counter-rotating vortex couplet (~40 km horizontal scale) that forms behind the convective line and is associated with the bowing convection at the end of the sampling period. While mesovortices and counter-rotating vortex couplets have been documented in previous studies, the mechanisms, environment, and scale in which these vorticity patterns makes the 2-3 June 2003 MCS unique.

Weisman and Davis (1998; hereafter, WD98) simulated mesoscale vortices with differing environmental shear profiles ( $10 \text{ m s}^{-1}$  over lowest 2.5 km,  $20 \text{ m s}^{-1}$  over lowest 2.5 km, and  $30 \text{ m s}^{-1}$  over lowest 5.0 km), but the overall shear vector was always perpendicular to the convective line. The actual environment of the 2-3 June 2003 MCS was similar to the weak shear simulation in the WD98 study, but the resultant reflectivity and vorticity fields more closely resembled the moderate and strong shear simulations.

WD98 propose two mechanisms for vortex formation. System-scale vortices (similar scale to what this study refers to as the mid-level, counter-rotating vortex couplet) in their simulations are produced by the localized upward tilting of system-generated horizontal vorticity. While WD98 produced system-scale vortices for all three shear profiles, they noted that the weaker shear, the further behind the line the vortex production occurred. This study exhibited what WD98 would classify as weak shear; however, the vortex production occurred almost directly behind the convective line. As

the counter-rotating vortex couplet matured, it migrated away from the convective line and towards the stratiform region as stretching amplified the vortices. This finding agrees with the modeling simulations seen in Skamarock et al. (1994), where the a convective line in weak, westerly shear ( $10 \text{ m s}^{-1}$  over lowest 2.5 km) produced cyclonic and anticyclonic vortices on the northern and southern ends, respectively, of the convective line. The vortices in Skamarock et al. (1994a.) were of similar scale to this study (40 – 60 km), and they were located within the stratiform region of the convective system. In simulations including the Coriolis force, the counter-rotating vortices seen in the Skamarock et al. (1994) and WD98 studies became asymmetric with time (i.e. the cyclonic vortex became dominant). While it is important to note that this current study was not able to monitor the entire lifetime of the counter-rotating vortex couplet, there were no signs of the cyclonic vortex becoming dominant. In fact, throughout the entire lifetime of the couplet, as seen by the airborne radars, the anticyclonic vortex was dominant vortex.

Small-scale bowed convective segments of similar size (10 – 20 km) were also observed in both this study and the WD98 study. WD98 discovered that the small-scale segments were associated with small-scale counter-rotating vortices, which they refer to as subsystem vortices. These subsystem-scale vortices were produced in the strong, deep shear simulations, and were rarely seen in the shallow, weak shear simulations. Their simulations show that the small-scale bowed convective segments are associated with updraft-downdraft couplets, similar to supercells. They propose that the environmental horizontal vorticity is tilted by these updraft-downdraft couplets causing the subsystem-scale vortices to form close in association with the updraft-downdraft couplet. WD98

reason these features may prefer being located on the line-ends as to increase interaction with the environmental shear and have less interaction with the system-processes; however, they do note that the subsystem-scale vortices are observed throughout the line, especially at earlier times in the simulations, which was observed in this study from the first to third flight leg.

The environment on 2-3 June 2003 was not one in which supercells or rotating updraft was expected; yet, the small-scale convective segments and the subsystem-scale vortices are observed. The general mechanism for vortex formation in the two studies is similar, however. In the first flight leg, when there are several pairs of small-scale vortices, there are also locally intense updrafts that are closely located to the small-scale vortex pairs. It is hypothesized that the locally intense updraft causes strong tilting of the environmental horizontal vorticity. While the WD98 study attributes their observed reflectivity and vorticity patterns to the supercellular feature induced by the deeper, strong shear, this study attributes the features the cyclonic/anticyclonic banded vorticity pattern and the local acceleration of the downdraft induced outflow.

It is also important to discuss the vortex pairs seen at the low-levels. Several studies have debated the genesis mechanisms of low-level vortices; yet, there are still several disagreement regarding this topic. Some studies assert low-level mesovortex genesis to the tilting of horizontal vorticity in the rainy, convective downdraft (e.g. Trapp and Weisman 2003; Wheatley and Trapp 2008). The tilting of the vortex lines near the gust front creates an anticyclonic vortex to the north and a cyclonic vortex to the south. Wakimoto et al. (2006b) argues that the downdrafts associated with the gust front are not producing rain at the earlier stages of vortex formation and proposes the mechanically

forced downdraft ahead of the convective line tilts the horizontal baroclinic vorticity. The tilting produces a vortex couplet with the anticyclonic circulation to the north and the cyclonic circulation to the south. Atkins and St. Laurent (2009b) develop mechanisms of low-level vortex genesis that create a cyclonic vortex to the north and an anticyclonic vortex to the south, especially in the early stages of bow echo formation. They propose that vortex lines oriented from north to south along and behind the gust front (associated with what?) are tilted upward by locally strong updrafts, which would create the cyclonic and anticyclonic vertical vorticity on the northern and southern sides, respectively, of the updraft. Also, while previous studies have shown that anticyclonic vortices form in the low-levels, they are normally not as strong or do not survive as long as the cyclonic vortices. While the general vortex formation and environment is different from the previous studies of low-level mesovortices, it is still important to note not only the number of anticyclonic vortices present in this study but also their strength and longevity.

The counter-rotating vortex couplet in the 2-3 June 2003 MCS forms directly behind the convective line and then moves toward the stratiform region as it matures. While the anticyclonic band of vorticity becomes disjoint during the formation of the cyclonic vortex, the cyclonic/anticyclonic vorticity bands begin to reorganize as the counter-rotating vortex begins migrating away from the convective line. During the final flight leg, both the cyclonic/anticyclonic banded vorticity bands as well as the counter-rotating vortices are present in the vorticity field. Tilting of the system-generated horizontal vorticity produced the vortex couplet, while tilting of the environmental horizontal vorticity produces the both the banded vorticity pattern and the small-scale

vortices within the bands. This exact vertical vorticity structure has yet to be discussed in the literature.

## Chapter 7

### CONCLUSIONS

#### 7.1 Summary of results

On 2-3 June 2003, an MCS traversed over northern Mississippi and was heavily sampled using ground-based and airborne platforms due to its occurrence during BAMEX. A detailed analysis of the three-dimensional wind field was executed using high-resolution radar data collected with ELDORA, which was mounted on the NRL P-3, and the NOAA P-3 radars. Dual-Doppler analysis was performed on all of the six flight legs, and due to coordination efforts between the NRL P-3 and the NOAA P-3, quad-Doppler analysis was completed on three of the six flight legs. Ground-based platforms such as mobile rawinsondes, WSR-88Ds, and wind profilers were also used to enhance the overall understanding of the environment in which the 2-3 June 2003 MCS was occurring. Through the combination of these highly mobile ground-based and airborne platforms, a thorough analysis of the MCS was conducted.

The 2-3 June 2003 MCS was associated with a low pressure system moving eastward through Oklahoma into Missouri. Atmospheric soundings in the nearby vicinity of the convection revealed ample instability to promote strong convection; however, the weak-to-moderate unidirectional vertical wind shear did not suggest the potential for

supercells or severe, bowing convection. Both the mobile rawinsonde data and the wind profiler data indicated similar environment wind profiles: there was a significant component of along-line wind shear in the region where the 2-3 June MCS would form and traverse.

Initially, the MCS was investigated to better understand the observed small-scale (10-15 km) bowing convective segments that were seen throughout the portion of the lifecycle that was observed by the airborne radars. While the convective line was initially linear with the small-scale convective segments embedded within it, it transitioned to a bow echo ~40 km long by the final leg. After performing a complete analysis of the wind field, it became obvious that there were several striking features within the vorticity field at both low- and mid-levels. While most MCSs feature a dominant cyclonic vortex in the northern end of the squall line with a weaker anticyclonic vortex on the southern end of the line (e.g. Fujita 197; Houze et al. 1989; Davis and Weisman 1994), the 2-3 June 2003 MCS contained a cyclonic and anticyclonic banded vorticity pattern. There was a band of strong cyclonic vertical vorticity ahead of the convective line with a band of anticyclonic that was parallel to the cyclonic band and just behind the convective line. Small-scale (5-15 km) vortices were often observed within the cyclonic and anticyclonic bands. In addition to this distinct, banded vorticity structure, a pair of counter-rotating vortices formed in conjunction with a larger-scale bowed convective feature later in the sampling period.

It is concluded that the along-line wind shear component played a significant role in producing the banded vorticity pattern. Ahead of the convective line, the horizontal vorticity vectors were aligned with a component normal to the line such that when the

vortex lines encountered the convective updraft, there was strong upward tilting ahead of the updraft and downward tilting on the backside of the updraft. This resulted in a band of cyclonic vertical vorticity ahead of the convective line with an anticyclonic band of vertical vorticity behind the convective line. It is shown that the effects of stretching then amplified these bands. A conceptual model exhibiting the vertical vorticity generation via horizontal vortex tilting in an along-line wind shear environment can be seen in Fig. 7.1. Only one other squall line in the published literature has exhibited a parallel, banded vertical vorticity pattern similar to the 2-3 June 2003 MCS. BH91 use observational data to investigate the banded vorticity pattern within the stratiform, while Zhang et al. (1989) and Zhang (1992) were able to simulate. Both BH91 and Zhang (1992) showed similar mechanisms to vertical vorticity generation in the convective and stratiform regions as the study of the 2-3 June 2003 MCS.

The small-scale vortices that were observed embedded within this band were often near areas with locally strong updrafts. The mechanism(s) for these updrafts are yet unknown; however, they may be a consequence of one or more of a variety of factors: intersection of the convective line with boundaries in advance of the storm, topographic effects (despite the minor topography in the Mississippi region), or locally enhanced downdrafts. By whatever mechanism, locally strong accelerations then cause enhanced lift in certain areas, producing the strong updrafts. Areas with strong updrafts are often areas with more intense tilting, which cause cyclonic vertical vorticity to be produced ahead of the upward motion while anticyclonic vertical vorticity is produced on the backside of the updraft. This mechanism can explain why the cyclonic and anticyclonic vortices were often observed together while straddling a strong updraft. In addition,

## Conceptual model of vertical vorticity and vortex tilting in a system with along-line shear

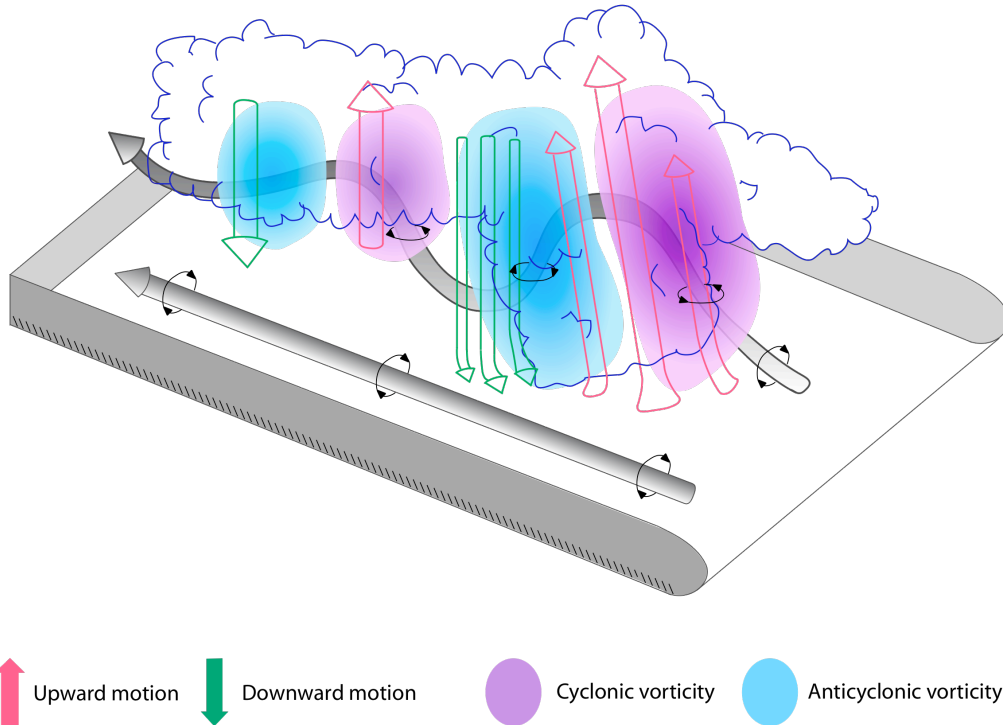


Figure 7.1: Conceptual model of a vertical vorticity generation via horizontal vortex tilting in a system with along-line wind shear. The MCS with trailing stratiform is denoted by the blue outlined area. The shaded tubes represent the horizontal vortex lines, and the rotation associated with the tubes is shown with black arrows. Upward (downward) motion is denoted by pink (green) arrows. Areas of cyclonic (anticyclonic) vertical vorticity is denoted by purple (blue).

these cyclonic and anticyclonic vortices were often associated with enhanced rear-flow, and small-scale bowing in the reflectivity field.

In addition the banded vorticity pattern, a mid-level vortex couplet formed and was associated with the bowing convection. This counter-rotating vortex couplet forms directly behind the convective line and then moves rearward toward the stratiform region with time. In the beginning legs, upward tilting of the horizontal vorticity generates the

vertical vorticity; however the growth and strengthening is attributed to the stretching. The vortex couplet grows and strengthens throughout the sampling period, but it is important to note the anticyclonic vortex is always observed to be more dominant than the cyclonic vortex.

## **7.2 Suggested future work**

The goal of this research is to document and understand distinct features that were associated with the 2-3 June 2003 MCS (e.g. small-scale bowing segments, small-scale vortices, and the banded vorticity pattern). While a thorough analysis was completed and many of the initial uncertainties were answered, there are still several questions remaining.

This study only examined one MCS, and while it displayed several interesting features, it would be beneficial to review MCSs that form in similar environments to see if the distinct features are robust. BAMEX did sample several MCSs with airborne Doppler radar that formed with a component of along-line wind shear, had radar signatures similar to the asymmetric trailing stratiform type or parallel stratiform type, and/or displayed small-scale bowing. It would be beneficial to investigate a larger sample of the MCSs in BAMEX which contained similar characteristics to the 2-3 June 2003 MCS. If it was determined that along-line wind shear often contributed to a banded-vorticity pattern, it would be important to establish how large of a component is needed to cause the shift from the dominant cyclonic vortex with a weaker anticyclonic vortex that is typical of bowed convective lines to the banded pattern. Also, it would be worthwhile to investigate whether small-scale vortices formed within the bands and if

these vortices were associated with small-scale bowing and/or damaging winds at the surface. Further investigating small-scale bowing and its associated wind and vorticity fields should also be considered as small-scale bowing has been observed in both line-parallel and line-perpendicular environments.

Furthermore, it would be valuable to use computer models to simulate the 2-3 June 2003 MCS as well as MCSs that form in similar environments. Since the environment is dissimilar to most other types of convective that have been simulated in the past, it would be beneficial to discover if simulations produced not only the banded vorticity pattern but also the small-scale vortices which occur along the convective line. Modeling studies have been completed in studying convection with along-line wind shear (Parker 2007a,b); however, they are just beginning to receive attention in the literature, and the current, published studies do not focus on the vorticity fields and distribution within the MCS. Through the combination of high-resolution observational data and computer model simulations, more light would hopefully be shed on vorticity patterns that are associated with a component of along-line wind shear.

## REFERENCES

- Atkins, N. T., and M. St. Laurent, 2009: Bow echo mesovortices. Part I: Processes that influence their damaging potential. *Mon. Wea. Rev.*, **137**, 1497–1513.
- Atkins, N.T. and M. St. Laurent, 2009: Bow Echo Mesovortices. Part II: Their genesis. *Mon. Wea. Rev.*, **137**, 1514–1532.
- Bargen, D.W. and R.C. Brown, 1980: Interactive radar velocity unfolding. Preprints, *19<sup>th</sup> Conf. on Radar Meteorology*, Miami Beach, FL, Amer. Meteor. Soc., 278–285.
- Biggerstaff, M.I. and R.A. Houze Jr., 1991: Midlevel vorticity structure of the 10–11 June 1985 squall line. *Mon. Wea. Rev.*, **119**, 3066–3079.
- Bosart, B.L., W.-C. Lee, and R.M. Wakimoto, 2002: Procedures to improve the accuracy of airborne Doppler radar data. *J. Atmos. Oceanic, Technol.*, **19**, 322–339.
- Byers, H.R. and R.B. Braham, 1949: *The Thunderstorm*. U.S. Govt. Printing Office, Washington, D.C.
- Chong, M., and C. Campos, 1996: Extended Overdetermined Dual-Doppler Formalism in Synthesizing Airborne Doppler Radar Data. *J. Atmos. Oceanic, Technol.*, **13**, 581–597.
- Coniglio, M. C., D. J. Stensrud, and M. B. Richman, 2004: An observational study of derecho-producing convective storms. *Wea. Forecasting*, **19**, 320–337.
- Cressman, G.P., 1959: An operational objective analysis system. *Mon. Wea. Rev.*, **8**, 367–374.
- Davis, C.A. and M. L. Weisman, 1994: Balanced dynamics of mesoscale vortices produced in simulated convective systems. *J. Atmos. Sci.*, **51**, 2005–2030.
- Davis, C. and Coauthors, 2004: The Bow Echo and MCV Experiment (BAMEX): Observations and opportunities. *Bull. Amer. Meteor. Soc.*, **85**, 1075–1093.

DeWald, V. L., and T. W. Funk, 2000: WSR-88D reflectivity and velocity trends of a damaging squall line event on 20 April 1996 over south-central Indiana and central Kentucky. Preprints, *20th Conf. on Severe Local Storms*, Orlando, FL, Amer. Meteor. Soc., 177–180.

Evans, J. S., and C. A. Doswell III, 2001: Examination of derecho environments using proximity soundings. *Wea. Forecasting*, **16**, 329–342.

Frush, C.L. P.H. Hildebrand, and C. Walther, 1985: The NCAR airborne Doppler radar, Part II: System design considerations. Preprints, *23<sup>rd</sup> Radar Meteorology Conf.*, Snowmass, CO, Amer. Meteor. Soc., 151–154.

Fujita, T., 1955: Results of detailed synoptic studies of squall lines. *Tellus*, **7**, 405–436.

Fujita, T., 1959: Study of mesosystems associated with stationary radar echoes. *J. Atmos. Sci.*, **16**, 38–52.

Fujita, T. T., 1978: Manual of downburst identification for project Nimrod. Satellite and Mesometeorology Research Paper 156, Dept. of Geophysical Sciences, University of Chicago, 104 pp.

Fujita, T., and R. M. Wakimoto, 1981: Five scales of airflow associated with a series of downbursts of 16 July 1980. *Mon. Wea. Rev.*, **109**, 1438–1456.

Hamilton, R.E., 1970: Use of detailed intensity radar data in mesoscale surface analysis of the 4 July 1969 storm in Ohio. Preprints, *14<sup>th</sup> Conf. on Radar Meteorology*, Tucson, AZ, Amer. Meteor. Soc., 339–342.

Hildebrand, P. H., and C. K. Mueller, 1985: Evaluation of meteorological airborne radar. Part 1: Dual-Doppler analyses of air motions. *J. Atmos. Oceanic Technol.*, **2**, 362–380.

Hilgendorf, E.R., and R.H. Johnson, 1998: A study of the evolution of mesoscale convective systems using WSR-88D data. *Wea. and Forecasting.*, **13**, 437–452.

Houze, R.A., Jr., S. A. Rutledge, M. I. Biggerstaff, and B. F. Smull, 1989: Interpretation of Doppler weather radar displays of midlatitude mesoscale convective systems. *Bull. Amer. Meteor. Soc.*, **70**, 608–619.

Houze, R.A., Jr., B. F. Smull, and P. Dodge, 1990: Mesoscale organization of springtime rainstorms in Oklahoma. *Mon. Wea. Rev.*, **118**, 613–654.

Hoxit, L.R., C. F. Chappell, and J. M. Fritsch, 1976: Formation of mesolows or pressure troughs in advance of cumulonimbus clouds. *Mon. Wea. Rev.*, **104**, 1419–1428.

- James, R.P., J.M. Fritsch, and P.M. Markowski, 2005: Environmental distinctions between cellular and slabular convective lines. *Mon. Wea. Rev.*, **133**, 2669-2691.
- Johns, R.H., and W.D. Hirt, 1987: Derechos: Widespread convectively induced windstorms. *Wea. Forecasting*, **2**, 39-49.
- Johnson, R.H., and P.J. Hamilton, 1988: The relationship of surface pressure features to the precipitation and airflow structure of an intense midlatitude squall line. *Mon. Wea. Rev.*, **116**, 1444-1473.
- Jorgensen, D.P., P.H. Hildebrand, and C.L. Frush, 1983: Feasibility test of an airborne pulse-Doppler meteorological radar. *J. Climate Appl. Meteor.*, **22**, 744-757.
- Jorgensen, D.P. and B.F. Smull, 1993: Mesovortex circulations seen by airborne Doppler radar within a bow-echo mesoscale convective system. *Bull. Amer. Meteor. Soc.*, **74**, 2146-2157.
- Jorgensen, D.P., T. Matejka, and J.D. DuGranrut, 1996: Multi-beam techniques for deriving wind fields from airborne Doppler radars. *J. Meteor. Atmos. Phys.*, **59**, 83-104.
- Klimowski, B. A., R. Przybylinski, G. Schmocker, and M. R. Hjelmfelt, 2000: Observations of the formation and early evolution of bow echoes. Preprints, 20th Conf. on Severe Local Storms, Orlando, FL, Amer. Meteor. Soc., 44-47.
- Klimowski, B.A., M. R. Hjelmfelt, and M. J. Bunker, 2004: Radar observations of the early evolution of bow echoes. *Wea. Forecasting*, **19**, 727-734.
- Lee, W.-C., R.M. Wakimoto, R.E. Carbone, 1992: The evolution and structure of a "bow-echo-microburst" event. Part II: The bow echo. *Mon. Wea. Rev.*, **120**, 2211-2225.
- Leise, J.A., 1982: A multidimensional scale-telescoped filter and data extension package. NOAA Tech. Memo. ERL WPL-82, 19 pp.
- Loehrer, S.M. and R. H. Johnson, 1995: Surface pressure and precipitation life cycle characteristics of PRE-STORM mesoscale convective systems. *Mon. Wea. Rev.*, **123**, 600-621.
- Miller, D. J., and R. H. Johns, 2000: A detailed look at extreme wind damage in derecho events. Preprints, 20th Conf. on Severe Local Storms, Orlando, FL, Amer. Meteor. Soc., 52-55.
- Moller, A.R., C. A. Doswell III, M. P. Foster, and G. R. Woodall, 1994: The operational recognition of supercell thunderstorm environments and storm structures. *Wea. Forecasting*, **9**, 327-347.
- Mohr, C.G., L.J. Miller, R.L. Vaughan, and H. Frank: The merging of mesoscale datasets

into a common Cartesian format for efficient and systematic analysis. *J. Atmos. Oceanic, Technol.*, **1**, 143–161.

Nolen, R. H., 1959: A radar pattern associated with tornadoes. *Bull. Amer. Meteor. Soc.*, **40**, 277–279.

Oye, D., and M. Case, 1995: REORDER: A program for gridding radar data. Research Data program, Atmospheric Technology Division, National Center for Atmospheric Research, Boulder, CO.

Oye, R., C. Mueller, and S. Smith, 1995: Software for radar translation, visualization, editing, and interpolation. Preprints, *27<sup>th</sup> Conf. On Radar Meteorology*, Vail, VO, Amer. Meteor. Soc., 359-364.

Parker, M.D., and R. H. Johnson, 2000: Organizational modes of midlatitude mesoscale convective systems. *Mon. Wea. Rev.*, **128**, 3413–3436.

Parker, M.D., 2007: Simulated Convective Lines with Parallel Stratiform Precipitation. Part I: An Archetype for Convection in Along-Line Shear. *J. Atmos. Sci.*, **64**, 267–288.

Parker, M.D., 2007: Simulated Convective Lines with Parallel Stratiform Precipitation. Part II: Governing Dynamics and Associated Sensitivities. *J. Atmos. Sci.*, **64**, 289–313.

Przyblynski, R.W. and D.M. DeClaire, 1985: Radar signatures associated with the derecho. One type of mesoscale convective system. Preprints, *14<sup>th</sup> Conf. On Severe Local Storms*, Indianapolis, IN, Amer. Meteor. Soc., 228–231

Przyblynski, R.W., 1995: The bow echo: Observations, numerical simulations, and severe weather detection methods. *Wea. Forecasting*, **10**, 203-218.

Rotunno, R., J.B. Klemp, and M.L. Weisman, 1988: A theory for strong, long-lived squall lines. *J. Atmos. Sci.*, **45**, 463-485.

Skamarock, W.C., M.L. Weisman, and J.B. Klemp, 1994: Three-dimensional evolution of simulated long-lived squall lines. *J. Atmos. Sci.*, **51**, 2563-2584.

Testud, J., P.H. Hildebrand, and W.-C. Lee, 1995: A procedure to correct airborne Doppler radar data for navigation errors using the echo returned from the earth's surface. *J. Atmos. Oceanic, Technol.*, **12**, 800-820.

Trapp, R.J., and M.L. Weisman, 2003: Low-level mesovortices within squall lines and bow echoes. Part II: Their genesis and implications. *Mon. Wea. Rev.*, **131**, 2804-2823.

Wakimoto, R.M., 2001: Convectively driven high wind events. *Severe Convective Storms, Meteor. Monogr.*, No. 50, Amer. Meteor. Soc., **75**, 189-200.

Wakimoto, R.M., H.V. Murphey, A. Nester, D.P. Jorgensen, and N.T. Atkins, 2006: High winds generated by bow echoes. Part I: Overview of the Omaha bow echo 5 July 2003 storm during BAMEX. *Mon. Wea. Rev.*, **134**, 2793-2812.

Wakimoto, R.M., H.V. Murphey, C.A. Davis, and N.T. Atkins, 2006: High winds generated by bow echoes. Part II: The relationship between the mesovortices and damaging straight-line winds. *Mon. Wea. Rev.*, **134**, 2813-2829.

Weisman, M.L., 1993: The genesis of severe, long-lived bow echoes. *J. Atmos. Sci.*, **50**, 645-670.

Weisman, M.L. Klemp, J.B., and R. Rotunno, 1988: Structure and Evolution of Numerically Simulated Squall Lines. *J. Atmos. Sci.*, **45**, 1990-2013.

Weisman, M.L., 1992: The role of convectively generated rear-inflow jets in the evolution of long-lived mesoconvective systems. *J. Atmos. Sci.*, **49**, 1826-1847.

Weisman, M.L., 1993: The genesis of severe, long-lived bow echoes. *J. Atmos. Sci.*, **50**, 645-670.

Weisman, M.L., and C.A. Davis, 1998: Mechanisms for the generation of mesoscale vortices within quasi-linear convective systems. *J. Atmos. Sci.*, **55**, 2603-2622.

Weisman, M.L., and R.J. Trapp, 2003: Low-level mesovortices within squall lines and bow echoes. Part I: Overview and sensitivity to environmental vertical wind shear. *Mon. Wea. Rev.*, **131**, 2779-2803.

Weisman, M.L. and R. Rotunno, 2005: Reply. *J. Atmos. Sci.*, **62**, 2997-3002.

Wheatley, D. M., and R. J. Trapp, 2008: The effect of mesoscale heterogeneity on the genesis and structure of mesovortices within quasi-linear convective systems. *Mon. Wea. Rev.*, **136**, 4220-4241.

Zhang, D.-L., K. Gao, D.B. Parsons, 1989: Numerical simulation of an intense squall line during the 10-11 June 1985 PRE-STORM. Part I: Model Verification. *Mon. Wea. Rev.*, **117**, 960-994.

Zhang, D.-L., 1992: The formation of a cooling-induced mesovortex in the trailing stratiform region of a midlatitude squall line. *Mon. Wea. Rev.*, **120**, 2763-2785.